CRANFIELD UNIVERSITY

Robert Oliver McCracken

The copper-bismuth-sulphur material system and thin film deposition of Cu_3BiS_3 by sputtering and evaporation for the application of photovoltaic cells

Cranfield Defence and Security
Department of Engineering and Applied Science

PhD Thesis
Academic Year: 2014-2015

Supervisor: Dr D W Lane
May 2015

Abstract

The semiconducting sulphosalt Wittichenite has been identified as a possible absorber material for thin film photovoltaic devices. It has the chemical formula Cu_3BiS_3 and its component elements are those of low toxicity and high abundance making it a very attractive prospect for photovoltaic devices.

The copper bismuth sulphur material system is not very well understood and information on it limited to a few small regions. To aid understanding of this system a pseudo-binary phase diagram along the $CuS-Bi$ join of the $Cu-Bi-S$ ternary phase diagram was constructed by making bulk samples of various compositions along the join and analysing them using X-ray diffraction and differential scanning calorimetry. This join was chosen because is crosses the point at which Cu_3BiS_3 would be expected to occur due to its stoichiometry. The $CuS-Bi$ phase diagram shows Cu_3BiS_3 forms across a wide compositional range but is mixed with either bismuth metal or copper sulphides depending on composition.

Films of Cu_3BiS_3 were made using sputtered copper and bismuth films annealed in a sulphur atmosphere and thermal co-evaporation of copper sulphide and bismuth.

Acknowledgements

I would like to thank the following for their input.

- Dr David Lane, my supervisor for his invaluable input and extreme patience
- Prof Keith Rogers for his help with XRD
- Dr John Painter for his help using the SEM and EDX
- Dr Jon Rock for his help with DSC
- Kyle Hutchings for the initial set up of sputtering equipment
- Mr Mike Sellwood and Mr Richard Hall for their technical support
- Dr Scilla Roncallo for her help during the first two years
- Deigo Colombara for at Bath University for his help with KCN etching

Funding was provided by EPSRC via the SuperGen project Photovoltaic Materials for the 21st Century grant number EP/F029624/1.

Contents

List of Figures

List of Tables

Glossary

AM1.5	Air Mass 1.5
DSC	differential scanning calorimetry
DTA	differential thermal analysis
ED-XRF	energy dispersive X-ray fluorescence spectroscopy
EDX	energy dispersive X-ray spectroscopy
ICDD	The International Centre for Diffraction Data
MTOE	million tonnes oil equivalent
RBSD	Rutherford back scattering detector
SEM	scanning electron microscopy
TCO	transparent conducting oxide
WD-XRF	wavelength dispersive X-ray fluorescence spectroscopy
XRD	X-ray diffraction
XRF	X-ray fluorescence spectroscopy

Chapter 1

Introduction

> “Modern civilization is the product of an energy binge . . . but humankind’s unappeasable appetite for energy make the solutions ephemeral and the challenge permanent”
>
> – Alfred Crosby, Children of the Sun [1]

1.1 Renewable Energy

Renewable energy can be defined as “energy flows which are replenished at the same rate as they are ‘used’ ” [2, p. 11].

At present the world meets the majority of its energy needs through the extraction and burning of fossil fuels such as coal, oil and gas. These are a non-renewable energy sources in that we use them at a rate which far exceeds the rate at which they are replenished. However, there is domestic and international pressure to increase the use of renewable energy sources. There are many reasons to do this. Some are environmental. The burning of fossil fuels and subsequent release of

CO_2 into the atmosphere is widely accepted by the science community to be the main contributor to climate change. Some are economical. When conventional fossil fuel sources start to run low the cost of that energy source will increase. The higher cost of extraction from more difficult places, for example deep sea drilling and the extraction of oil from tar sands, will also drive the price up. This provides a good economic reason to move towards renewable energy. Renewable energy sources include technologies such as hydropower, wind power, wave power, bioenergy, tidal energy, geothermal energy, and solar energy. With the exception of tidal and geothermal all the these systems are powered by the sun either directly or indirectly.

Each year 5 400 000 EJ (5.4×10^{24} J) of solar radiation is incident on the earth, about 30 % of this is reflected by the atmosphere leaving 3 800 000 EJ available to the earth [2, p. 12]. To get a better idea of the scale of this amount of energy it can be compared to the global energy consumption in 2012. According to the BP Statistical Review of World Energy 2013 [3] global energy consumption in 2012 was 12 476.6 million tonnes oil equivalent (MTOE), or 524 EJ[1] in comparable units given 1 ton oil equivalent is about 42 GJ. Therefore, in 2012 we consumed energy equal to slightly less than one seven-thousandth of that received from the sun over the same time period. From this it can be seen that renewable energy technologies tap into a very large and constant resource.

Two renewable energy technologies use energy from the sun directly, these are solar thermal energy which is used to heat water and photovoltaics which uses sunlight to drive a current and produce electricity. It is the photovoltaic technology

---

[1] or 305.68 EJ if taking MTOE as 4.4 TW h (15.84 GJ) as mentioned in review for all non-oil sources and assuming 42 GJ for oil

that this thesis will focus upon.

1.2 A Brief History of Photovoltaics

The photovoltaic effect is the conversion of light energy into electrical energy. Edmund Bequerel first reported the photovoltaic effect in 1839. He observed that light incident on a silver coated platinum electrode immersed in electrolyte produced an electric current. In 1876 Williams Adams and Richard Day found that a photocurrent could be created when selenium is contacted with two heated platinum contacts, this was the first solid state device. The first large area solar cell was prepared by Charles Fritts in 1894 and afterwards other materials were found to produce similar effects although their efficiencies were very low. It was not until the 1950s when silicon, a semiconductor, was used did these devices produce potentially useful amounts of power. Although very expensive they were used in space applications in the 1950s and 1960s because other fuel sources were comparatively heavy and therefore expensive. The 1970s energy crisis renewed interest in photovoltaics and a great deal of our current understanding of photovoltaics stem from this period. In the late 1990s production of photovoltaics expanded at a rate of 15 % to 25 % per annum which helped reduce cost through economies of scale and photovoltaics started to become competitive in applications where price was once a barrier [4, pp. 2–4]. In the last few years it rose to above 30 % and was predicted by solar market analysts NDP Solarbuzz to remain so well into 2014 [5].

1.3 Theory of Photovoltaics

1.3.1 Solar Cell Operation

Photovoltaic cells (PV cells) absorb photons of light and convert them into electricity. A semiconductor material is used since it has the property that electrons are forbidden to possess a particular range of energies. The range of forbidden energies is known as the band gap. Electrons are generally incapable of moving freely through a semiconductor because they posses energies below the band gap and reside in the full valance band. If an electron is excited to an energy above the band gap, the conduction band, it is free to move around and the semiconductor will conduct. The empty state in the valence band is then known as a hole which is also able to move about freely and act like an electron of opposite charge. In PV cells the excitation is provided when a photon of energy equal or greater than the band gap is incident on the electron. In order to produce a current when an electron-hole pair is created they must be separated before they recombine. This separation takes place due to an internal electric field set up by the presence of a p-n junction, which is an interface between p-type (positive) and n-type (negative) semiconductors, as shown in Figure 1.1.

The n-type semiconductor is doped with impurity atoms that donate electrons creating an excess of electrons in that region. The p-type semiconductor is doped with impurity atoms that accept electrons creating an excess of holes in that region. Electrons from the n-type region and holes from the p-type region diffuse across the junction and annihilate with each other, this region is called the depletion region due to the resulting lack of charge carriers present. This process establishes an electric field across the depletion region which works against further movement of

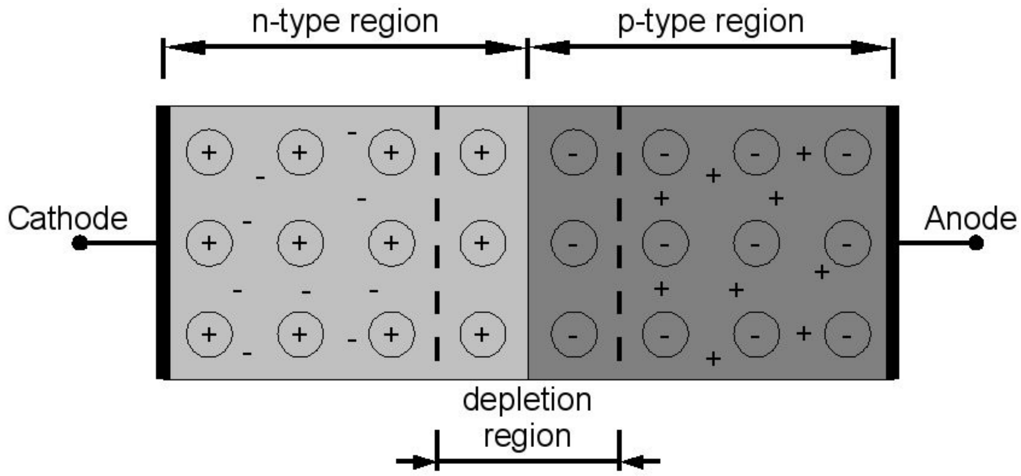

Figure 1.1: Schematic of a p-n junction

the majority carriers, i.e. the electrons in the n-type region and holes in the p-type region. However, when an electron-hole pair is created in the p-type region, as long as the electron (the minority carrier when in this region) is within a diffusion length of the depletion region it is swept into the electron rich n-type region by the electric field and does not recombine with the created hole; the same is true for holes created in the n-type region. This creates a photocurrent which is carried away via electrical contacts and may be utilised.

The electric field across the depletion region may also be explained by looking at the electronic band structure across the p-n junction. The Fermi energy level, E_F, is defined as the energy level at which the probability of an electron occupying it is 0.5 [6, p. 9]. In an undoped semiconductor the valence band is full and the conduction band is empty so the Fermi energy is theoretically placed half way between the two. This value is denoted E_i in a doped semiconductor since it is a useful reference point. In an n-type semiconductor the extra electrons from the donor atoms occupy the conduction band. Now that there are electrons occupying higher energy states the level at which the probability of occupancy is 0.5 is shifted upwards. There is a downwards shift for analogous reasons in p-type semiconductors [7, p. 40]. However, the Fermi energy must be a constant value [7, p. 91] therefore at a p-n junction the other energy bands bend to provide a constant Fermi energy level, as shown in Figure 1.2. Physically this bending is the result of the depletion region and the electric field being established by the movement of charges described above. Figure 1.2 also shows an electron-hole pair being created by the absorption of a photon of energy E_γ. The electron moves in the direction to minimise its energy (i.e. towards the n-type region) and the hole moves in the direction to maximise its energy (or more correctly, to minimise the energies of the electrons in the valence band). The resulting potential difference across the junction, the built in potential, V_{bi}, is the maximum theoretical value of the photo-voltage and is the sum of the differences of E_F and E_i in each region divided by the charge of the carrier [7, pp. 93–95]. qV_{bi}, is always less than the band gap of the material.

The band gap is a very important characteristic of a PV cell. When light enters the cell photons of energy less than the band gap are not absorbed and photons of energy greater than the band gap contribute energy equal to the band gap and the excess is wasted as heat [8, p. 320]. If the band gap is large fewer photons are absorbed lowering the resulting current and if it is small more photons are absorbed but each excited electron carries less energy lowering the resulting voltage. These places a limit on the maximum efficiency possible for a given distribution of light such as solar radiation, this limit is known as the Shockley-Queisser limit [9]. There is an optimum band gap for a given power spectrum of light and for standard

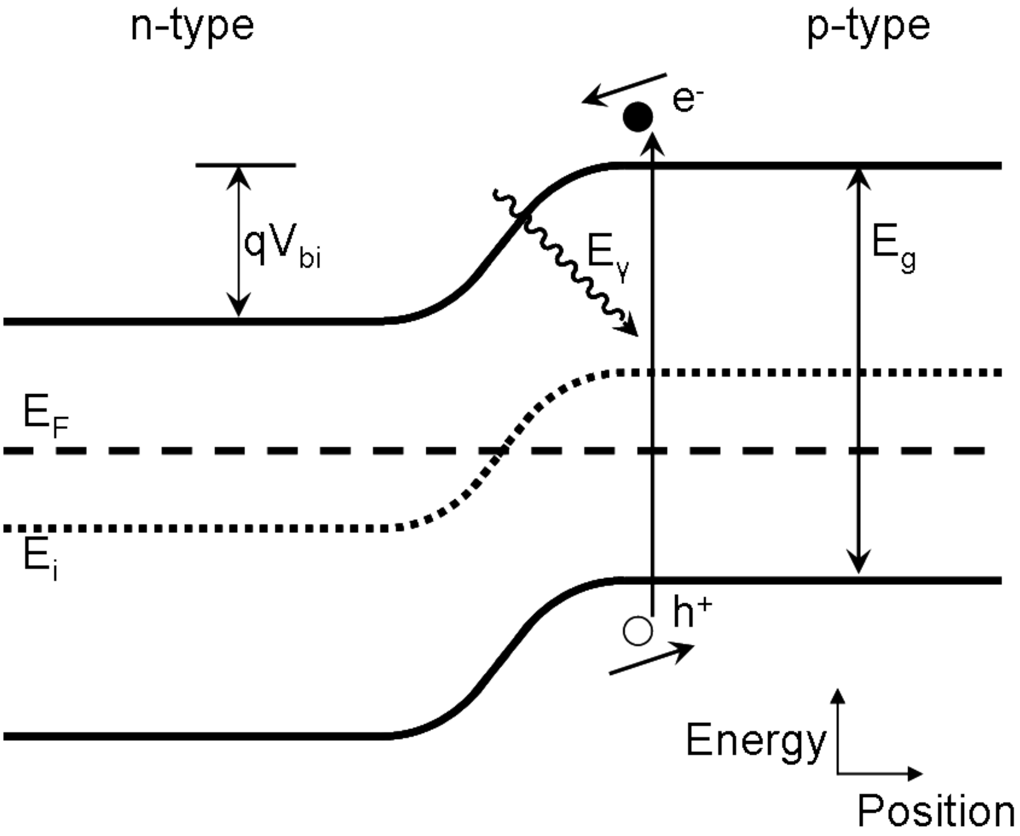

Figure 1.2: Band structure of a p-n junction, creation of an electron-hole pair illustrated and movement of resulting carriers shown

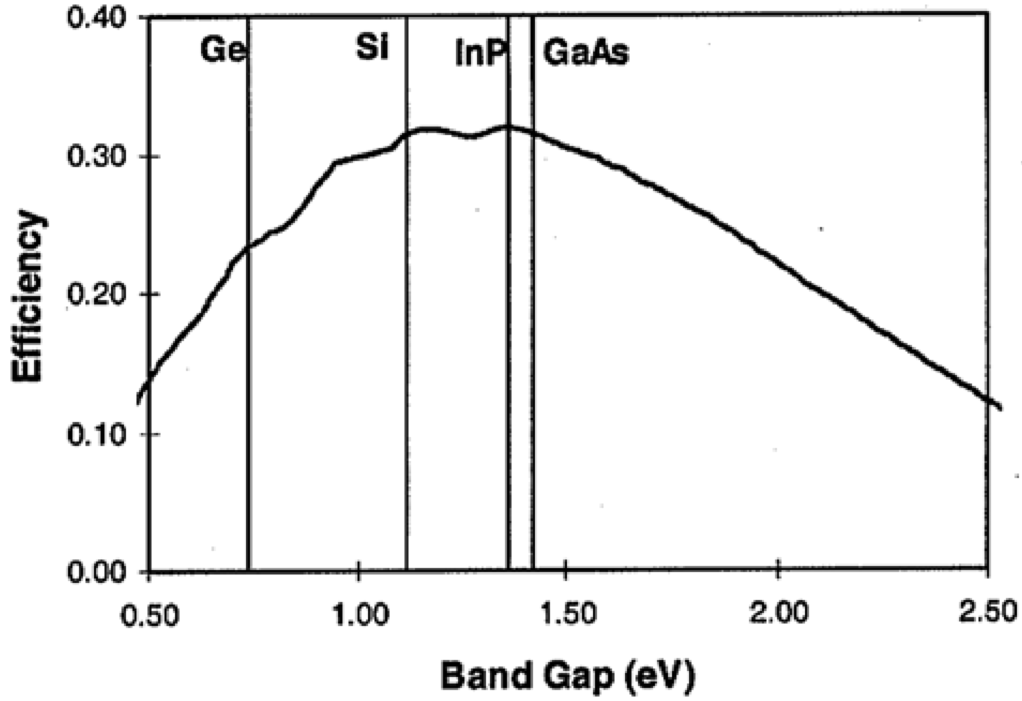

Figure 1.3: Theoretical maximum efficiency as a function of band gap for AM1.5 and the band gap of a few common photovoltaic materials [4, p. 178]

solar test conditions (see Section 1.3.2) the optimum band gap is 1 eV to 1.6 eV as shown in Figure 1.3 along with the band gap of some common photovoltaic materials.

The energy of a photon, E_γ, is directly proportional to its frequency, ν, by $E_\gamma = h\nu$ where h is the Planck constant. E_γ is therefore inversely proportional to wavelength, λ, since $\nu = c/\lambda$ for light. A convenient rule for converting photon energy in electronvolts to wavelength in nanometres is described by Equation (1.1) [4, p. 8].

$$E/\mathrm{eV} \approx 1240/(\lambda/\mathrm{nm}) \tag{1.1}$$

1.3.2 Performance and efficiency

The J–V curve

When no load, i.e. zero resistance, is applied to an illuminated PV cell the current density produced by the photocurrent is known as the short circuit current density, J_{sc}. When a load is applied a current is produced in opposition to the photocurrent reducing the net current density from its short circuit value. The opposing current is called the dark current density, J_{dark}, and can be approximated as the dark current density of an ideal diode which varies with voltage as:

$$J_{dark}(V) = J_0(e^{qV/k_BT} - 1) \tag{1.2}$$

where J_0 is a constant, k_B is the Boltzmann constant and T is temperature in kelvin. Convention has it that the photocurrent is positive, therefore the net current density, sketched in Figure 1.4 is:

$$J(V) = J_{sc} - J_{dark}(V) = J_{sc} - J_0(e^{qV/k_BT} - 1) \tag{1.3}$$

If an infinite load were to be applied to the PV cell the potential difference across it would then be the open circuit voltage, V_{oc}, at this point $J(V)$ is zero. Substituting this into Equation (1.3) gives:

$$V_{oc} = \frac{k_BT}{q}\ln(\frac{J_{sc}}{J_0} - 1) \tag{1.4}$$

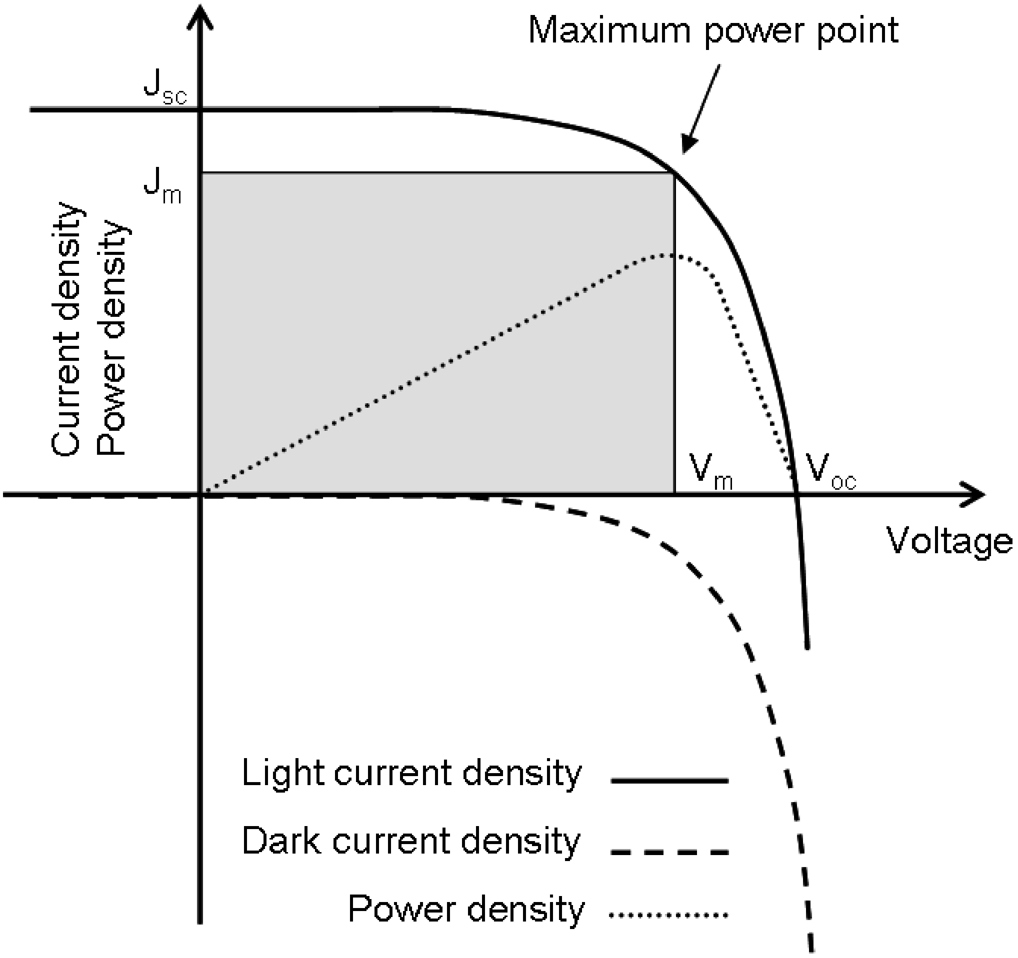

Figure 1.4: The current-voltage and power-voltage characteristics of an ideal PV cell

Efficiency

The power density is given by $P = JV$ and the maximum power point occurs at some voltage, V_m, and current density, J_m, as shown in Figure 1.4. The fill factor, FF, of a PV cell is defined as:

$$FF = \frac{J_m V_m}{J_{sc} V_{oc}} \tag{1.5}$$

The efficiency, η, of a PV cell is the ratio of maximum power density delivered and the incident light power density, P_s

$$\eta = \frac{J_m V_m}{P_s} = \frac{J_{sc} V_{oc} FF}{P_s} \tag{1.6}$$

The short circuit current density, open circuit voltage, fill factor and efficiency are the four key performance characteristics of a PV cell. [4]

Test conditions

The performance of PV cells is measured under a set of widely accepted standard conditions. The cell should be held at 25 °C and be illuminated with a light source of spectral power distribution Air Mass 1.5 (AM1.5) and total power density $1000\,\mathrm{W\,m^{-2}}$ [2, p. 70]. AM1.5 describes the spectral power distribution of solar radiation as observed from the Earth's surface at mid-latitudes and takes into account any attenuation that occurs when radiation from the sun travels through the atmosphere.

Just outside the atmosphere radiation from the sun has not travelled through the Earth's atmosphere and is close to black body radiation from a body at about

5800 K, the actual spectral power distribution is slightly different and is described as AM0 and is used for testing PV for space applications. On the surface, when the sun is at its zenith (directly overhead), the altered spectral power distribution due to absorption by gases in the atmosphere is known as AM1. When the sun is at an angle θ from the zenith the air mass number is defined as the ratio of the path length through the atmosphere at this angle and the path length through the atmosphere when the sun is at its zenith. Trigonometry therefore gives the definition of air mass as Equation (1.7). Meaning AM1.5 describes the spectral power distribution observed when the sun is $\theta = \arccos(1/1.5) \approx 48^\circ$ from the zenith or as observed at a latitude of 48° North or South at noon during the equinoxes. The spectral power distributions of blackbody radiation at a temperature of 5800 K, AM0, and AM1.5 are shown in Figure 1.5.

$$\text{Air Mass} = 1/\cos\theta \tag{1.7}$$

1.4 Evolution of Photovoltaics

There are several different ways to construct PV cells. In industry the initial technology used was crystalline wafer photovoltaics. This was followed by the addition of thin film photovoltaics which reduced the amount of semiconductor material needed. Both are currently being manufactured. There is also considerable research in other newer types of photovoltaic cells. They are not currently commercially viable but are part of the emerging technologies which include either optimising wafer or thin film technologies or developing new types of photovoltaic

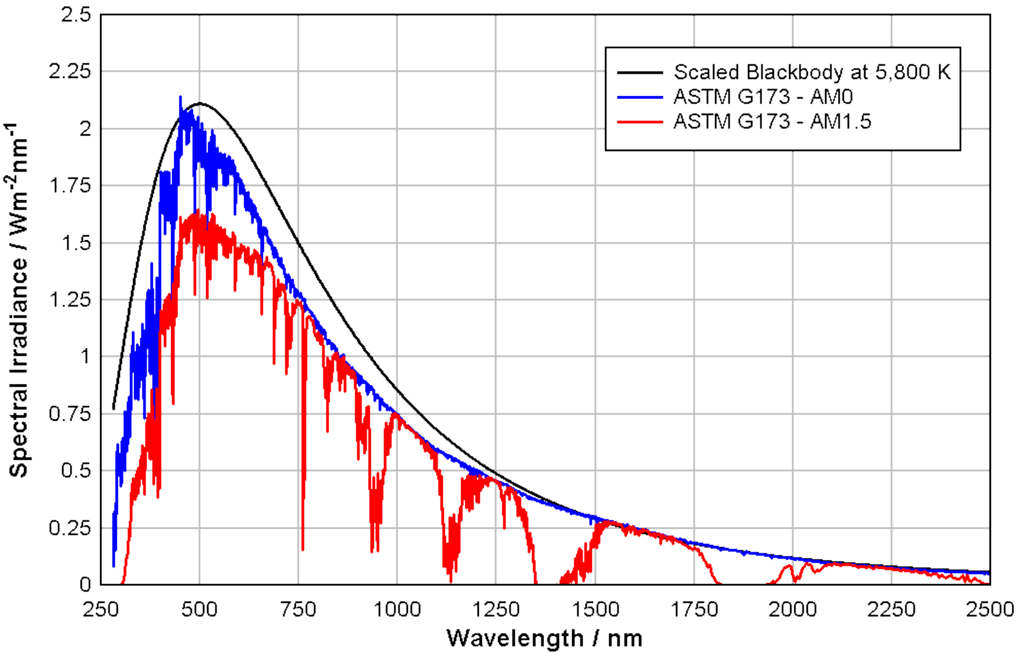

Figure 1.5: Spectral power distribution of 5800 K black body radiation, AM0, and AM1.5g. Plotted using data from the National Renewable Energy Laboratory [10]

cells altogether to further increase efficiency. The following three sections will give brief introductions to crystalline wafer, thin film, and emerging technologies.

1.4.1 Crystalline Wafer Photovoltaics

Most PV cells are made using crystalline silicon for the absorber layer [2, p. 75]. In 2014 about 92% of total PV production was silicon wafer technology [11]. Both monocrystalline and polycrystalline silicon are used. Monocrystalline cells are made from wafers cut from an extremely pure single crystal ingot of silicon. The wafers are doped to create a p-n junction, coated with an anti-reflective coating, then front contacts are deposited and the wafers are assembled together to from modules. The band gap of silicon is 1.12 eV which is within the ideal range of band gaps of 1 eV to 1.6 eV and monocrystalline silicon cells do achieve high efficiencies. However, they are also expensive to make. The manufacturing process of the silicon ingot is very energy intensive and the wafers sawn from the ingot are in the region of 100 µm to 200 µm thick. Sawing the wafer also wastes silicon as dust so the process in general is not very material efficient. Some cost savings can be made by making wafers from polycrystalline silicon. They are essentially made the same way as monocrystalline silicon cells but are cut from ingots made from polycrystalline silicon. Polycrystalline silicon is not a single crystal but is made from many small grains of monocrystalline silicon, it is cheaper to make but the PV cells have lower efficiencies due to recombination of charge carriers at grain boundaries [2, p. 77]. It is worth noting that both forms of silicon have indirect band gaps. An indirect band gap requires the absorption of momentum from the lattice of the semiconductor as well as energy from a photon to create an electron-hole pair. This extra requirement means absorption is less likely to occur as a photon travels through the silicon than if the band gap were direct. This lowers the absorption properties of silicon and is a contributing factor as to why the wafers are relatively thick and use so much material when compared to thin film photovoltaics introduced in the next next section. Despite these disadvantages silicon is the currently the most common photovoltaic material.

Other crystalline materials include gallium arsenide (GaAs) and indium phosphide (InP). Also cut from an ingot to make wafers. Unlike silicon both have a direct band gap and so absorb photons more readily. This means GaAs has a higher absorption co-efficient than silicon and is more efficient at absorbing photons as they travel though a given thickness. However, gallium and arsenic are much less abundant than silicon and therefore they are much more expensive. Indium suffers the same abundance problem also leaving InP cells very expensive.

1.4.2 Thin Film Photovoltaics

Thin Film Photovoltaics (TFPV) is a another technology which uses physical or chemical deposition to deposit very thin layers of polycrystalline or amorphous (uncrystallised) solar material unto a substrate. In 2014 about 9% of total PV production was thin film technology [11]. Evaporation, sputtering and chemical bath deposition are examples of deposition techniques employed [12, p. 65]. Materials used absorb photons readily and therefore only thin layers are required. The layers deposited are in the region of 1 µm thick vastly reducing the quantity of expensive semiconductor used. The deposition methods are relatively easy to scale to industrial size, and can deposit on cheap, large area substrates such as glass. Configurations are possible that connect the fabricated cells in series to create modules. It is for these reasons that it was thought that thin film technology had the potential to drive PV module costs to below € 1 per watt peak [13]. Amorphous PV cells are less efficient than crystalline PV cells but the reduced cost of manufacture makes them economically viable and allows them to compete with crystalline wafer photovoltaic cells. First Solar is an example of a company specialising in thin film photovoltaics using cadmium telluride [14]. Other materials used include amorphous silicon and copper indium gallium selenide. These materials are covered in greater depth in the following chapter.

1.4.3 Emerging Photovoltaics

There are also many other emerging photovoltaic technologies which have not been applied commercially or are currently at the research stage. These include dye-sensitised cells [15], perovskite cells [16], organic cells [17], and quantum dot cells. Other emerging technologies include the optimisation of wafer and thin film photovoltaics and these currently achieve the highest lab efficiencies as shown in Section 1.5. Another avenue for research is the search for other materials for thin films such as such as CZTSSe or the sulphosalts, $CuSbS_2$ and Cu_3BiS_3. These are receiving attention due to containing only abundant and non-toxic elements.

1.5 Cell efficiencies

The National Renewable Energy Laboratory [18] is the primary research institute for renewable energy in the United States of America. They publish Figure 1.6 and update it regularly to include the most current best research cell efficiencies. It should be noted these efficiencies are those reported in lab conditions and not in the field. However, it gives a good summary of the progression of photovoltaic technologies to date.

The highest efficiencies are achieved using multi-junction cells with concentrators and are as high as 44.4 % by Sharp [19] for thee-junction cells and 46 % by Fraunhofer ISE / Soitec [20] for four-junction (or more) cells. Multi-junction cells bypass the limit imposed on single junction cells by the Shockley-Queisser limit by using two or more junctions to tune into difference parts of the incident light's spectrum which would otherwise be wasted when using a single junction cell. Of the single junction cells thin film technologies have been steadily increasing since the 70s and the best lab efficiency is currently held by NREL at 23.3 % using CIGS with a concentrator. A concentrator is used to focus incident light from a large area onto a smaller area solar cell to increase its intensity.

1.6 Cu_3BiS_3 and the Copper-Bismuth-Sulphur Material System

This thesis is going to investigate Cu_3BiS_3, one of the sulphosalt materials that is a candidate absorber material in thin film photovoltaics. It also goes by the mineral name wittichenite, after the mine where it was discovered [21]. The constituent materials are all abundant and of low toxicity making it a good candidate material for future photovoltaics. Studies that have been carried out on this material suggest it has a band gap suitable for solar radiation and is a good absorber of light. Section 2.1.2 goes into these properties in more depth. Cu_3BiS_3 is a ternary phase within the Copper-Bismuth-Sulphur material system. The Copper-Bismuth-Sulphur material system and phase diagram is not very well known and further understanding of it would help with the fabrication of Cu_3BiS_3. A phase diagram shows the expected phases present for a given temperature and combination of starting materials and so can help predict how copper, bismuth and sulphur might react. This investigation will, after investigating the $Cu-Bi-S$ system as a whole, attempt to grow films of Cu_3BiS_3 using DC magnetron sputtering of metallic precursors to be heated in a sulphur atmosphere and then using direct co-evaporation of CuS and bismuth.

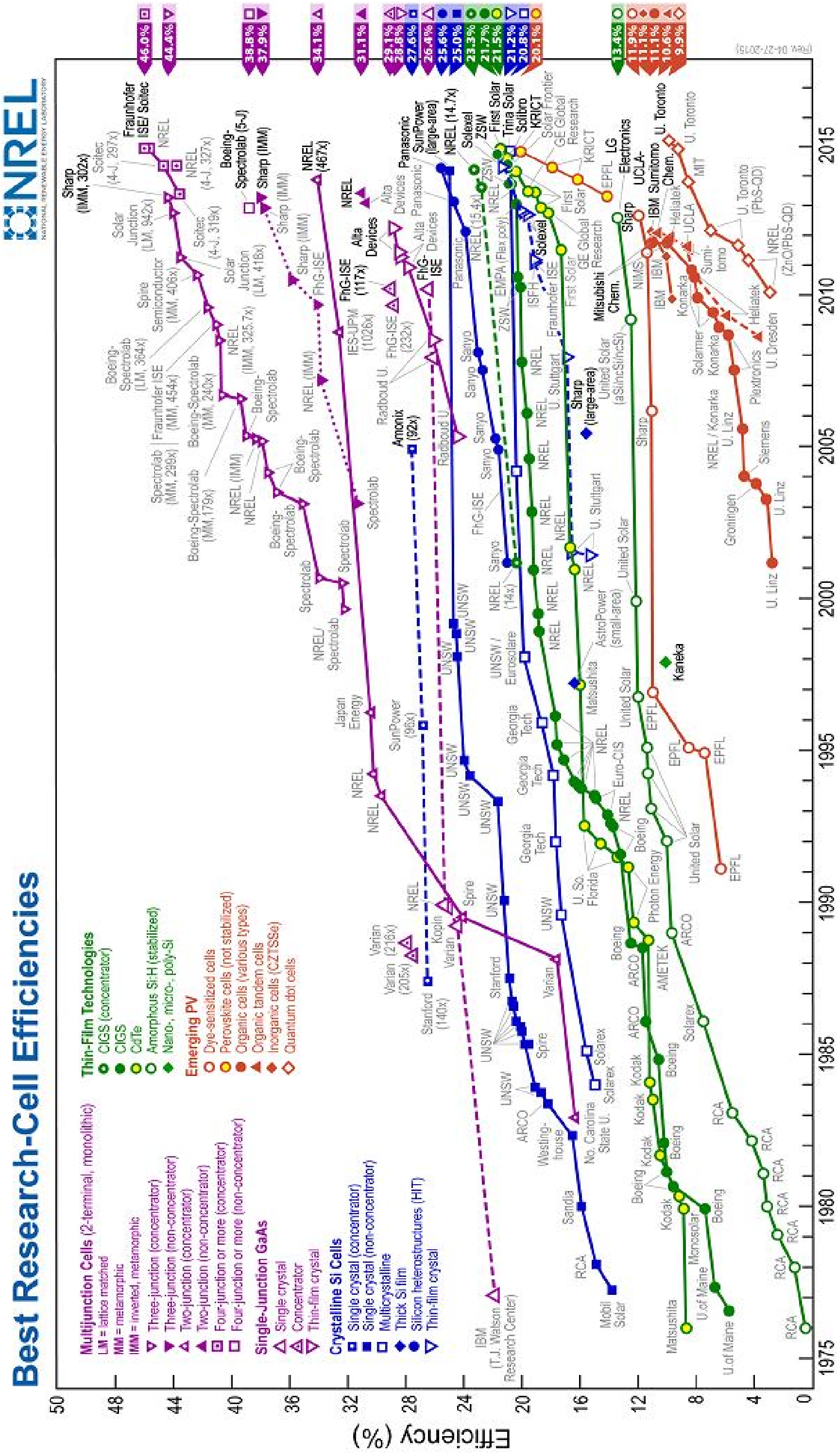

Figure 1.6: Timeline of photovolatic cell efficiencies published by NREL

1.7 Summary and Thesis Structure

In this chapter the need for alternative and renewable energy sources has been discussed. Solar energy has been identified as a very large energy source and the basics of photovoltaic theory has been explained. The evolution of photovoltaics has been discussed. Crystalline wafer, thin film and emerging photovoltaic technologies have been described and their development over the past few decades summarised. As part of the emerging photovoltaics Cu_3BiS_3 was discussed since it is believe to be a suitable candidate material.

Chapter 2 will talk about materials used to make existing and developmental solar cells in more depth. This includes a literature review and explores some of the sustainability, social and political issues connected with the use of such materials. More information on Cu_3BiS_3 as the material of primary interest of this thesis. An introduction to phase diagrams and how to construct them is also included. Having chosen the material focus of this thesis the copper bismuth sulphur material system will be explored. Currently the material system is incomplete and will be studied to gain knowledge that will help enable the production of Cu_3BiS_3. Chapter 3 will outline the techniques used to make bulk samples, deposit films, and analysis them. The $Cu-Bi-S$ material system will be studied and a partially constructed phase diagram presented. DC magnetron sputtering and thermal evaporation will be used to grow films of Cu_3BiS_3. Results are presented in Chapter 4. This will then be followed by a discussion of the results in Chapter 5 and conclusions with proposed future work in Chapter 6.

Chapter 2

Materials used in Photovoltaics

A thin film photovoltaic cell is made of several layers. There is a supportive structural layer such as glass on which the other layers of the cell are grown. Then in order from the front where light enters the cell there is a top contact layer made with a transparent conducting oxide (TCO), a window layer made with n-type semiconductor, a thicker absorber layer made with more highly absorbing p-type semiconductor, and lastly a back contact. It is the material of the absorber layer that is referred to when differentiating between different types of thin film cells. This chapter will look at the properties needed in an absorber layer material, the materials currently used as absorber materials, and some candidate materials that may make good absorber layers. The Cu$-$Bi$-$S material system will also be discussed as it includes the candidate material of interest to this study, Cu_3BiS_3.

2.1 Thin Film Absorber Materials

The absorber material in thin film photovoltaics needs to be a good absorber so that a thin film of 1 µm to 10 µm can absorb most of the light incident on it rather than allowing it to pass though. The absorption coefficient, α, is a measure of attenuation of light as it passes though a material and is described by Equation (2.1) where I_0 is the intensity of light entering the material and I is the intensity at distance x within the material. When light is attenuated by a factor of e the value of x is known as the absorption length and is given by $1/\alpha$ [4]. Two absorption lengths reduce intensity by 86.5 % and three absorption lengths reduce intensity by 95 %. For thin films an absorption length in the region of a micron is ideal and this would be achieved when absorption coefficient is 10^4 cm^{-1}.

$$I = I_0 e^{-\alpha x} \tag{2.1}$$

The absorber material should also be semiconducting and have a band gap of 1 eV to 1.6 eV which is optimal for solar radiation as shown in Figure 1.3. The diffusion length of the charge carriers should also be larger than the thickness of the film to aid their collection. Currently several materials are used. The following chapter will look at a few examples of current materials and look at some new materials identified as possibly suitable for thin film photovoltaics.

2.1.1 Current absorber materials

An example of some of the materials being used as absorber materials in photovoltaics are amorphous silicon, cadmium telluride, and copper indium gallium

Element	Production (t)	Reserves (t)	Cost ($/kg)
Cadmium	21 800	500 000	1.95
Gallium	280	NA	511.00
Germanium	155	NA	1 875.00
Indium	770	NA	580.00
Silicon	7 700 000	Almost limitless	2.65
Selenium	NA	120 000	77.18
Tellurium	NA	24 000	112.00
Bismuth	7 600	320 000	19.18
Copper	17 900 000	690 000 000	7.50
Sulphur	69 000 000	Almost limitless	0.12
Tin	230 000	4 700 000	22.93
Zinc	13 500 000	250 000 000	2.12

Table 2.1: World production, reserves, and cost of photovoltaic materials in 2013. Data taken from the US Geological Survey [23]. Values marked NA are not available.

selenide. Three other materials are briefly discussed in this section that are currently attracting research. They are copper zinc tin sulphide, copper antimony sulphide and the material this thesis will concentrate on, copper bismuth sulphide. The constituent elements of these materials are listed along with world reserves, production and cost in Table 2.1. The book 'Materials Challenges : Inorganic Photovoltaic Solar Energy' [22] covers many more materials and the following materials in greater depth.

Amorphous silicon (a-Si)

Amorphous silicon (a-Si) is deposited by plasma-enhanced chemical vapour deposition to form p-i-n homojuntions. It has a high absorption coefficient and can be cheaply produced since silicon is very abundant and cheap. Also, much less of it is used than in the more familiar crystalline silicon wafer technology. However, it has not gained a large market share due to low stable average efficiencies of about

6 % for single junction cells. The efficiency is low due to the the Staebler-Wronski effect which is the name given to the degradation caused to a-Si cell by the exposure to light [24], a significant problem to the viability of a photovoltaic device.

Cadmium telluride (CdTe)

A heterojunction of p-type cadmium telluride, CdTe, and n-type cadmium sulphide, CdS, can be deposited using a variety of deposition methods. The typical structure of a device made with CdTe is shown in Figure 2.1a. In this example light enters the cell through the glass substrate, i.e. superstrate configuration. A TCO layer is added to act as a front contact while transmitting light to the absorbing layers. CdTe has a band gap of 1.45 eV and it also has a very high absorption coefficient meaning it is suitable for solar energy conversion and a very thin layer is sufficient to absorb the light [25]. Efficiency in the lab has reached 21.5 % by First Solar and commercially range from 10 % to 11 % [13]. First Solar uses CdTe for their PV modules and as a company has a total installed capacity of 10 GW [14].

However, these materials do have problems. Cadmium is extremely toxic, therefore care has to be taken especially at the manufacturing and disposal stages of the cell's lifetime. Although believed to be safe BP Solar stopped manufacturing CdTe PV cells in 2008 citing the presence of cadmium as a problem for its customers [2, p. 79]. The other problem is the use of tellurium, it is a very rare metal and it is estimated its abundance could place an upper limit to CdTe PV cell production of 100 GW [26, p. 36].

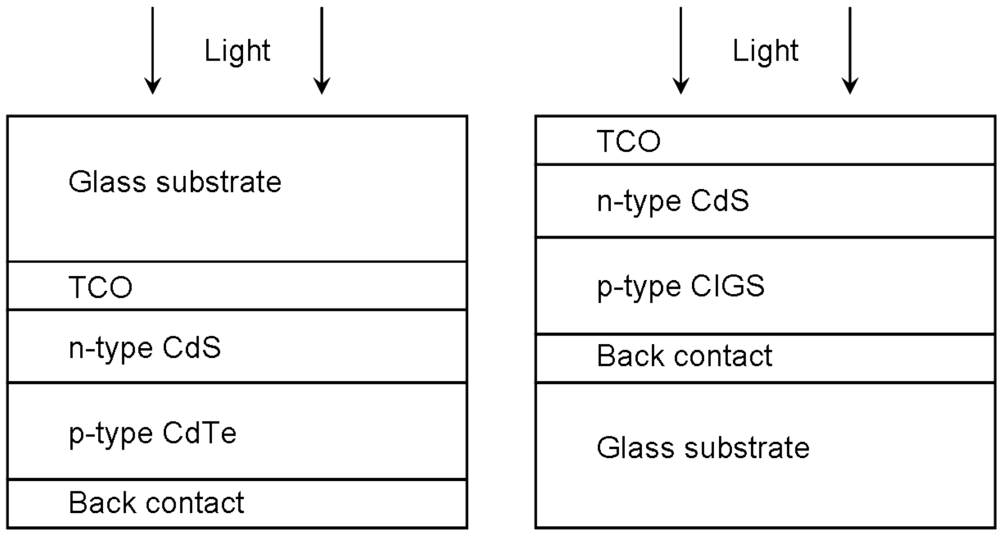

(a) CdTe cell in superstrate configuration **(b)** CIGS cell in substrate configuration

Figure 2.1: Structure of a CdTe and CIGS thin film photovoltaic cell

Copper indium gallium selenide (CIGS)

Copper indium gallium selenide, $CuIn_xGa_{(1-x)}Se_2$ or CIGS, can also be made into a heterojunction p-n junction with n-type CdS. It is deposited in the substrate configuration as shown in Figure 2.1b. Molybdenum, Mo, is deposited onto a glass substrate to make ohmic contact and act as the back contact. The CIGS film is deposited by either vapour co-deposition of all the constituent elements or the selenisation of metal precursors. Chemical bath deposition is used to add the n-type CdS layer and a transparent conducting oxide is added, front contacts are connected to this layer. [4, p. 245]

The band gap of CIGS depends on the proportion of indium to gallium and in the lab CIGS shows huge potential exhibiting efficiencies up to 21.7 % for single junction devices in the lab by ZSW [27], however due to complications the best commercial cells are only 11 % to 13 % efficient. In addition, indium is very rare limiting production of CIGS cells to only a few GW [13]. In addition, they also have the same toxicity problems as CdTe cell since they also use a CdS layer

Copper zinc tin sulphide (CZTS)

Copper zinc tin sulphide (CZTS) has a chemical formula of Cu_2ZnSnS_4 and is a material currently being investigated as a possible new material for photovoltaics. Its component materials are relatively abundant and of low toxicity. Photoelectric behaviour was first reported by Ito and Nakazawa [28] when they deposited films using atomic beam sputtering and a band gap was estimated at 1.45 eV. More recently attempts have been made to grow CZTS using sputter deposition of metallic alloy precursors which are then sulphurised in a sulphur atmosphere. One such attempt was by Hutchings [29] who used sputtering to deposit a wide composition range of alloy precursors. This study lead to the fabrication of a device which had an efficiency of 1.26 %. Within this class of material selenium can be substituted for all or part of the sulphur and more recently other groups studying this system have made made devices with efficiencies as high as 12.6 % [30]. Although, their method uses a hydrazine based solution which is highly toxic.

Copper antimony sulphide ($CuSbS_2$)

Copper antimony sulphide, $CuSbS_2$, is another material that has been identified as suitable for photovoltaics. It is from the same class of compounds as CIGS, i.e. the sulphosalts. If $x = 1$ for CIGS we are left with $CuInSe_2$. Sulphur and selenium are both chalcogens and are often substituted for each other in PV material discovery. Indium and antimony have almost equal ionic radii and the cost of antimony is lower than indium since it is much more abundant so a substitution here is desirable

[31, 32]. $CuSbS_2$ has been investigated and reported to be a p-type material with a direct band gap of 1.52 eV[33]. This falls within the ideal range of 1 eV to 1.6 eV for use with the solar spectrum. The direct optical band gap also suggests a high absorption coefficient making it suitable as an absorber material for PV cells. In studies thin films of $CuSbS_2$ have been deposited using spray pyrolysis, evaporation, and chemical bath deposition then annealing.

2.1.2 Copper Bismuth Sulphide (Cu_3BiS_3)

Copper bismuth sulphide, Cu_3BiS_3, is another material that has been identified as suitable for photovoltaic development and is the material this project will focus its attention. It is another sulphosalt and has the mineral name wittichenite, after the mine where it was discovered [21]. It has two advantages over the established CdTe and CIGS, abundance and low toxicity. Table 2.1 shows the production and reserves of constituent materials. In 2013 production of bismuth was ten times greater than that of indium and was much cheaper at $19.18/kg in contrast to $580/kg for indium. In the same year reserves for bismuth were recorded at 320 000 tonnes and tellurium was recorded as 24 000 tonnes costing $112/kg.Copper and sulphur are very abundant and cheap making Cu_3BiS_3 a very attractive material. The toxicity of the materials should also be taken into account. Although safe once made the toxicity of current constituent materials like cadmium means extra care must be taken at the fabrication and decommissioning stages of a photovoltaic's lifetime. In contrast bismuth is used as a lead replacement in solders, in ammunition and in some pharmaceuticals specifically because it has a low toxicity [23, 34].

Past studies have shown that Cu_3BiS_3 possesses a band gap within the optimal range for solar radiation and has a high optical absorption co-efficient, both critical characteristics for an absorbing material for use in solar cells. To date no photovoltaic cells have been made using this material but several groups have studied it and suggest it should be suitable.

Nair et al. annealed a multi layer of Bi_2S_3 and CuS deposited by chemical bath deposition on to glass slides in the mid 1990s to produce films of Cu_3BiS_3. The films were annealed for 1 h at 250 °C to 300 °C. These films were found to have p-type conductivity and a high optical absorbency [35]. Later the same group repeated the study using a bilayer instead of a multilayer arrangement and measured its absorption co-efficient as $4 \times 10^4\,\mathrm{cm^{-1}}$ at 500 nm and electrical conductivity as $10^2\,\Omega^{-1}\,\mathrm{cm^{-1}}$ to $10^3\,\Omega^{-1}\,\mathrm{cm^{-1}}$, the film was p-type [36].

Estrella followed on from Nair's work by exploring the following reaction pathway $3\,CuS + Bi \longrightarrow Cu_3BiS_3$. A film of CuS was chemically deposited and coated with a film of thermally evaporated bismuth then annealed at 300 °C for 1 h in a nitrogen atmosphere. The resulting films had an absorption co-efficient $>10^5\,\mathrm{cm^{-1}}$ at 650 nm, a band gap of 1.2(1) eV, and p-type [37]. This investigation will look at the same pathway but use a different deposition method and different annealing conditions.

In the mid-2000s Gerein and Haber used DC magnetron sputtering to deposit copper and bismuth onto quartz. This was annealed in an H_2S atmosphere, long times and low temperatures were required because bismuth depletion was observed at high temperatures [38]. Radio frequency magnetron sputtering of metal sulphide precursors was also attempted and the morphology of the film appeared to be highly dependent on the heating conditions and precursor morphology [39]. Later, Cu_3BiS_3 made from the reactive sputter deposition of CuS and Bi on hot substrates was reported to have a direct band gap of 1.4 eV and absorption coefficient of 10^5 cm^{-1} at 650 nm [34, 40].

Since then Mesa et al. have used reactive evaporation to make Cu_3BiS_3 films. A glass substrate was held at 300 °C, bismuth was thermally evaporated onto it followed by copper, both evaporations were carried out in a sulphur atmosphere. The resulting layer was phase pure and had a high absorption coefficient of $>10^4$ cm^{-1} and a band gap of 1.41 eV [41, 42].

The electrodeposition of copper and bismuth onto molybdenum-coated glass was attempted by researchers at Bath University. These were annealed at 450 °C to 500 °C for 30 min in sulphur vapour under flowing nitrogen gas. The subsequent films produced a photocurrent response [43]. Colombara et al. [44] undertook work into the phase evolution of Cu_3BiS_3 using this method. He concluded the reaction proceeds through the sulphides of copper and bismuth and the reaction of bismuth into Bi_2S_3 is much slower than for copper to CuS. If heated too quickly bismuth melts and compromises the morphology of the final film.

2.2 Material Phase Diagrams

To create Cu_3BiS_3 films it will be useful to understand as much of the Cu−Bi−S material system as possible. This can help predict how we can expect copper, bismuth and sulphur to combine for different combinations of the starting materials. In material science phase diagrams are used to represent the changes that a material or mix of materials goes through when heated or cooled.

For a single material a two dimensional pressure-temperature plot can show which phase a material is in at a given temperature and pressure. For example

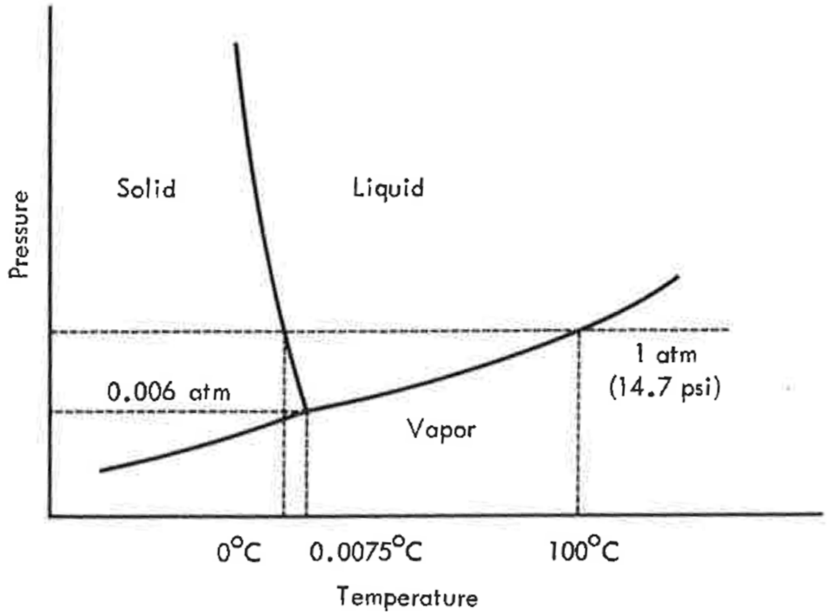

Figure 2.2: Phase diagram of water [45, p. 118]

Figure 2.2 shows the phase diagram for water. The plot shows that at atmospheric pressure water changes from a solid to a liquid at 0 °C and into a gas at 100 °C and that all three phases exist simultaneously at 0.0075 °C at 0.006 atm, the triple point of water.

When considering a mixture of two materials a third variable, composition, is introduced. To represent this on a two dimensional plot one other variable will need to be fixed. Since most material applications occur at atmospheric pressure, pressure is often fixed at 1 atmosphere. Figure 2.3 shows the binary phase diagram for mixtures of copper and bismuth at different temperatures at atmospheric pressure.

This binary phase diagram is broadly split into three regions. The lower region is a solid mixture of copper and bismuth and the top region is a liquid mixture. The middle region is a mixture of solid copper phase and liquid mixture phase and

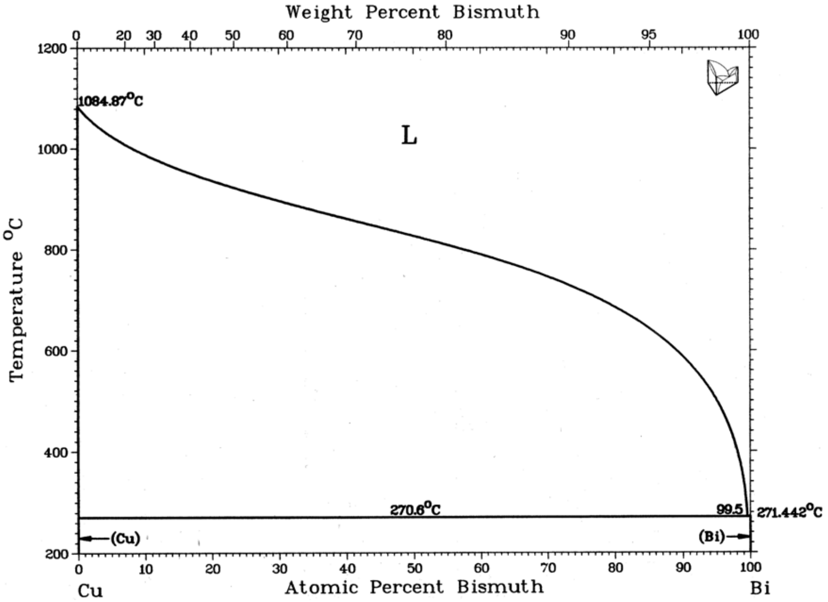

Figure 2.3: Binary phase diagram for copper and bismuth [46]

depending on the location within this region each phase has a different composition but the mixture has an overall composition as read from the horizontal axis. The exact composition of each component can be read using the lever rule. The lever rule states that within a region that is a mixture of phases the proportion of each phase is inversely proportional to the horizontal distance to either phase boundary [47, p. 5].

The sketch phase diagram in Figure 2.4 can be used to demonstrate the use of the lever rule. The overall composition at point B is x_b but this will consist of a mixture of two phases. A solid phase A with composition x_a and a liquid phase C of composition x_c. The percentage of each phase will be given using the lever rule as shown in Equation (2.2).

$$\%A = \frac{x_c - x_b}{x_c - x_a} \times 100 \quad \text{and} \quad \%C = \frac{x_b - x_a}{x_c - x_a} \times 100 \tag{2.2}$$

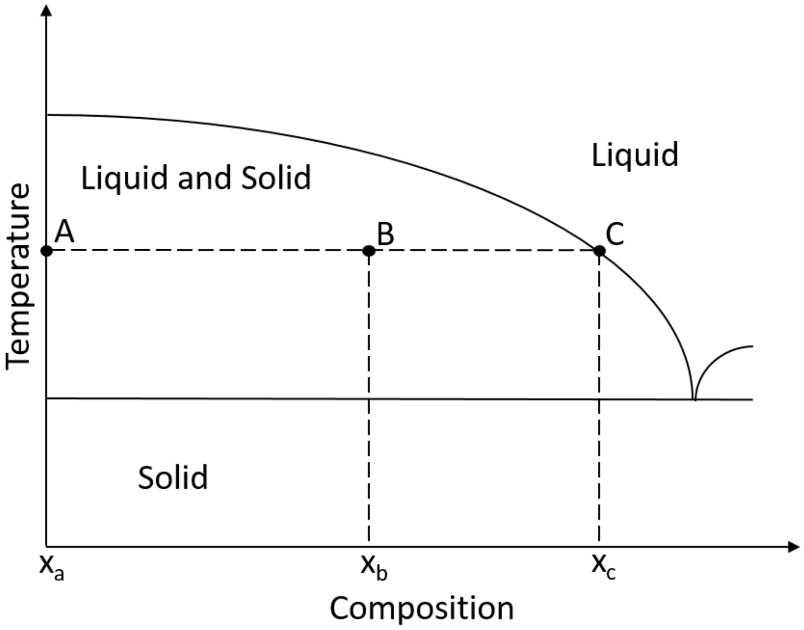

Figure 2.4: Sketch phase diagram to demonstrate the lever rule

Ternary phase diagrams are used for a mixture of three materials. All combinations of the three materials are represented by a triangular plot with an orthogonal axis for temperature, pressure is fixed as with binary phase diagrams. This gives a complicated three dimensional plot, a generic example of which can be seen in Figure 2.5. Usually a slice is taken through this three dimensional plot to show a pseudo-binary phase diagram.

2.2.1 Pseudo-Binary Phase Diagrams

A three dimensional ternary phase diagram can be difficult to build and interpret so it is common to simplify it by concentrating on a vertical slice and plot that as a two dimensional plot varying linearly in composition on the x-axis and temperature on the y-axis. Figure 2.6 shows a slice through the Cu−Bi−S material system.

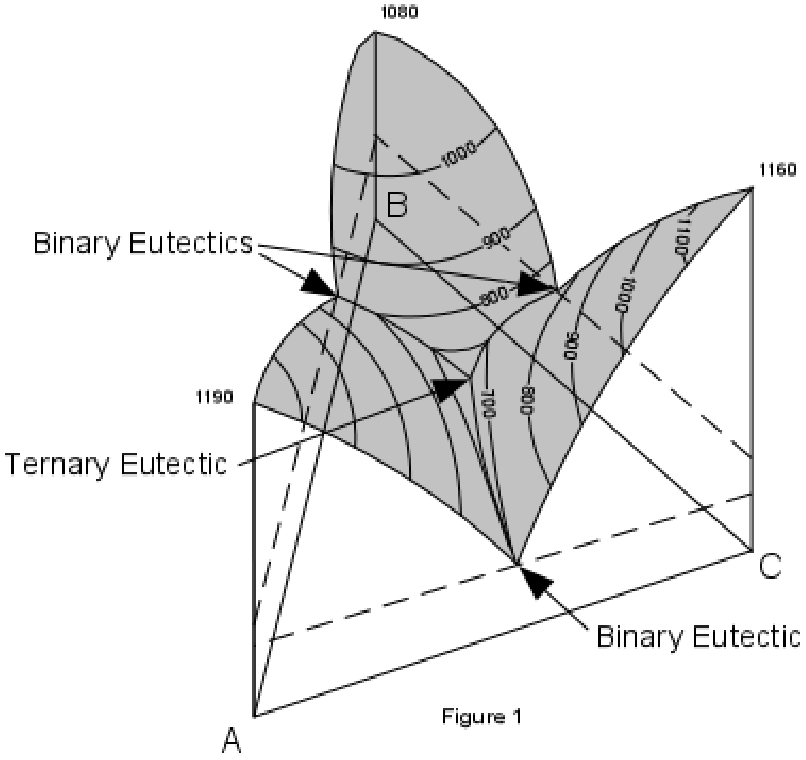

Figure 2.5: Generalised ternary phase diagram [48]

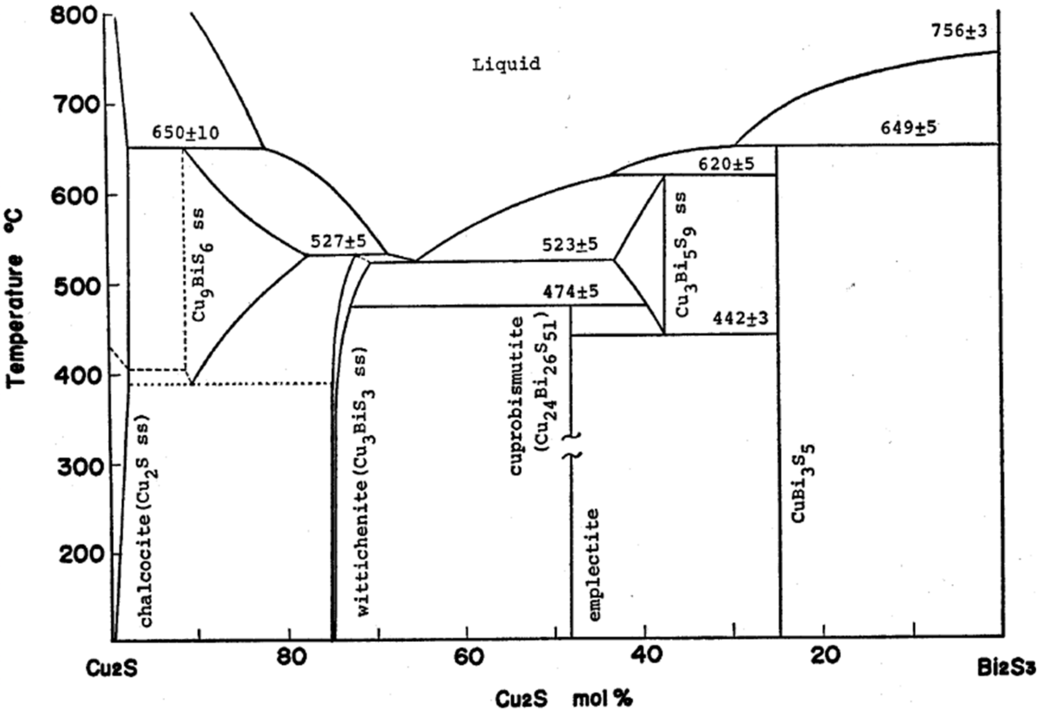

Figure 2.6: Pseudo-Binary phase diagram of the $Cu_2S-Bi_2S_3$ system [49]

This pseudo-binary phase diagram was plotted by Sugaki and Shima [49] in their investigation into the phase relations of the $Cu_2S-Bi_2S_3$ system. Several mixtures of Cu_2S and Bi_2S_3 were prepared and annealed. Then phase boundaries were determined using differential thermal analysis (DTA) and the phases present by X-ray diffraction (XRD). This appears to be an accepted way to construct a phase diagram and this investigation will use a very similar technique.

This thesis will explore a slice through the diagram from CuS to Bi. It intersects with the $Cu_2S-Bi_2S_3$ phase diagram at 75 mol % Cu_2S so it should show the same events at this composition. If all the compounds in the The International Centre for Diffraction Data (ICDD)'s database containing any mixture of copper, bismuth and sulphur are listed and sketched onto a compositional triangle plot it will look like Figure 2.7a. From this we can see there is a concentration of phases along the compositional range $Cu_2S-Bi_2S_3$ which corresponds to the pseudo-binary phase diagram in Figure 2.6. The slice this thesis is investigating passes through fewer known phases and passes through where we would expect to find Cu_3BiS_3. It would be reasonable to expect it to be less complicated. This might mean it has a wider phase pure region than the $Cu_2S-Bi_2S_3$ slice or departures from the phase pure region might be less pronounced when the CuS/Bi ratio is not exactly three. If this is the case it would simplify the fabrication of Cu_3BiS_3 films due to a greater tolerance to starting composition when using CuS and Bi as starting materials. Also, if the introduction of other phases when the CuS/Bi ratio is not exactly three is very slow there may be scope to use the starting composition as a doping method to further simplify making Cu_3BiS_3 solar devices. The final reason for choosing this slice is that CuS and Bi are readily available starting materials.

Overall there is very little information on the Cu−Bi−S material system. In addition to the $Cu_2S-Bi_2S_3$ phase diagram there are four other phase diagrams some of which cross the region of interest in this thesis. These are discussed along with the results in the discussion chapter.

2.3 Summary of Photovoltaic Materials

This chapter details the requirements of a good absorber material for use in photovoltaics. Current materials used as absorber materials were discussed alongside the cost and possible long term disadvantages of the materials used. A literature review of current research into candidate materials, CZTS, $CuSbS_2$ and Cu_3BiS_3 is presented. This thesis is going to investigate Cu_3BiS_3 and its material system by partially constructing a phase diagram then attempting to grow films of Cu_3BiS_3

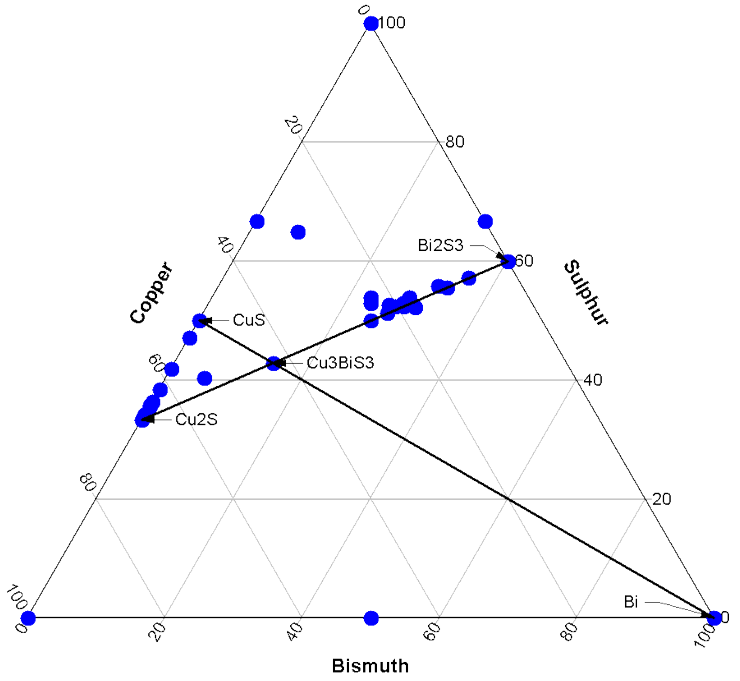

(a) All known Cu−Bi−S phases listed in the ICDD

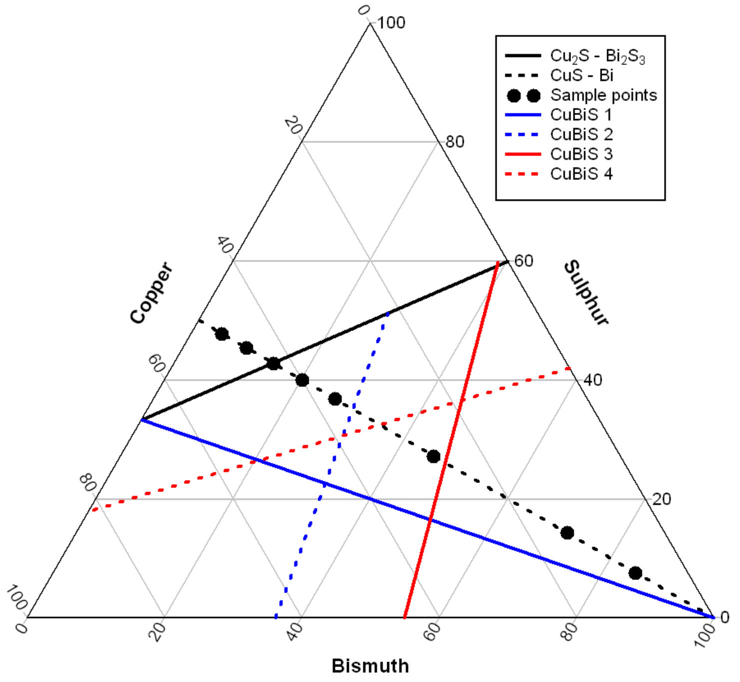

(b) Location of all known phases diagrams

Figure 2.7: Phases and Phase diagrams of the Cu−Bi−S system

using the techniques outlined in Chapter 3.

Chapter 3

Experimental Methods

This chapter outlines the methods used to prepare, analysis and interpret samples. Preparation of the bulk sample for the phase diagram work is presented first followed by the techniques used to grow thin films of Cu_3BiS_3 and analysis them.

3.1 Phase Diagram

To construct the CuS−Bi pseudo binary phase diagram several samples of varying compositions that lie along that compositional range were made and studied using a method similar to that used by Sugaki and Shima [49]. The adapted method is detailed below.

Bismuth powder, −200 mesh, 99.999 % purity from Alfa Aesar and copper sulphide powder, −100 mesh, 99.99 % purity from Testbourne Ltd where used as starting materials. Eight pellets of varying composition but restricted to $Bi_x \cdot (CuS)_{1-x}$ where x is the molar fraction of bismuth were made. The compositions chosen and the masses of starting materials required are summarised in Table 3.1.

Sample	Molar Fraction		Mass required (g)	
	Bi	CuS	Bi	CuS
1	0.083	0.917	0.330 32	1.669 68
2	0.167	0.833	0.609 37	1.390 63
3	0.250	0.750	0.842 98	1.157 02
4	0.333	0.667	1.043 62	0.956 38
5	0.417	0.583	1.219 78	0.780 22
6	0.625	0.375	1.569 23	0.430 77
7	0.833	0.167	1.831 97	0.168 03
8	0.917	0.083	1.920 47	0.079 53

Table 3.1: Masses of starting materials required for target composition of bulk sample pellets

The powders were measured and ball milled to fully mix and decrease the particle size. They were then pressed into 8 mm diameter pellets each of mass 2 g. Later two more pellets were added to fill the larger compositional gaps between samples 5, 6 and 7. They are included in the results section.

Each pellet was placed in an alumina crucible with a silica lid and placed into individual silica ampoules. They were held in place by packing the ampoule with alumina silicate ceramic wool and then evacuated and sealed. Images of the pellets can be seen in Figure 3.1. The ampoules were heated to 1000 °C in a box furnace then cooled at a rate of $20\,^{\circ}\mathrm{C\,h^{-1}}$ during working hours, the cooling profile is shown in Figure 3.2. After three days the samples had cooled to 380 °C and were held at this temperature for 2.5 months to ensure equilibrium had been reached. Using a high temperature will speed chemical reactions but a temperature too high could result in the breakdown of Cu_3BiS_3, the phase of most interested, or introduce extra phases compromising the sample. Figure 2.6 shows that Cu_9BiS_6 could form at about 400 °C so 380 °C was chosen as a suitable compromise. After

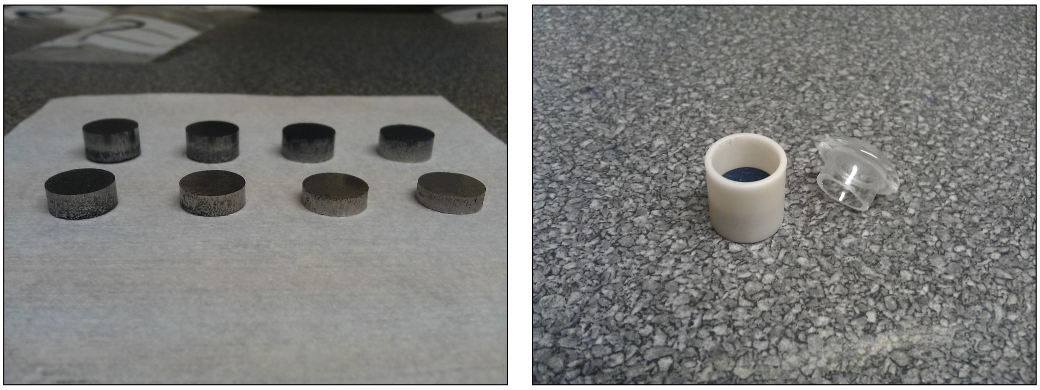

(a) Bulk sample pellets

(b) A single bulk sample pellet inside an alumna crucible with silica lid

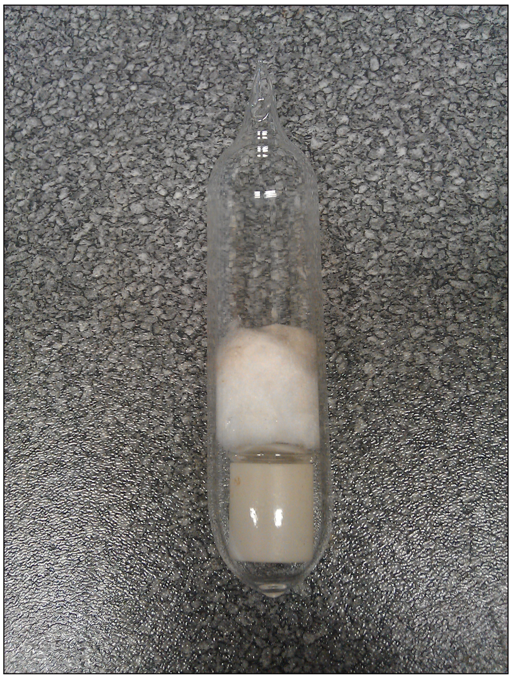

(c) Crucible held in place with ceramic wool inside a sealed evacuated ampoule ready for annealing

Figure 3.1: Images of bulk sample pellets prepared for annealing

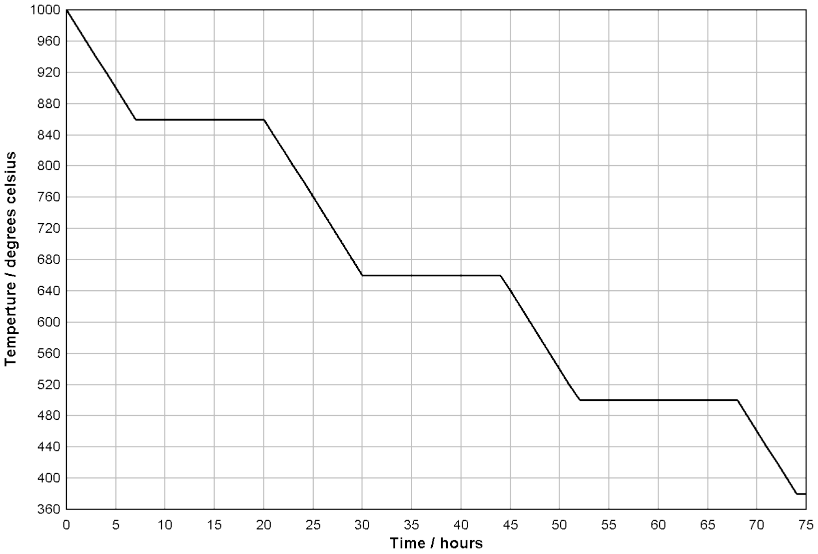

Figure 3.2: Cooling profile for samples 1 to 8 as they were cooled from 1000 °C to 380 °C

2.5 months the ampoules were quenched in liquid nitrogen to lock in the phases present at 380 °C and then opened. The pellets were removed, crushed and milled into powders and analysed using XRD and differential scanning calorimetry (DSC) detailed in Sections 3.3.1 and 3.3.2 respectively.

XRD was used to identify phases present at 380 °C and their relative quantity at each composition. This may be useful for the construction of the Bi$-$CuS phase diagram. To get data of the phase present at a higher temperature the samples were re-heated to 510 °C and analysed. They were heated to 510 °C for ten days and quenched. Parts of the samples were cold mounted in Kleer-Set polyester resin and polished to expose a surface of 2 mm to 3 mm in length. Scanning electron microscopy (SEM), light microscopy and photo conductivity tests were preformed on the samples while the rest of the samples were ground to a powder for XRD analysis.

3.2 Thin Films

3.2.1 Substrate Cleaning

Thin film deposition was carried out on 75 mm × 25 mm soda lime glass microscope slides throughout this study. The glass slides must be cleaned thoroughly before anything is deposited on them or it may compromise the film. For sputtering deposition the glass slides were gently scrubbed with a dilute decon-90 solution made up with deionised water to remove any dust and inorganic matter. They were then rinsed with deionised water and placed into a glass cradle which was put into an ultrasonic bath with acetone for 15 min to remove oils and any other organic compounds from the slides. The cradle and slides are then submerged in methanol to remove the acetone which otherwise would leave a residue. The slides were rinsed with deionised water again and dried using a compressed nitrogen jet. The slides are then stored in separate press-lock plastic bags and inside a desiccator until ready to use.Slides were prepared on the same day as deposition to reduce storage time and the possibility of them becoming contaminated. Later when the focus of the investigation turned to thermal evaporation the cleaning process was slightly altered. The slides were cleaned with decon-90 as above but after rinsing were placed into an ultrasonic bath with a 50:50 mixture of deionised water and industrial methylated spirit for 30 min. The slides were dried using a compressed nitrogen jet as before.

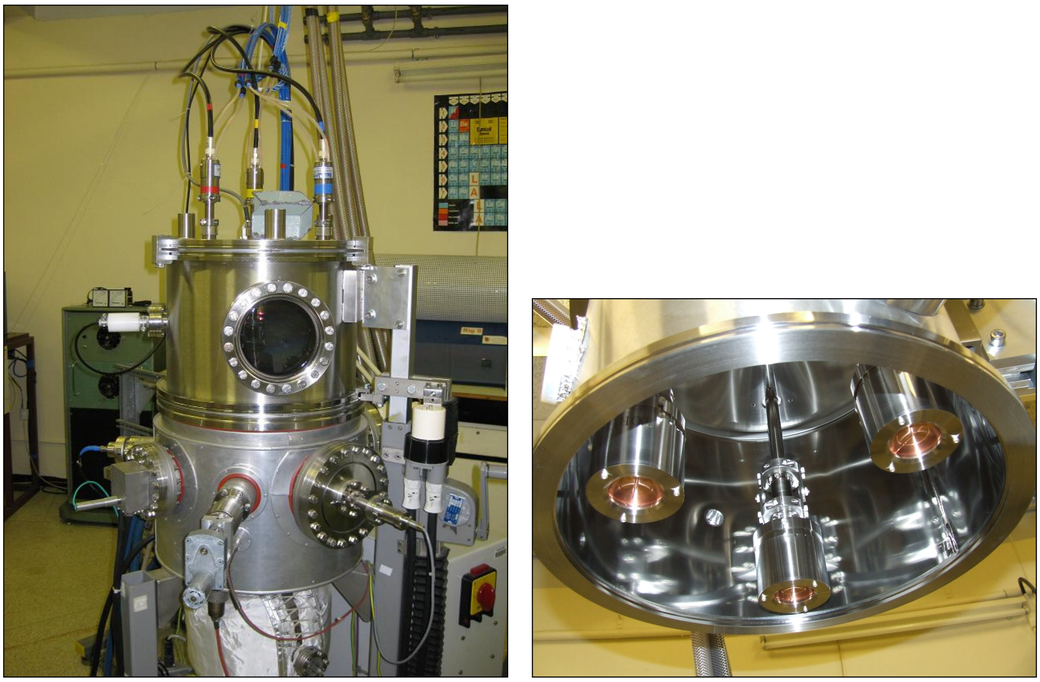

(a) The sputtering equipment used

(b) Inside the sputtering chamber showing the targets in the triangular configuration

Figure 3.3: Images of the sputtering equipment used

3.2.2 Sputter Deposition

Sputtering is a physical vapour deposition technique which can be used to grow layers of materials onto a substrate. It involves the bombardment of a target material with argon ions. This causes atoms of the target to rebound and travel in straight lines away from the target. When the atoms come into contact with a substrate they condense on it and over time a layer will build up.

The equipment available is a direct current magnetron sputtering chamber from the Kurt J. Lesker Company. This can be used to sputter materials from conducting metallic targets. A picture of the sputtering equipment and a picture of inside the chamber where the cathodes on which targets are placed is shown in Figure 3.3.

The substrate was placed in the bottom section of the sputtering chamber with the surface to be coated facing upwards. Metallic targets were attached to the suspended cathodes in the upper section of the sputtering chamber and directed towards the substrate. The chamber is then closed and pumped down to a pressure of 5×10^{-4} mbar. To remove any impurities that may have accumulated since the cleaning procedure outlined in Section 3.2.1 a glow discharge is run for 2 min. This raises the chamber pressure to 5×10^{-3} mbar and a potential difference of 3000 V (DC) is applied across the substrate platform and a secondary electrode to establish a plasma. A plasma of charged particles bombard the substrate removing impurities and preparing the surface for sputtering. Care must be taken not to damage the substrate at this point with an over exposure to the glow discharge. The chamber is once again pumped to 5×10^{-4} mbar then trickle fed argon gas until the pressure stabilises at 5×10^{-3} mbar. A large potential difference is applied between the target and substrate which ionises the argon gas and forms a plasma. Magnets confine the plasma close to the surface of the target increasing output. The heavy argon cations are accelerated by the electric field towards the target where it hits and sputters the target atoms. The target atoms are neutral and are not affected by the electric field so travel in straight lines until they condense on the substrate. Sputter deposition occurs on all of the chamber surface so it is possible to get large uniformly thick deposits. The rate of deposition can be controlled by varying the power supplied to the targets. However it is rather slow, depositing materials in the order of a few Å s^{-1}. [50]

For combinatorial work a spread of compositions across a slide is desired. These samples are referred to as libraries because they contain a spread of compositions across the slide. This was achieved by aligning the targets at an angle to the substrate rather than directly above and perpendicular. Initially the top plate

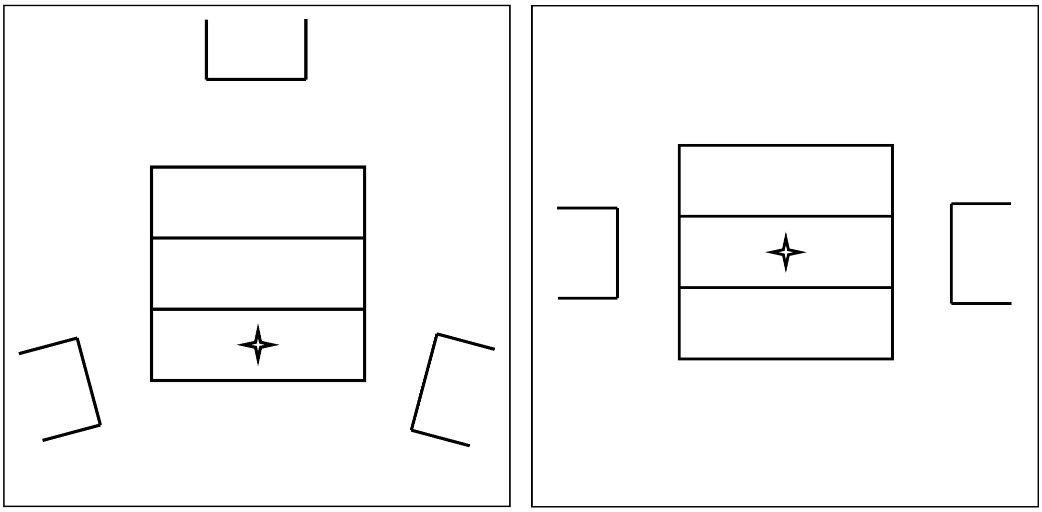

(a) Two targets of the triangular configuration top plate directed onto the centre of a one slide substrate, focus marked with a star

(b) Two targets of the linear configuration top plate directed onto the centre of a three slide substrate, focus marked with a star

Figure 3.4: Sputtering target configurations used with either top plate

in Figure 3.3b was used which had three targets in a triangular arrangement. Figure 3.4a shows a sketch of the sputtering set up used to sputter bismuth and copper initially. By using two targets and directing them to the centre of the closest slide a single slide library which varies in one direction can be made. After the library work the top plate was replaced with a top plate with three targets in a row which allowed for uniform sputtering from directly above and sputtering at an angle from either side while keeping the substrate in a central location, shown in Figure 3.4b.

Sputter Target Power

The rate of deposition is dependent on the power applied to the target and the target material, each material also has a maximum power above which it may melt and damage the target or equipment. The relationship between power and deposition rate was previously investigated by Kyle Hutchings [29] and is documented in the lab manual along with maximum power for each material. The following equations from the lab manual can be used to estimate the power required for a desired deposition rate. R_i is the rate in Å s^{-1} and P_i is power in watts.

$$R_{copper} = 0.0572 P_{copper} + 0.2267 \tag{3.1}$$

$$R_{bismuth} = 0.3327 P_{bismuth} + 0.725 \tag{3.2}$$

For a given area the thickness of a film is directly proportional to the volume and so the molar volume can be used as a conversion factor between atomic number and thickness. The molar volume, V_m, is molar mass divided by mass density. The molar volume of bismuth was found to be 21.31 cm^3 mol^{-1} [51] and the molar volume of copper was calculated to be 7.09 cm^3 mol^{-1}.

If aiming for a central atomic ratio of copper and bismuth of 3:1 multiply each by the molar volume to get a desired ratio of volumes. This is directly proportional to the thickness of each material and if the materials are deposited for the same length of time it is also proportional to the rate of deposition. In this case the rate of deposition will be in a ratio of $3 \times 7.09 : 1 \times 21.31$ which is very close to 1:1. If a power of 30 W is chosen for the bismuth target Equation (3.2) can be used to see this will give a deposition rate of 10.7 Å s^{-1}. To get the same deposition rate for copper Equation (3.1) can be used to show 183 W will be required. It should be stressed these are starting points, the material flux from each target may interact with the other during co-depositions and therefore adjustments may need to be made.

Figure 3.5: Image of the thermal evaporation equipment used to sulphurise metallic precursors

3.2.3 Thermal Evaporation

Thermal evaporation was used to deposit a film of sulphur on to metallic precursors grown in the previous section and it was also used to deposit films directly. Each instance will be explained more fully after a general introduction to thermal evaporation.

Thermal evaporation involves heating a source material in a vacuum so that it boils or sublimes a vapour. When the vapour escapes from the surface of the source material it travels in straight lines until it condenses on a surface. This is because at low pressure there are few atoms to collide with and alter the travelling atoms' path.

An image of the equipment available can be seen in Figure 3.5. The equipment is covered by a bell jar so that it may be pumped down to a pressure in the order of 10^{-5} mbar. There is an upper platform with a window on which the sample to be coated sits face down. Below the platform is one or more evaporation source. In the image it has one source of sulphur. The source material is held in either an alumina crucible or a tungsten boat. It is heated by driving an electrical current through a coil around the crucible or through the tungsten boat. An in-situ quartz crystal thickness monitor is placed next to the precursor to record an approximate thickness of the layer deposited in Å. This method can be used to maintain high levels of purity but is difficult to run for long periods of time for large quantities of evaporate [50].

Deposition of Sulphur

In the Section 3.2.2 sputter deposition was used to create metallic precursors of copper and bismuth. Next thermal evaporation was used to add sulphur to the film. An alumina crucible was half filled with sulphur powder and heated by passing an electric current though a coil basket holding the crucible. The current was raised slowly until the quartz crystal monitor recorded a deposition rate of approximately $10\,\text{Å}\,\text{s}^{-1}$ and turned off once $10\,\text{kÅ}$ ($1\,\mu\text{m}$) was deposited. This resulted in a metallic film with a sulphur film on top. To encourage a reaction these samples were annealed as detailed in Section 3.2.4.

Deposition of Copper, Bismuth and Sulphur

Later in the investigation films were grown directly using thermal evaporation. This required a few alterations to the equipment. The crucible containing sulphur was swapped for a crucible containing bismuth and a tungsten boat was added for the evaporation of copper sulphide to take place from. The current to each source was independent of each other which meant each source could be heated separately. At some point a baffle was used to partially shadow the sources to create a composition gradient across the sample. This was achieved by placing a sheet of metal very much like the shutter but smaller between the sources and the substrate.

3.2.4 Annealing

The sulphurised samples from Section 3.2.3 were sealed in evacuated Pyrex ampoules and heated in a tube furnace to encourage a reaction between the sulphur layer and previously deposited metallic layer. The ampoule was heated from room temperature to the desired temperature then held at that temperature for a recorded length of time. Afterwards the ampoule is removed and left to cool naturally. The furnaces available are a Carbolite tube furnace and a Lenton tube furnace by Thermal Engineering Services.

Figure 3.6 shows the temperature profile of the furnace used to anneal the thin film samples from the centre of the furnace where the samples are placed to the edge as measured using a type K thermocouple. At the centre the temperature is in the order of 5 % lower than the set temperature of the furnace and the temperature drops with distance from the centre. The central region appears to be large enough to accommodate the samples without too much variation in temperature across the sample.

3.3 Analysis Techniques

The following analysis techniques were used in this study.

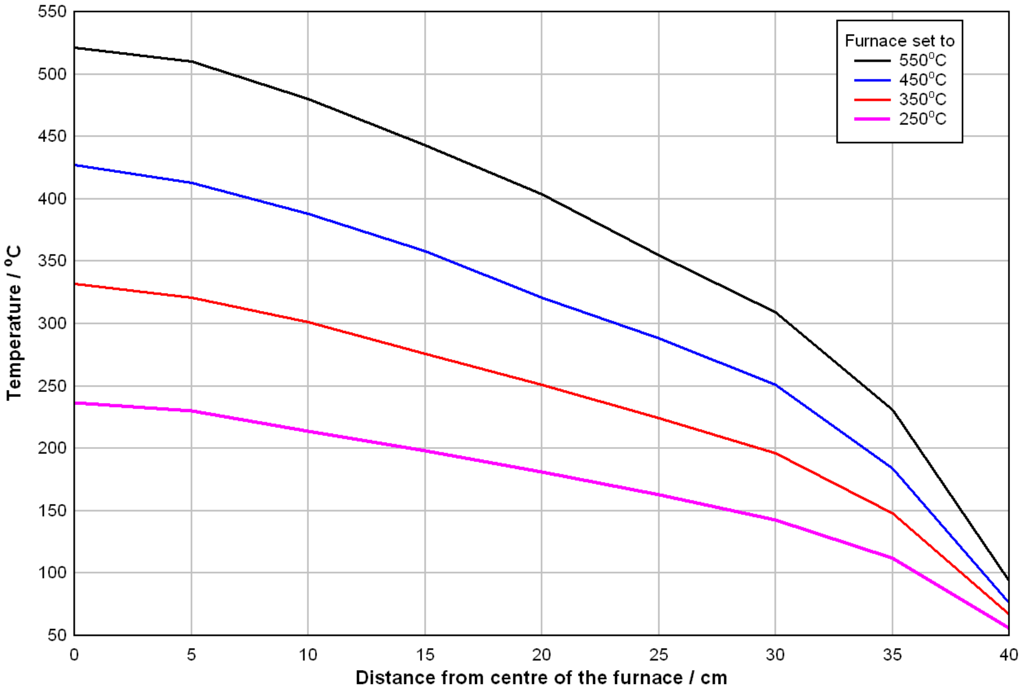

Figure 3.6: Tube furnace temperature profile from the centre to one end of the tube

3.3.1 Differential Scanning Calorimetry

DSC was used to find the temperatures at which phase transitions happen in the bulk samples for the phase diagram work. Aliquots of the powdered samples were taken and placed in alumina crucibles. The aliquots were heated at a user defined rate in °C min^{-1}. To maintain a constant rate of temperature change the heat flow is carefully controlled by the instrument and compared to the heat supplied to an empty reference crucible. The DSC plots a graph of heat flow versus time (or temperature since they are deliberately directly related) These graphs are usually mostly horizontal lines or curves with steps and/or peaks present. Interpretation of the shape and peaks of these curves can give information about the temperatures at which phase changes occur for each sample. For example a downward peak would

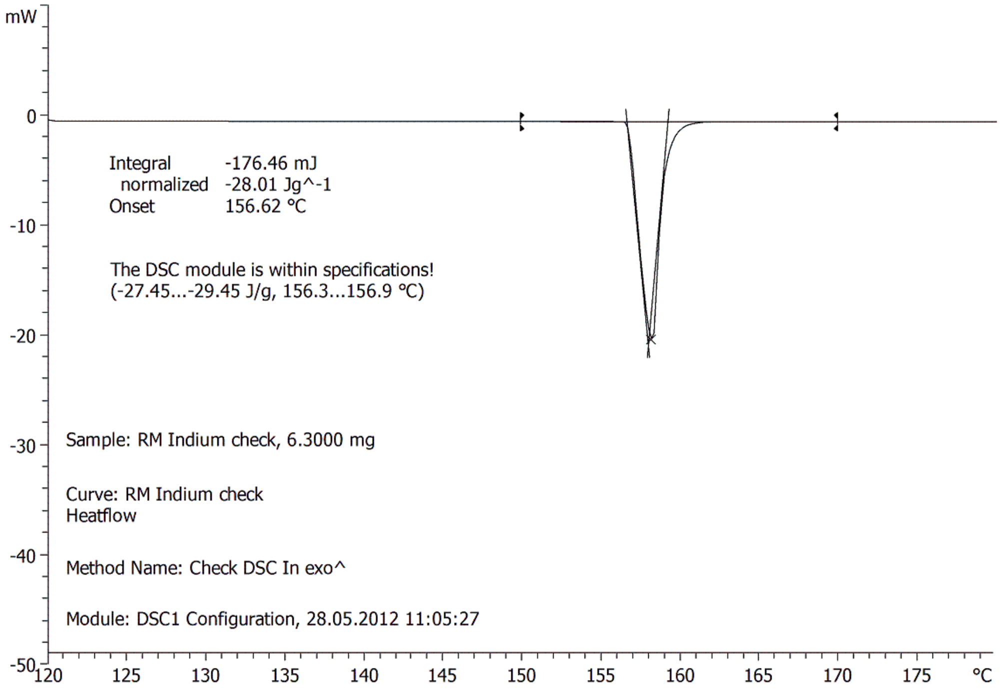

Figure 3.7: An example DSC heating curve showing the melting point of indium at 156.62 °C

represent an endothermic reaction or phase transition. There does not seem to be a convention for which part of the peak to read the temperature from. To be as consistent as possible sharp peaks with a well defined onset temperature are read as occurring at that onset temperature. The onset temperature of a broad peak is much harder to define so their characteristic temperature was taken to be at their maxima. DSC also gives a precise value of enthalpy for a thermal effect [52]. The enthalpy is measured by integrating the curve over the peak, the area is the enthalpy of the thermal event.

The equipment used in the investigation was a Mettler Toledo Differential Scanning Calorimeter, DSC 1. Before using the equipment a calibration routine should be carried out using a sample of indium. The calibration routine produces a heating curve clearly shows the melting point of indium as an endothermic downward peak. This is shown in Figure 3.7 as an example of an output from DSC analysis. In this case the software automatically determines the onset temperature and normalised integral which is the enthalpy in units of J g^{-1} and compares them to expected values.

3.3.2 X-ray Diffraction

XRD is a non destructive method that records and analyses X-rays scattered from the planes of a crystal lattice. From this information it is possible to determine crystallographic properties and chemical composition of the sample. In this investigation it will be used to identify phases present.

The atoms in a crystalline material are arranged in a regular three-dimensional structure called a crystal lattice. The regular arrangement may be long range as it would be for a single crystal or short range as it would be for a polycrystalline substance. If there is no regular arrangement at all the material is not crystalline and is amorphous. The atoms in a crystal lattice can be viewed as many planes parallel to each other and separated by a distance, d. This distance depends on the material, lattice structure and the ionic radii of the atoms present. For any lattice there are planes in many orientations, each with a specific d value. An example of three planes present in a crystal lattice and their d-spacings is shown in Figure 3.8.

If parallel monochromatic X-rays are incident on the planes some of them are reflected and some will penetrate deeper into the lattice to another parallel plane and be reflected from it. Depending on the angle of incidence the extra distance travelled by the penetrating X-rays will be more than those reflected

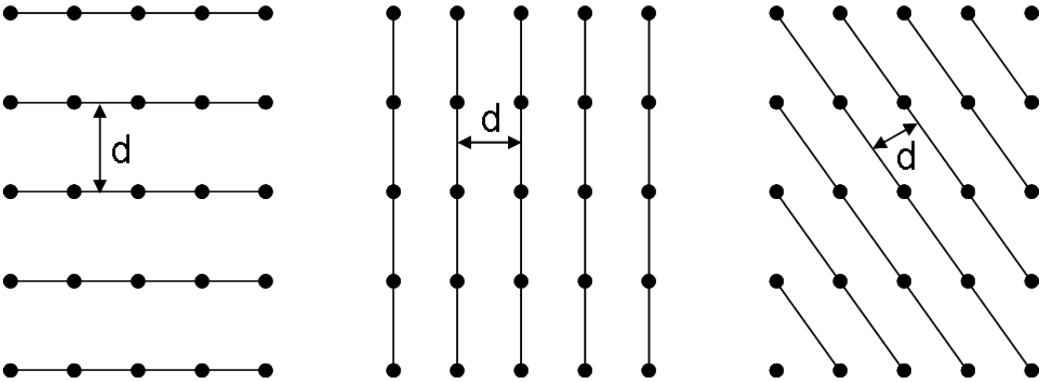

Figure 3.8: Three example planes within a crystal lattice with their d-spacing marked

from the plane or planes above. See Figure 3.9. If the path difference equals a whole number number of wavelengths constructive interference occurs. The wavelength of the incident X-rays is known and by studying the angle at which constructive interference is observed Bragg's law may be used to determine the distance between the planes by Equation (3.3).

$$\lambda = 2d \sin \theta \tag{3.3}$$

For this project the d-spacing need not be calculated. Instead, a diffractogram is produced which shows intensity of reflected X-rays as a function of 2θ, the incident and scattering angle, both θ added together. This shows peaks at values of 2θ which correspond to constructive interference from a particular set of planes from a particular material. By studying the position of the peaks the material or phase of material may be identified by comparing them to those held in the ICDD database of known materials. Peak heights can give information on the relative concentration of phases present. Peak widths can give information on grain size, large grains give sharp peaks and peak width increases as gain size decreases. The presence of a background hump shows amorphous content.

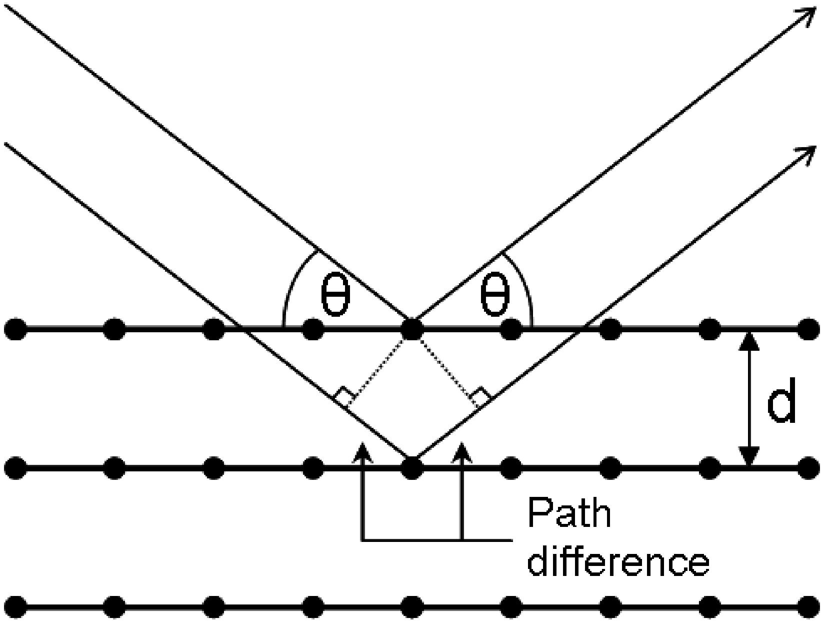

Figure 3.9: Schematic diagram showing parallel incident X-rays reflected from planes of a crystal lattice. When the total path difference equals a whole number of wavelengths constructive interference occurs

The glass substrate used for these thin films is amorphous so to limit the X-rays from penetrating too deep into the substrate and producing a large background hump incident angles are generally kept low at between 10° and 30°

The equipment available is a Bruker D8, Cu K-alpha X-ray source and a GADDS area detector. Probing spot size is approximately 500 µm. The probe is scanned across the library collecting data from each point, the diffractogram of each point is then studied using Crystallographica Search-Match software to determine phases present.

3.3.3 Scanning Electron Microscopy

A beam of thermionically emitted electrons is focused onto the sample to be investigated. Only a small portion of the sample point is probed at any one time so the beam is scanned across the point of interest to build up a more complete picture. When the incident electrons arrive at the sample they decelerate transferring energy inelastically to atomic electrons present in the sample. Through many random scattering events the beam fills a tear-drop shaped volume extending into the sample. From this volume secondary electrons, back scattered electrons and X-rays are emitted. [53]

Secondary Electrons

Images of the surface may be produced by the detection of secondary elections. These low energy electrons are emitted from the surface of the sample no deeper than several angstroms. A scintillator and photomultiplier combination is used to detect the relative number of secondary electrons from any one point and an image is built up as the scanning beam scans across the sample point. Images of high magnification, resolution and depth of field can be obtained using this technique and are useful for studying the morphology of thin films.

Back Scattered Electrons

Higher energy electrons can be elastically back scattered from the atoms within the sample. The probability of back scattering occurring is proportional to the atomic number of the atoms in the sample but the relationship is weak and cannot be used to identify the atoms present. If there are large changes in atomic number they can be used to image phase contrast. Typically the higher energy electrons in the electron beam and penetrate deeper into the sample and so cannot be used to image topology but this can compensated for by using a glancing angle and in this instance an image of the surface can be obtained and can be useful when imaging with secondary elections is difficult.

X-Rays

X-rays are emitted from yet deeper into the tear-drop volume and are characteristic of the atoms in the sample. The energy from the incident electrons excite atomic electrons and when the atomic electrons relax back into their ground state they emit radiation in the X-ray range. By analysing the energies of the emitted X-rays the atoms can be identified and by analysing the relative numbers of X-rays the composition of the tear-drop volume can be determined.

Summary

The technique using secondary electrons to image surfaces will be referred to as SEM and the technique using X-rays to determine composition will be referred to as energy dispersive X-ray spectroscopy (EDX). Given the numerical output of EDX it will contain some measurement error. The proportion of each material identified is described in terms of a percent. If an error can be attributed to each percent value it is a simple case of adding relative errors to get the error of the ratio of two materials. However, the modelling software accompanying the equipment does not provide an error value. Values for composition be quoted without errors but it might be worth considering later.

The equipment used was a LEO 435VP scanning electron microscope with an EDAX energy-dispersive X-ray spectroscopy detector. EDX analysis will be carried out using EDAX Genesis software.

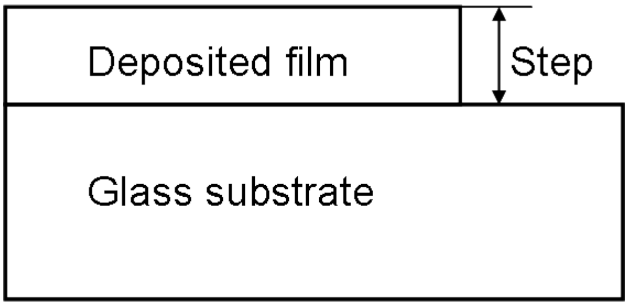

Figure 3.10: Step in deposited film to enable alpha step to measure film thickness

3.3.4 Alpha Step

A mechanical stylus is moved over the surface of the film and vertical displacement is measured as it traces the surface. In order to determine the thickness of the film a step is introduced. This was done by applying tape to part of the substrate during deposition and then removing it afterwards. The taped part of the substrate had no film deposited on it and can be used as a zero reference when measuring the height, or thickness, of the film. As the stylus moves over the step it measures the height difference between the top of the film and the top of the substrate below it, see Figure 3.10. Vertical resolution can get up to about 1 Å. This technique has limitations, such as the creation of the step. It either has to be done in advance or by etching by mechanical or chemical means which is difficult without affecting the rest of the film. The mechanical stylus has the potential to damage the film if it is either very soft or has not adhered well to the substrate and background vibration and substrate roughness can introduce unwanted noise. [53, pp. 576–578] The equipment used was an Alpha-step 100 by Tencor Instruments.

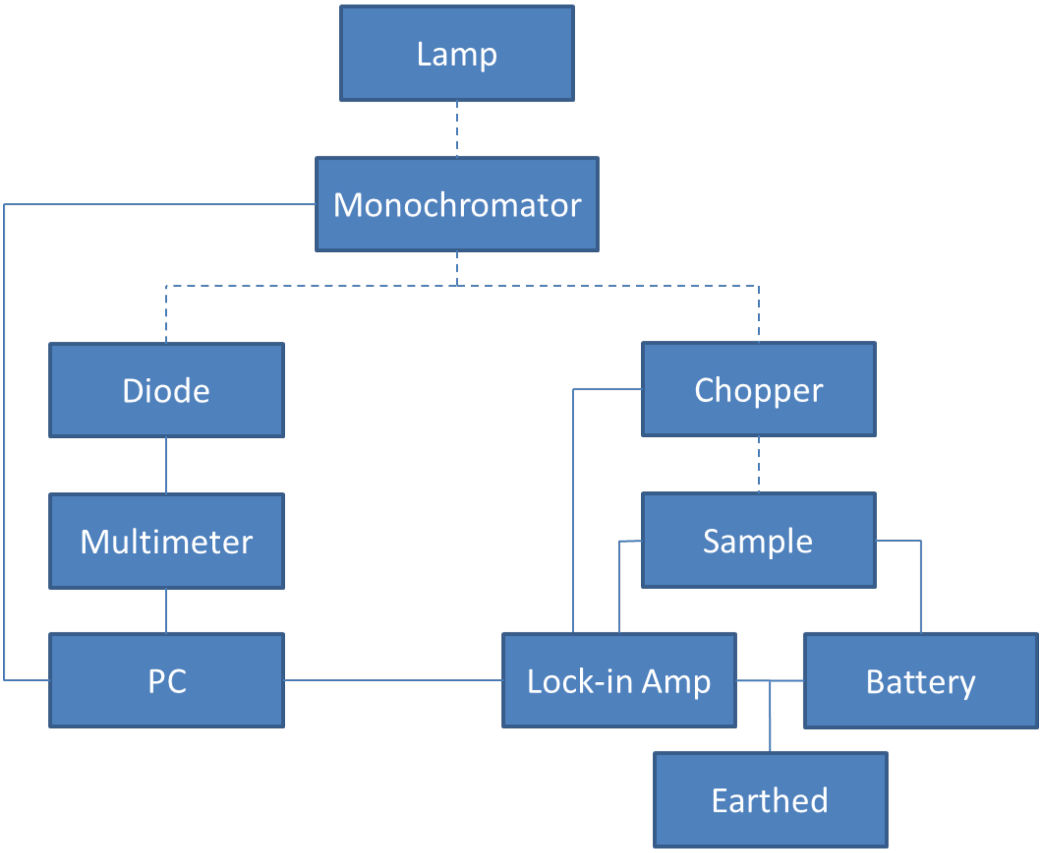

Figure 3.11: A schematic block diagram of the arrangement of the equipment used in photoconductivity testing

3.3.5 Photoconductivity

Photoconductivity is the phenomenon in which a semiconductor's conductance changes with the absorption of light. When photons of light possess more energy than the band gap of the material they are incident upon they excite electrons into the conduction band which increases the conductance of the semiconductor. This variation of conductance with photon energy can be used to determine the band gap energy from the point at which conduction commences.

A schematic block diagram of the arrangement of the equipment used to measure photoconductivity can be seen in Figure 3.11. Light is provided by a

100 W halogen lamp and is passed through a monochromator controlled by a computer. The monochromatic light is then passed through a bifurcated high grade optical bundle and split in two equally. One half of the optic bundle is directed onto a reference photo-diode to measure incident power and the other half is passed through a chopper set at a frequency of 27 Hz and is then focused using quartz optics onto the sample. A PP3 battery provides a low noise 9 V bias across the sample and the current is recorded using a lock-in amplifier set to the frequency of the chopper as that it picks up any variation due to the chopped light focused on the sample. Interrupting the light source and looking for a signal of the same period means a much smaller signal can be detected before being lost in the background noise. A computer records the periodic current from the sample and from the reference diode, calculates the photoconductivity at that wavelengh then moves the monochromator to the next wavelength to be tested. Data collection was controlled by a National Instruments LabVIEW interface (see Appendix A).

Using Ohm's law the resistance of a sample is $R = V/I$ where V is the voltage across the sample supplied by the battery and I is the current flowing through it. The current has two components, I_0 and I_{ph}. I_0 is due to the intrinsic conductance of the sample and I_{ph} is the result of any increase to the conductance due to the chopped illumination. Only I_{ph} is recorded by the lock-in amplifier. The overall conductance of the sample is:

$$G = \frac{I}{V} = \frac{I_0 + I_{ph}}{V} = \frac{I_0}{V} + \frac{I_{ph}}{V} = G_0 + G_{ph} \tag{3.4}$$

The photoconductance is of interest to us therefore the following was used to calculate it at each wavelength step:

$$G_{ph} = \frac{I_{ph}}{V} \tag{3.5}$$

The photoconductance of the sample was measured over a range of wavelengths however as different wavelengths were selected the power of the light incident on the sample changes because of the spectral distribution of the lamp and the transmittance properties of the optics. An example of the variation of incident power between 200 nm and 1100 nm in 5 nm steps is shown in Figure 3.12. This was accounted for by normalising the photocurrent using a reference photo-diode. The current through the reference photo-diode, I_d, was measured and divided by its responsivity, Res_d, to get the incident power:

$$P = \frac{I_d}{Res_d(\lambda)} \tag{3.6}$$

Values for $Res_d(\lambda)$ are tabulated in the photo-diode's manual. For each sample a final value of conductance per unit incident power in S W^{-1} was plotted against wavelength and analysed.

3.3.6 X-ray Fluorescence

X-ray fluorescence spectroscopy (XRF) is a non destructive method of measuring elemental concentrations by measuring the fluorescence emitted by a sample when irradiated with X-rays. The equipment available is a Seiko Instruments SEA1600VX. It measures the elemental composition of a bulk or thin film sample in much the same way as EDX. It illuminates the sample with an X-ray source and analyses the energies of the X-rays emitted from the atoms. The energies of the

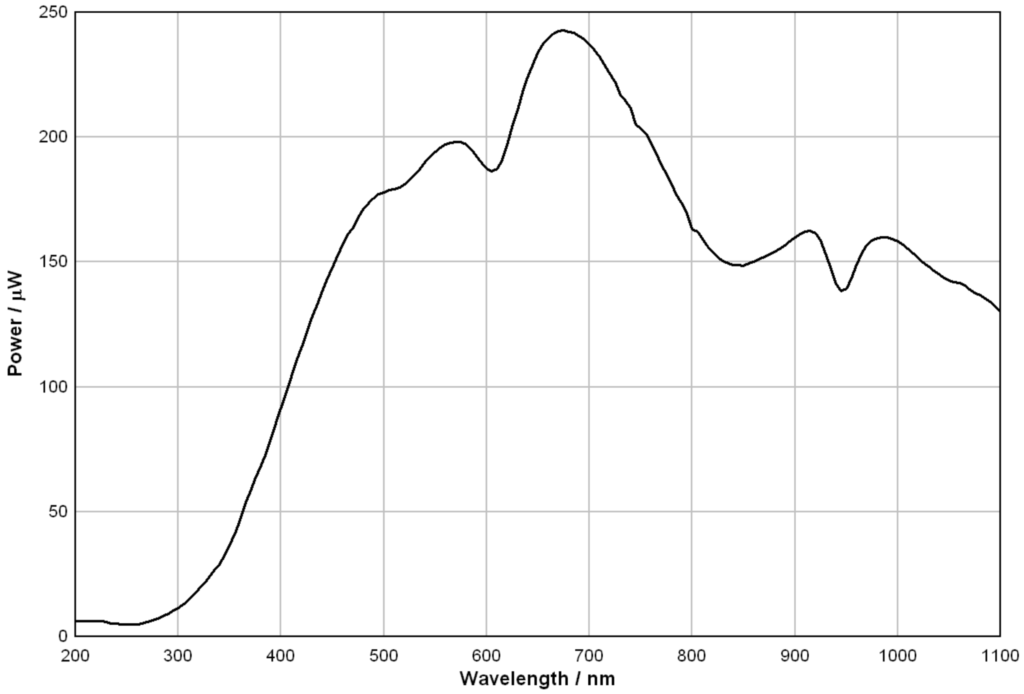

Figure 3.12: Power distribution of light incident on a sample during photoconductivity measurements as a function of wavelength

X-rays are characteristic for each element and can be identified and the relative quantity of each element can be obtained. It has an advantage over EDX in that it is not a vacuum process.

The program controlling the XRF is much more complicated than for EDX but it does allow known standards that are similar to the sample to be loaded to improve accuracy. For bulk analysis bismuth and copper sputtering targets and a pressed sulphur pellet were used as standards. For thin films standards from “Micromatter XRF calibration standards” were purchased. The standard films were mounted on 6.3 µm thick Mylar polyester which is almost invisible to XRF. The copper film was 105.9 $\mu g\,cm^{-3}$, the bismuth film was 90.1 $\mu g\,cm^{-3}$, and the sulphur standard was a film of CuS_x comprising of 84.7 $\mu g\,cm^{-3}$ sulphur and 26.3 $\mu g\,cm^{-3}$ copper. The films were guaranteed to ±5 %. When the film standards were measured and input into the program they were placed on a blank microscope slide to account for any fluorescence or any other signal that may come from the glass slide beneath the thin film samples.

3.4 Summary of Experimental Methods

This chapter outlined all the techniques used in this investigation to partially construct a pseudo binary phase diagram for the CuS−Bi join of the CU−Bi−S material system and then to grow and analyse films of Cu_3BiS_3. Results are in the following chapter.

Chapter 4

Results

The following chapter presents the results obtained during this study and is split into three sections. The first presents the results from the study of the bulk samples of various compositions of the copper-bismuth-sulphur system which are then used to help construct a partial phase diagram in the discussion chapter. This is followed by the results obtained when attempting to grow films of Cu_3BiS_3 using DC magnetron sputtering to deposit a metallic precursor which is then sulphurised by either evaporating a layer of sulphur on top and annealing or annealing with a sulphur pellet. Finally the results from using thermal evaporation to grow films directly using the sulphides of copper and bismuth is presented. In both cases it was shown that films of Cu_3BiS_3 could be gown using these techniques.

Sample	Composition				ED-XRF		Label in mol % Bi
	Mass / g		Molar %		Molar %		
	CuS	Bi	CuS	Bi	CuS	Bi	
1	1.6700	0.3309	91.7	8.3	92.2	7.8	8
2	1.3892	0.6092	83.3	16.7	83.4	16.6	17
3	1.1583	0.8417	75.0	25.0	78.2	21.8	25
4	0.9547	1.0474	66.6	33.4	74.9	25.1	33
5	0.7798	1.2133	58.4	41.6	68.5	31.5	42
5a	1.1846	2.8165	47.9	52.1	-	-	52
6	0.4254	1.5691	37.2	62.8	46.3	53.7	63
6a	0.5813	3.4182	27.1	72.9	-	-	73
7	0.1698	1.8390	16.8	83.2	21.4	78.6	83
8	0.0780	1.9199	8.2	91.8	9.7	90.3	92

Table 4.1: Expected composition from mass measurements and XRF analysis of bulk samples

4.1 Phase Diagram

4.1.1 Composition of Samples

The masses of CuS and Bi used to prepare the bulk samples were measured and are reported in Table 4.1 with their expected composition by calculation and as measured using energy dispersive X-ray fluorescence spectroscopy (ED-XRF). Samples 5a and 6a were made at a later date to fill the compositional gap between samples 5, 6 and 7. Samples 5a and 6a have a total mass of 4 g instead of 2 g.

In all samples there is a drop from the expected bismuth content when measured using ED-XRF. Although, after annealing no film or residue of bismuth was found on the inside of the ampoule or on the ceramic wool. There was no evidence to suggest the sample had lost any material. In addition, the balance used to measure the starting materials had an error of ±0.1 mg. It was calculated that this mass

Sample	Composition / Molar %				Bismuth change
	ED-XRF		WD-XRF		
	CuS	Bi	CuS	Bi	
4	74.9	25.1	74.8	25.2	0.1
7	21.4	78.6	23.2	76.8	−1.8

Table 4.2: Independent verification of XRF measurements, numbers expressed in molar percent

error translated to a maximum of ±0.04 mol % Bi. Due to the complexity of setting up XRF and that it is normally used to measure trace values as opposed to bulk it was decided to continue using the weighted and expected composition values. Samples were subsequently labelled using the expected bismuth content rounded to the nearest percent and will be referred to by their composition in mol % Bi in the following sections.

However, two samples from the first set of bulk samples where sent to be independently verified by the equipment supplier on a Rigaku Primus 1 using wavelength dispersive X-ray fluorescence spectroscopy (WD-XRF). Table 4.2 shows how the resulting analysis compares with that from ED-XRF undertaken at Cranfield University. The bismuth content in sample 4 changes by 0.1 mol % Bi although for sample 7 this difference is −1.8 mol % Bi. Although these agree measuring both bismuth and sulphur using XRF is difficult because the Mα peak of bismuth at 2.42 keV significantly overlaps with the Kα peak of sulphur at 2.308 keV and Kβ peak at2.464 keV. Bismuth content may be measured from another peak such as its L peaks but sulphur has no other peaks to measure therefore great care must be taken to ensure that this overlap is accounted for and it is not clear from the software to what degree it is.

4.1.2 Phase Analysis of Samples

SEM analysis was performed on the surface of each of the samples after they were annealed at 380 °C and the images can be seen in Figure 4.1. In each case a crystal structure can be seen suggesting that there are one or more single phase regions present to form the structures in each sample. Cu_3BiS_3 has an orthorhombic structure and has square and rectangular faces with edges smoothed off by other smaller faces. Other expected phases include metallic bismuth which is monoclinic and appears in blocks with a less obvious crystal shape with serrated edges and CuS which is hexagonal and displays a plate-like structure [54]. Hexagonal plates can be seen in Figures 4.1a to 4.1d suggesting the presence of CuS. In the other samples the structures are less obvious but there appears to be more parallel and perpendicular edges in Figures 4.1f and 4.1h which would be consistent with metallic bismuth and Cu_3BiS_3.

In addition to visual identification, which is only an indication of structure, the pellets were ground to a powder in a ball mill and XRD was performed on them to confirm which phases are present. The diffractograms of each pellet are shown in Figure 4.2. In general Cu_3BiS_3 (wittichenite, ICDD number 43-1479) was identified in all but the last sample and metallic bismuth was present in samples with a bismuth content greater than 25 mol % Bi. As bismuth content increases above 25 mol % Bi the peaks corresponding to Cu_3BiS_3 decrease in intensity and the peaks corresponding to the metallic bismuth phase increase. Below 25 mol % Bi the bismuth phase was absent and another phase appeared alongside Cu_3BiS_3 and was identified as CuS. However, these two phases do not account for a peak at $2\theta = 46.5°$ in the 8 mol % Bi and 17 mol % Bi samples. This peak could belong to

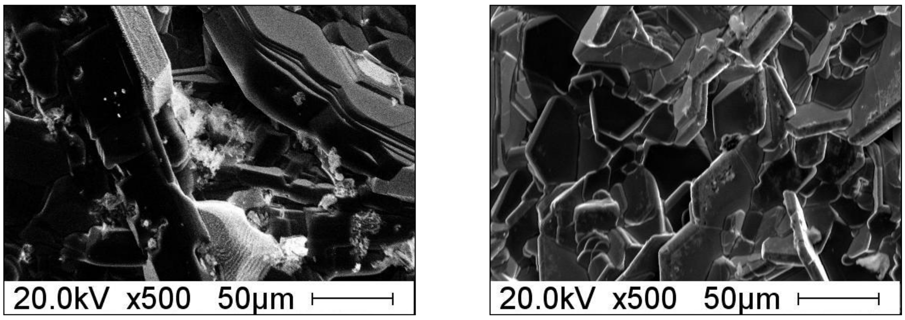

(a) 8 mol % Bi **(b)** 17 mol % Bi

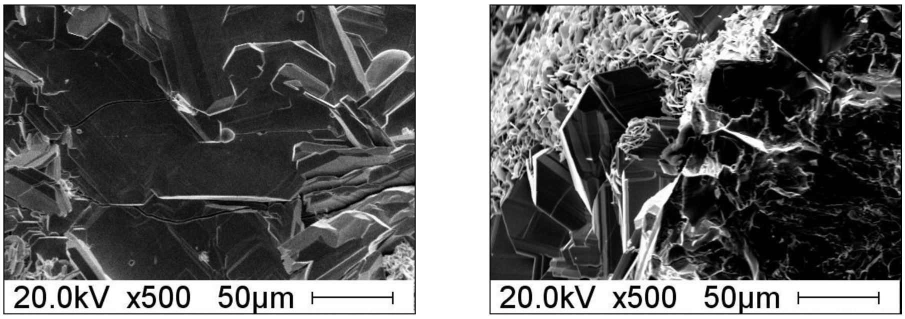

(c) 25 mol % Bi **(d)** 33 mol % Bi

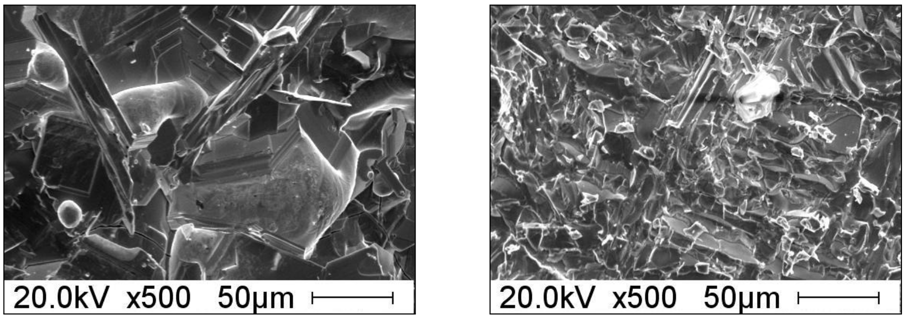

(e) 42 mol % Bi **(f)** 63 mol % Bi

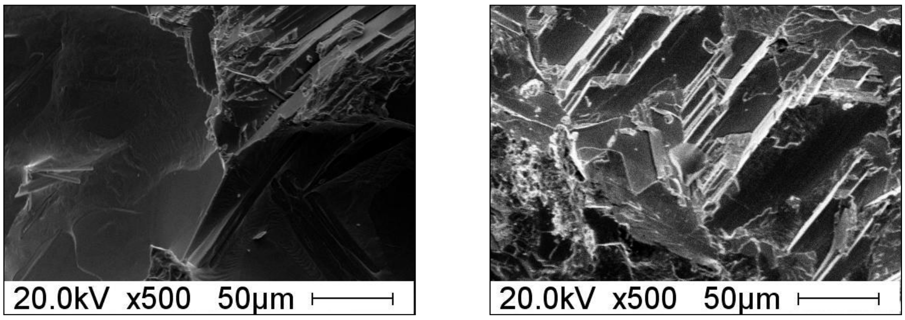

(g) 83 mol % Bi **(h)** 92 mol % Bi

Figure 4.1: SEM showing crystalline formations on the surface of the bulk samples after annealing at 380 °C

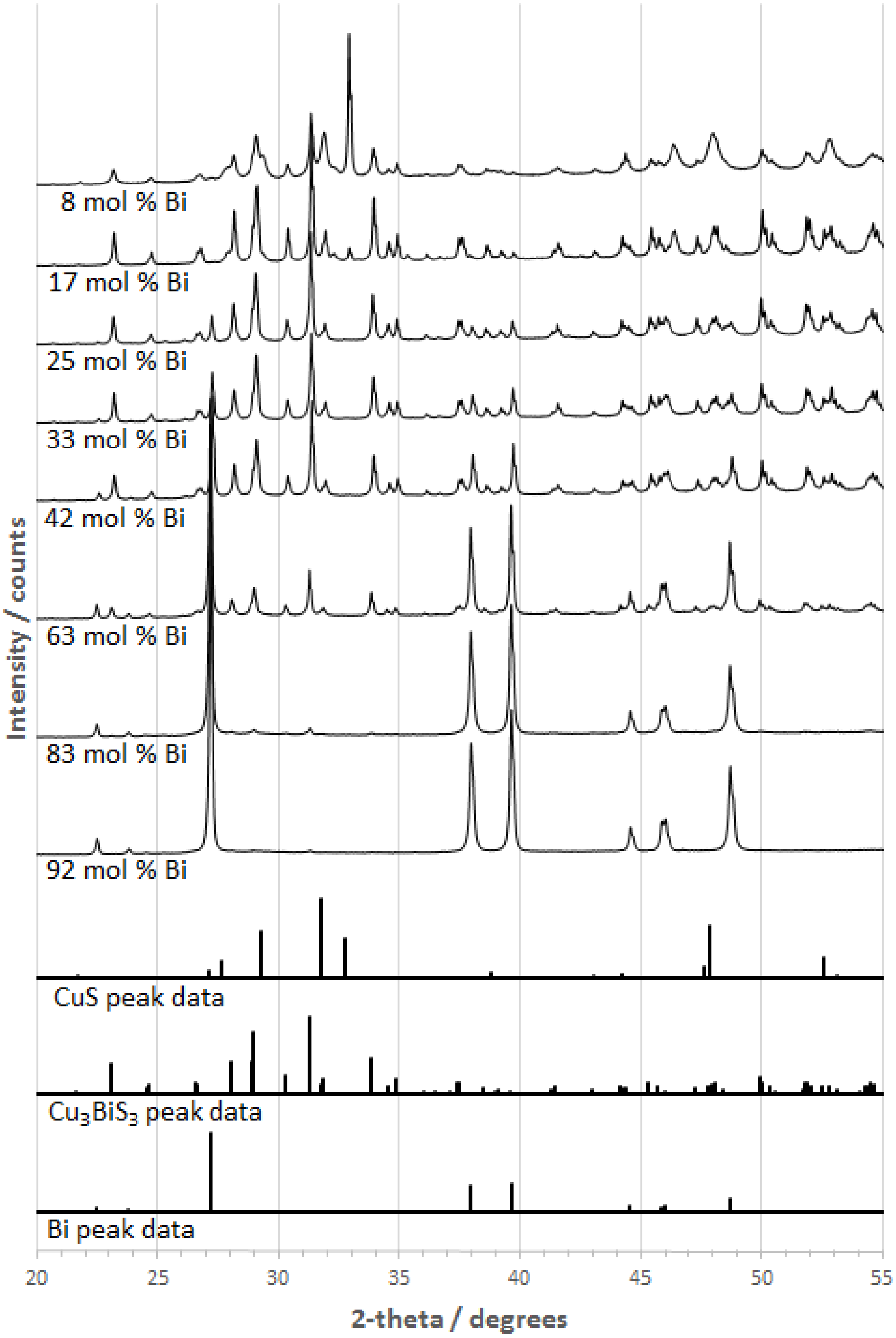

Figure 4.2: XRD showing phases present in the bulk samples after annealing at 380 °C

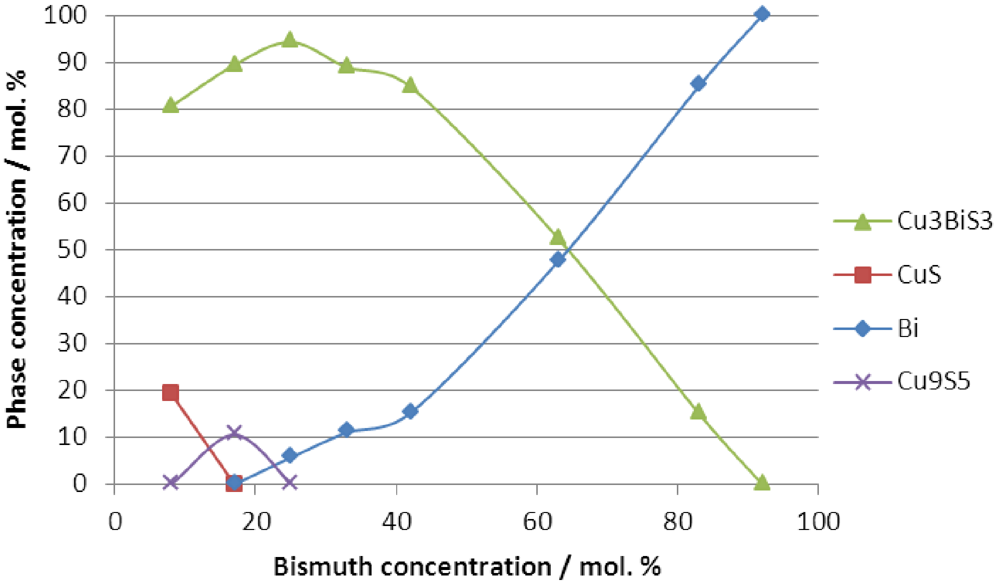

Figure 4.3: Relative phase composition of bulk samples after annealing at 380 °C as determined by using Topas profile fitting software

another copper sulphide phase but was unidentified by visual analysis. Cu_3BiS_3 has many peaks so there is greater potential that its diffraction pattern can hide the patterns of other less intense patterns.

The diffractograms were also analysed using Topas profile fitting software to get the relative abundance of each phase and the results are presented in Figure 4.3. Topas is a software analysis technique that attempts a quantitative approach and shows that above 25 mol % Bi the decrease of the Cu_3BiS_3 phase and increase of the bismuth phase is linear with mol % Bi content. Below 25 mol % Bi Topas analysis was able to match CuS to the 8 mol % Bi but only a Cu_9S_5 phase to the 17 mol % Bi sample. Although, Cu_9S_5 could not be confirmed by visual analysis of the diffractogram partly due to the high number of peaks. In both cases these are copper sulphides and the amount of Cu_3BiS_3 decreases linearly with falling bismuth content in samples below 25 mol % Bi.

Overall, the results from XRD correspond to the visual results from SEM. Copper sulphides were found on samples below 25 mol % Bi where plate structures were seen in the SEM images and only Cu_3BiS_3 and metallic bismuth was found on samples above 25 mol % Bi where more orthogonal angles were observed.

4.1.3 DSC Analysis of Samples

DSC was performed on 50 mg aliquots of each powdered sample. They were placed in open 70 µl alumina crucibles then heated and cooled at a rate of 5 °C min^{-1} from 0 °C to 700 °C and down again (or in the case the of 52 mol % Bi and 73 mol % Bi samples 50 °C to 650 °C). This was cycled through three times and the heating curves of the third run are shown in Figures 4.4 and 4.5. The third set of heating curves where used to mitigate against the effects of the thermal history of the samples and any super cooling that might occur. All the curves show a general downward background curve with several downward peaks, both sharp peaks and broad peaks which represent endothermic events corresponding to phase boundaries at that particular composition. These peaks can be broadly collected together into groups based on their shapes, positions and relative amplitudes.

All the curves have a similar sharp peak at about 270 °C which increases in size with increasing bismuth content. This group of peaks has been named Group A. The first five curves have an additional sharp peak at approximately 635 °C. These peaks decrease in size with increasing bismuth content and have been grouped into Group B. On each of the first five curves and between the peaks identified above there appears to be a step up and a step down again. This is most clearly seen on the 25 mol % Bi curve. The neighbouring curves also contain these features but

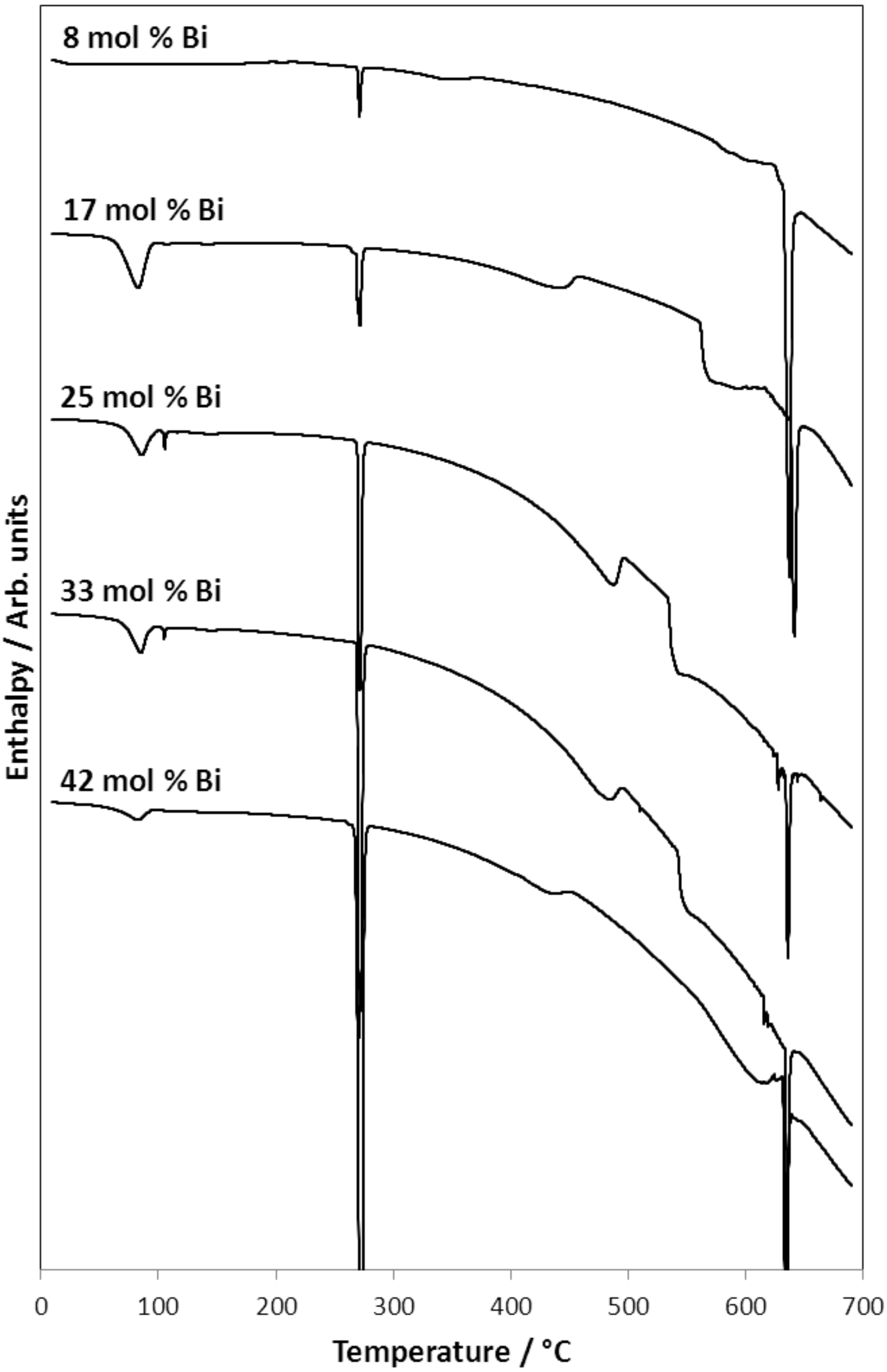

Figure 4.4: DSC heating curve showing endothermic events of samples 8 mol % Bi to 42 mol % Bi

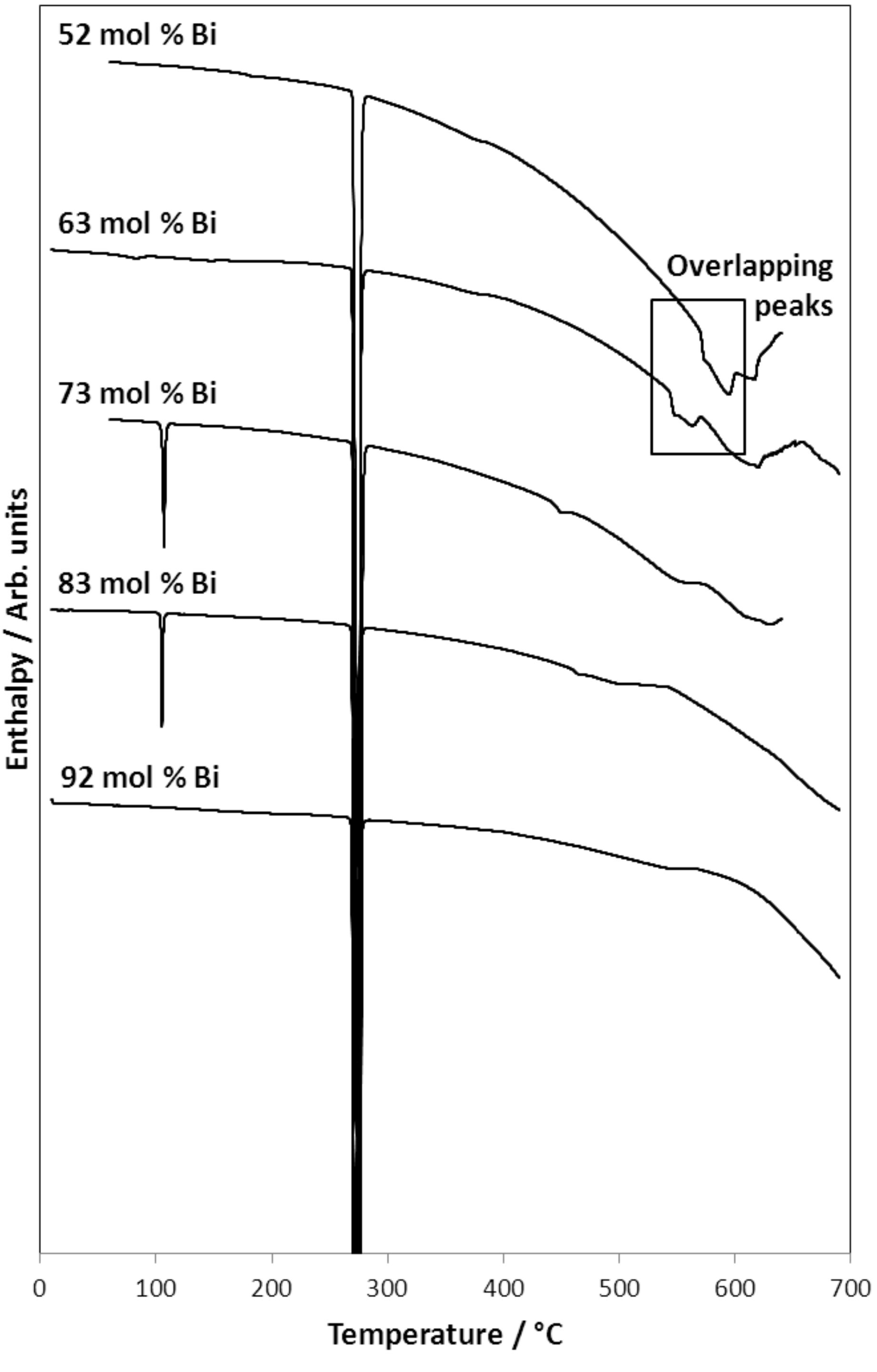

Figure 4.5: DSC heating curve showing endothermic events of samples 52 mol % Bi to 92 mol % Bi

they are less pronounced the further from 25 mol % Bi the curve is. Each step up has been grouped together into Group C and each step down has been grouped together into Group D. The results in terms of groups is explored more detail in Section 4.1.4.

On the five remaining curves (≥52 mol % Bi) there appears to be fewer events after the main sharp peak at 270 °C and those present are more shallow and less obvious. On the 52 mol % Bi and 63 mol % Bi curves there are two overlapping peaks just below 600 °C. They are labelled in Figure 4.5 and are discussed in Section 4.1.6. There are also some low temperature events around 100 °C on several of the curves.

Each of the events identified on the heating curves was recorded. Temperature, the point on the curve at which the temperature was taken, and enthalpy per unit mass of each thermal event is summarised in Table 4.3. From this table it is possible to see the patterns related to the groups of events listed above. For example each sample has an event occurring at around 270 °C. To help visualise how the events relate to the phase diagram they were plotted on a composition verses temperature plot. This plot can be seen in Figure 4.6. Each event is represented by a circle and the area of the circle is proportional to the enthalpy per unit mass of the event. The proposed groups outlined above due to common features and possible relationships are grouped and marked on this plot and are explored in more depth in Section 4.1.4.

Composition / mol % Bi	Temperature / °C	Feature	Enthalpy / J g^{-1}
8	77	Onset	−0.13
	270	Onset	−0.95
	343	Peak	−1.44
	573	Onset	−0.16
	632	Onset	−14.21
17	65	Onset	−6.66
	107	Peak	−0.09
	143	Peak	−0.21
	268	Onset	−2.71
	435	Peak	−6.31
	561	Onset	−12.65
	638	Onset	−6.91
25	72	Onset	−3.37
	104	Onset	−0.27
	115	Onset	−0.06
	146	Peak	−0.35
	269	Onset	−7.01
	485	Peak	−9.38
	534	Onset	−16.25
	633	Onset	−5.10
33	71	Onset	−2.84
	104	Onset	−0.20
	145	Peak	−0.18
	269	Onset	−11.15
	477	Peak	−6.05
	542	Onset	−9.22
	632	Onset	−5.89
42	63	Onset	−1.62
	144	Peak	−0.18
	269	Onset	−23.58
	431	Peak	−2.50
	561	Onset	−6.49
	632	Onset	−7.63

Table 4.3: Thermal events identified from DSC heating curves

Composition / mol % Bi	Temperature / °C	Feature	Enthalpy / J g^{-1}
52	270	Onset	–29.88
	375	Peak	–0.37
	569	Onset	–0.92
	594	Peak	–4.94
63	67	Onset	–0.39
	146	Peak	–0.54
	269	Onset	–37.93
	373	Peak	–0.25
	543	Onset	–0.62
	562	Peak	–2.36
73	105	Onset	–2.41
	269	Onset	–40.95
	451	Peak	–0.60
	546	Peak	–4.79
	607	Peak	–1.16
83	104	Onset	–1.25
	120	Peak	–0.01
	269	Onset	–44.85
	460	Onset	–0.20
	499	Peak	–0.53
92	181	Peak	–0.49
	269	Onset	–44.21
	540	Peak	–2.07
100	269	Onset	–51.90

Table 4.3: Thermal events identified from DSC heating curves (cont.)

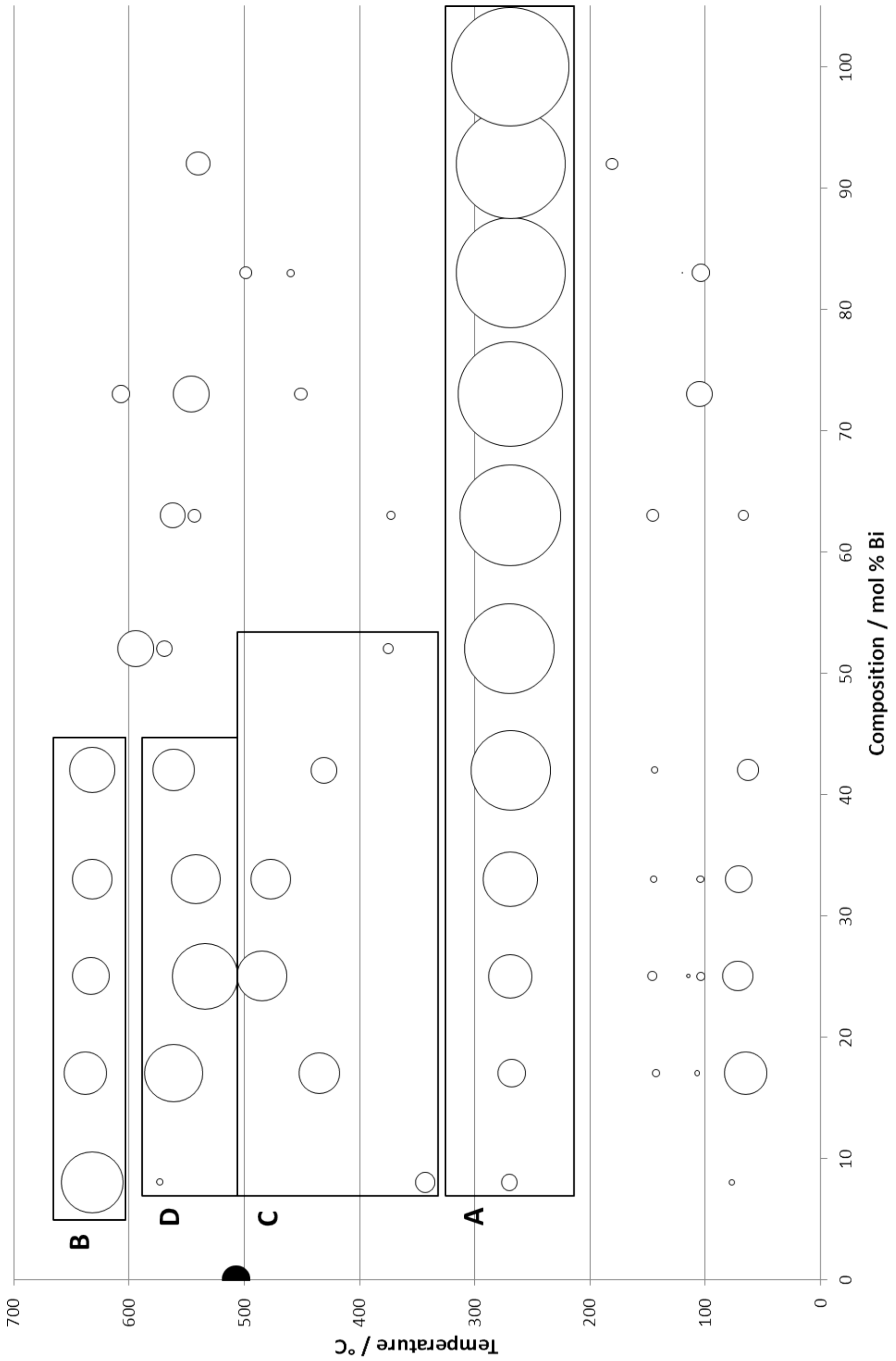

Figure 4.6: Bubble plot showing temperature of thermal events at each composition, bubble area is directly proportional to enthalpy

4.1.4 Analysis of Groups of Peaks

A Tammann diagram is a plot of enthalpy against composition and can be useful in confirming suspected trends. It can also be used to more accurately find a eutectic composition or the compositional limit to a thermal activity by extrapolating the enthalpy to zero [52]. In the following sections the Tammann diagram of each group of peaks along with the temperature of each event in each group are reported.

Group A

The curves in Group A have a similar sharp peak at about 270 °C which increases in size with increasing bismuth content. They occur on all the DSC curves. Figure 4.7 shows the Tammann Diagram for this group where it can be seen that the enthalpy does increase with increasing bismuth content suggesting this peak is related to a change in the bismuth phase. The enthalpy appears to vanish at about 5 mol % Bi. The onset temperature of the all the peaks occur close to melting point of bismuth which is 271.5 °C. These peaks have been identified as the melting of bismuth which is an endothermic process at a well defined temperature and would result in a sharp downward peak as observed.

Group B

The first five curves ($<$50 mol % Bi) have an additional sharp peak at around 635 °C. The Tammann diagram for Group B, Figure 4.8, shows the enthalpy decreases to a central minimum at approximately 25 mol % Bi then increases again with increasing Bi content. This would suggest that it is the boundary of a two phase region. In a two phase region the the closer to the region's compositional boundary

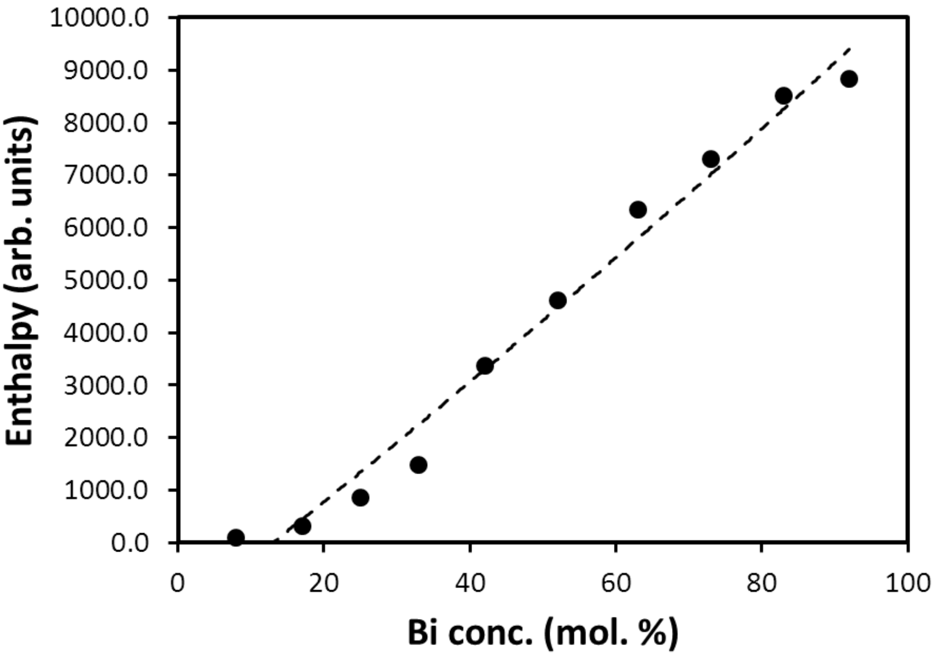

(a) Tammann diagram of Group A

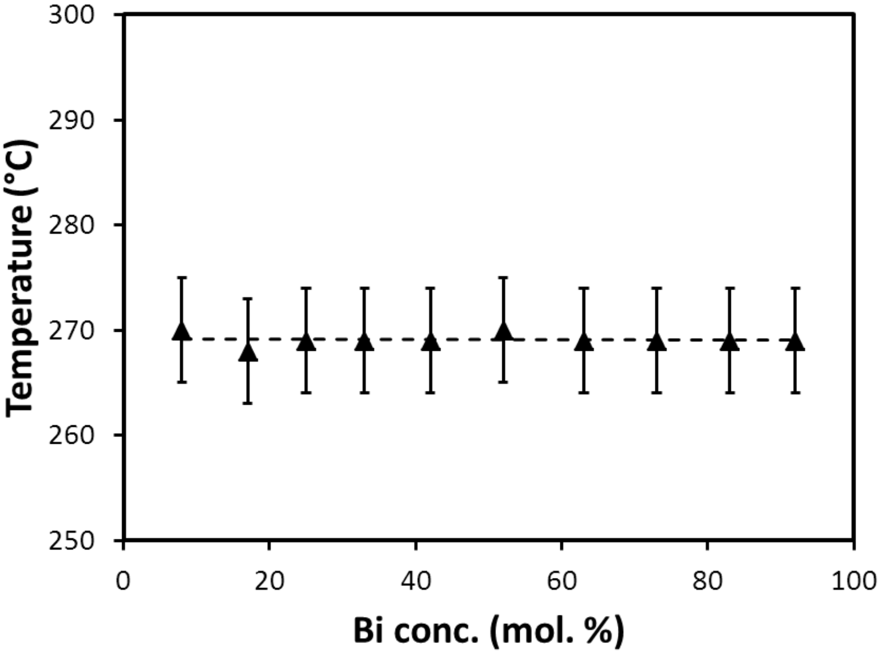

(b) Temperatures of Group A

Figure 4.7: Tammann and temperature plots for thermal events in Group A

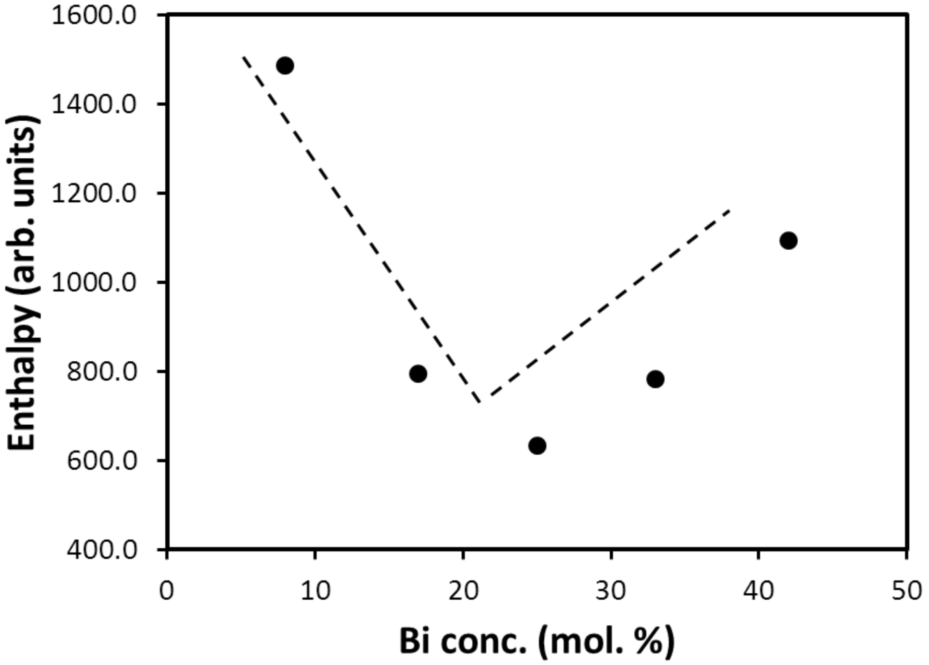

(**a**) Enthalpies of Group B

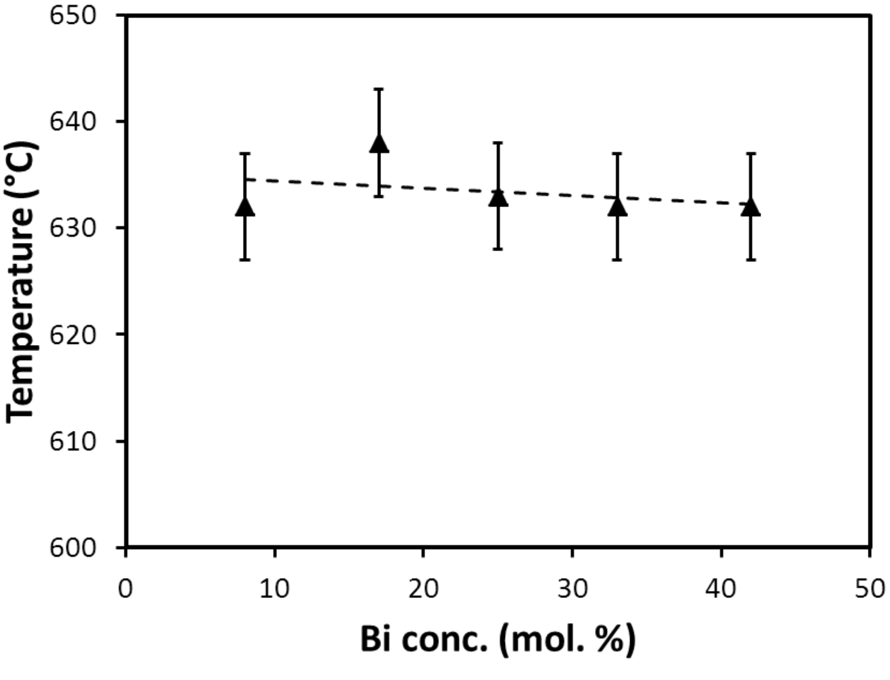

(**b**) Temperatures of Group B

Figure 4.8: Tammann and temperature plots for thermal events in Group B

the more dominate the features of a single bordering phase are which would explain the increase in enthalpy observed at either end of these series of peaks.

Group C

The peaks in Group C appear as an upward step in the first six DSC curves. On closer inspection these are more likely to be very broad downward peaks. Since taking an onset temperature would be very difficult and introduce an unsatisfactory level of uncertainty the temperature of the peaks minimum value was taken instead. Although this is different from the other types of peaks it is consistent within this series of peaks and allows for better comparison. The temperature of these events increases to 485 °C at 25 mol % Bi then decreases again with increasing Bi content.

The Tammann diagram for Group C, Figure 4.9, shows the enthalpy is maximum at 25 mol % Bi suggesting this boundary is associated with a phase change. Most likely Cu_3BiS_3 as this is the phase that fits the stoichiometry at this position and is the dominant phase in the XRD analysis for the 25 mol % Bi sample. When the enthalpy is linearly extrapolated in either direction to zero the compositional boundaries of event C can be found to be at 5 mol % Bi and 52 mol % Bi using the trend line equations $y = 59.615x - 314.13$ and $y = -41.64x + 2178$ respectively. This would suggest that whatever phase change is represented by these curves starts and ends at 5 mol % Bi and 52 mol % Bi respectively.

Group D

The peaks in Group D appear as an downward step in the DSC curves. This looks like a sharp peak with a long tail, in this case the onset temperature was taken. The temperature of these events decreases to 534 °C at 25 mol % Bi then increases

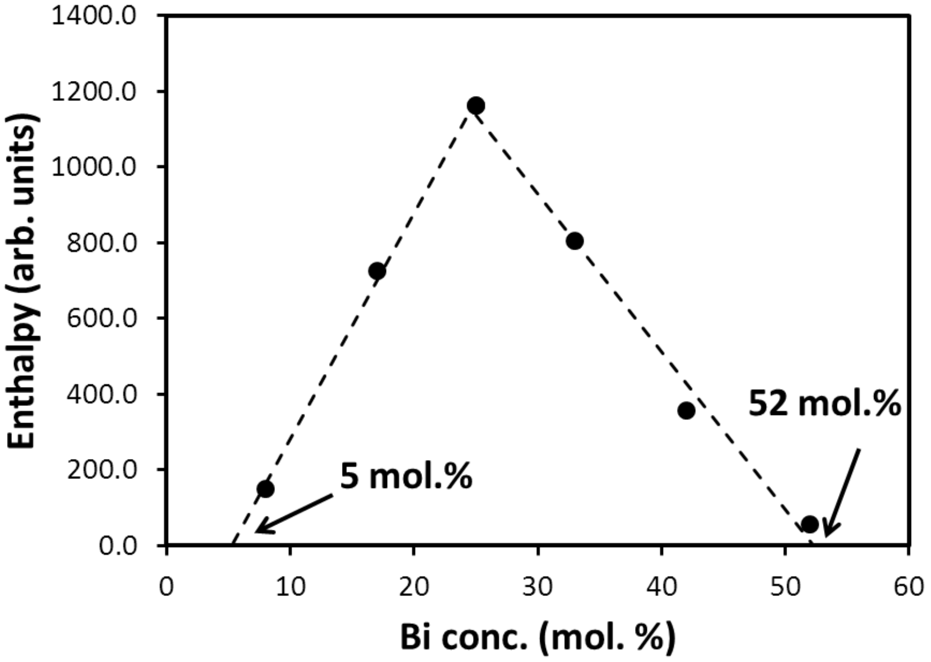

(a) Enthalpies of Group C

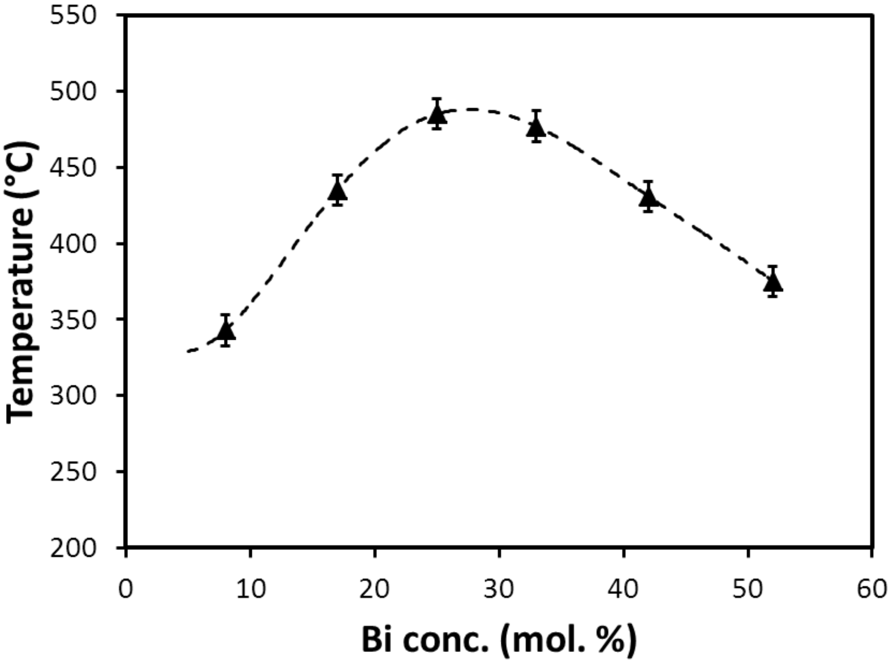

(b) Temperatures of Group C

Figure 4.9: Tammann and temperature plots for thermal events in Group C

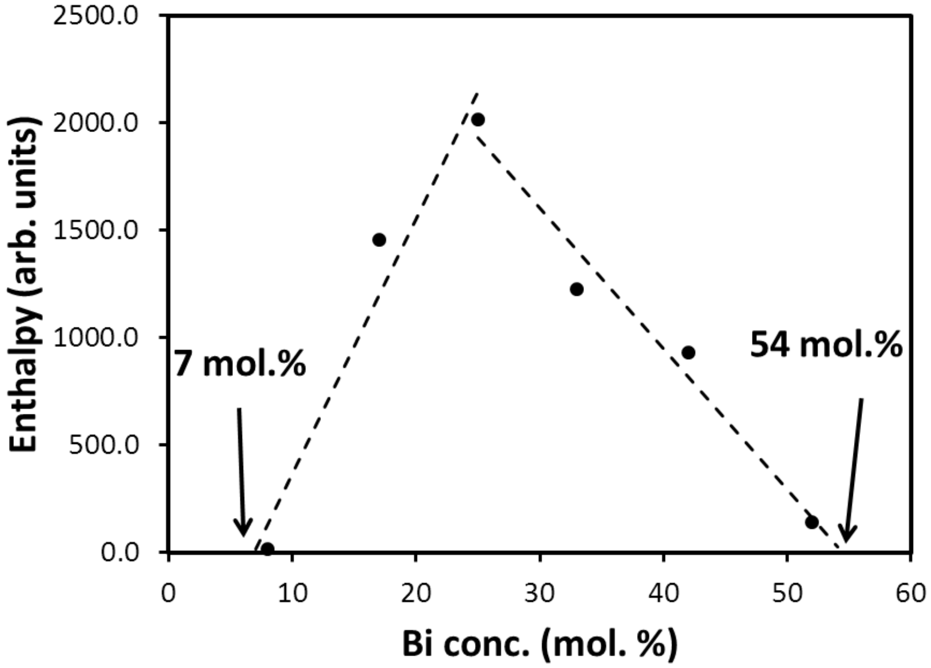

(a) Enthalpies of Group D

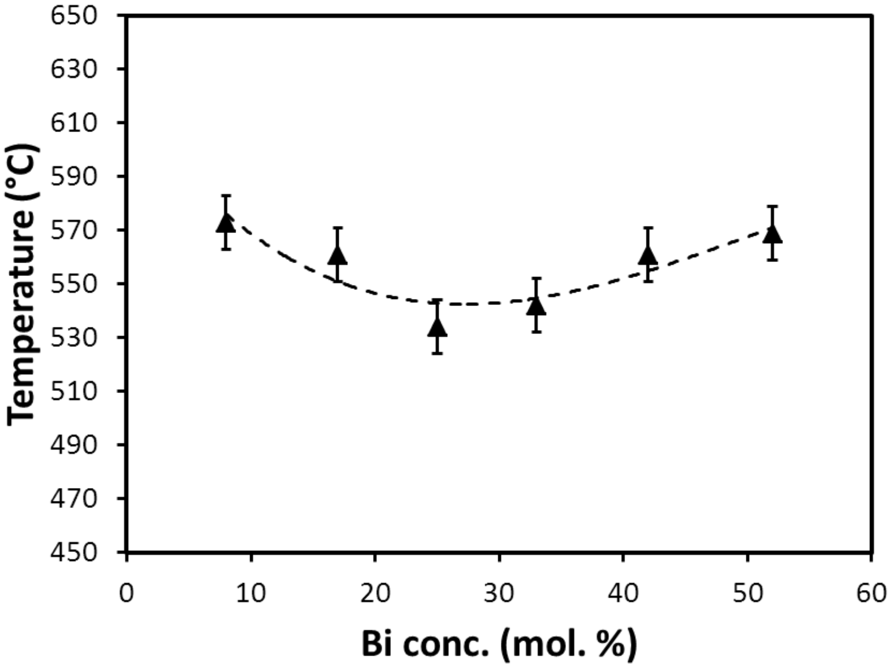

(b) Temperatures of Group D

Figure 4.10: Tammann and temperature plots for thermal events in Group D

again with increasing Bi content.

The Tammann diagram for Group D, Figure 4.10, shows the enthalpy is maximum at 25 mol % Bi suggesting this boundary is associated with a phase change of Cu_3BiS_3 like in Group C. When the enthalpy is linearly extrapolated in either direction to zero the compositional boundaries of event D can be found to be at 7 mol % Bi and 54 mol % Bi using the trend line equations $y = 118.37x - 811.46$ and $y = -65.542x + 3568.7$ respectively.

4.1.5 DSC Analysis of Starting Materials

Powdered Bismuth and Copper Sulphide where used as the starting materials and also represent the edges of the CuS−Bi phase diagram. DSC was run on each material and the heating curves are shown in Figure 4.11.

Bismuth showed a single sharp peak with onset temperature of 269 °C and enthalpy of −51.90 J g^{-1}. This was expected from the phase diagram of bismuth[46], shown in Figure 4.22, which shows the melting point of bismuth to be 271.5 °C. This point as been added to the bubble plot and table of thermal events.

The first heating curve for copper sulphide showed many features that were not expected from the Cu−S phase diagram [55]. The Cu−S phase diagram shows CuS decomposes peritectically at 507 °C to $Cu_{2\text{-}x}S$ (or Cu_9S_5) and liquid. There is a further phase change at 813 °C but that is above the temperature range of this study. Figure 4.11 shows many more events, these could be other processes such as amalgamation of the power or wetting of the ampoule. The CuS sample would have benefited from being run two more times like the mixed samples but it appeared to de-gas and dirty the insides of the DSC furnace. It was decided not

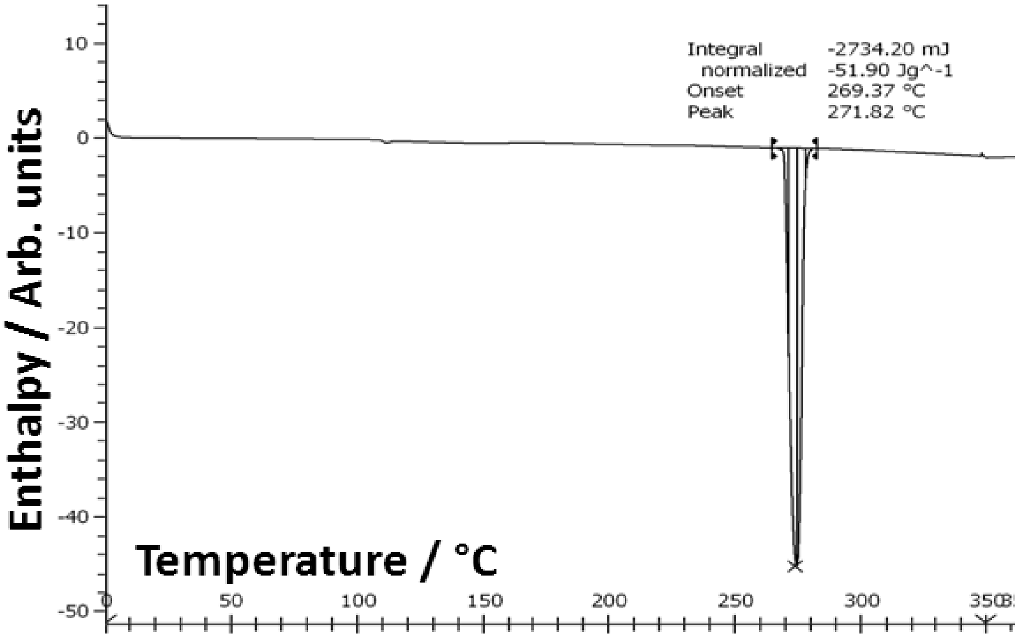

(a) DSC heating curve of bismuth showing bismuth's melting point at 269.37 °C

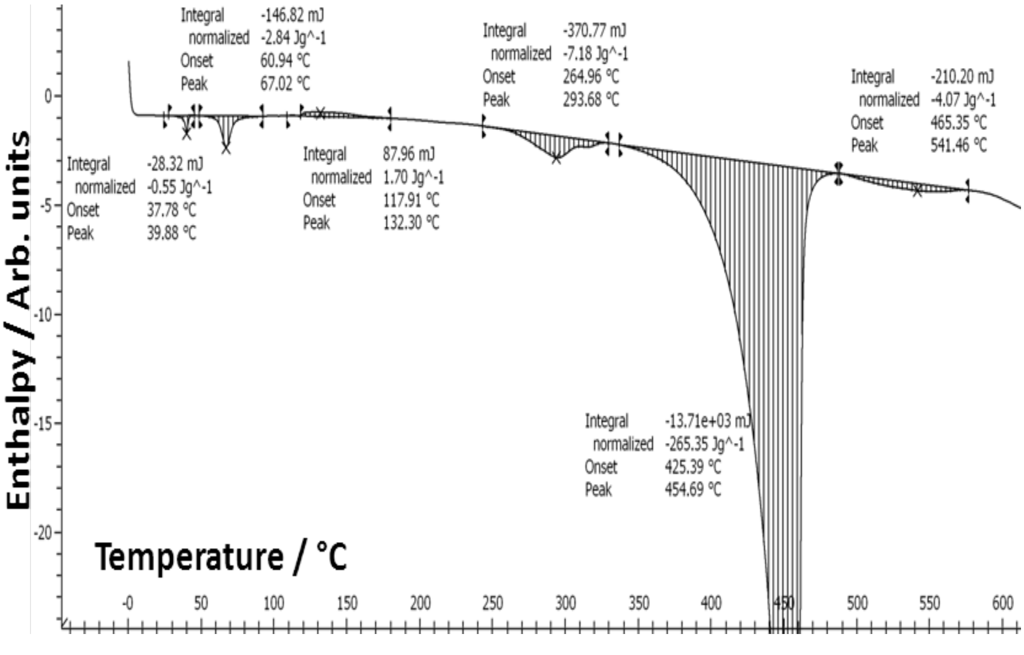

(b) DSC heating curve of copper sulphide

Figure 4.11: DSC heating curves of bismuth and copper sulphide

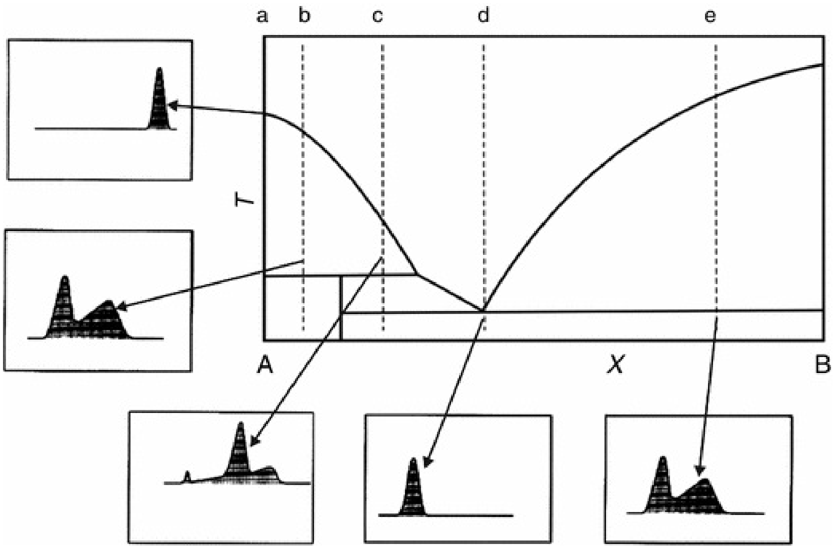

Figure 4.12: Correlation between topology of phase diagram and shape of DSC curve [52]

to continue with a second and third run and values for the CuS side of the phase diagram were taken from literature instead. The phase change at 507 °C is noted on the bubble plot as a solid semicircle because we do not have an enthalpy value for it.

4.1.6 Deconvolution of Overlapping Peaks

The 52 mol % Bi and 63 mol % Bi curves appear to have two similar features that look like overlapping peaks, they are marked in Figure 4.5. This is common in DSC curves and is related to the shape of the phase diagram for the material system [52]. Figure 4.12 shows some examples of this, the DSC curves for compositions at ‘b’ and ‘e’ show a sharp peak followed by a broad peak.

When a pure component goes though a phase change such as melting a sharp peak is observed. For ‘e’ this is the case at the horizontal line on the phase diagram. When there are other components present the peaks are broader with blunt maxima [56]. This is the case within the region above the horizontal line since that now contains a mixture of phases from either side of the region in accordance with the level rule. As the temperature increases the proportions of the phases change due to the slope of the liquidus. The proportion of liquid in this region increases with temperature as part of the phase mixture melts over a wide range of temperatures. This contributes many small peaks to the DSC curve which, when added together, smooth out to give a broad blunt peak. Therefore, it would be reasonable to assume that modelling the overlapping peaks as a series of smaller peaks would be a good approximation when trying to separate the sharp peak from the broad peak.

Each set of overlapping peaks has a single measured enthalpy value obtained from the integral over the whole feature. MagicPlot Student fitting software [57] was used to attribute an enthalpy value to each peak by fitting six Gaussian curves to each feature, as shown in Figure 4.13. The first two Gaussian curves were attributed to the first sharp peak and the latter four attributed to the second broad peak. For clarity the sloping background has been removed and the curves negated so positive values can be used in the calculations. The relative areas of the Gaussians were compared and the enthalpy split in the same proportion as shown in Table 4.4. These values were added to the bubble plot and the table of thermal events in Section 4.1.3.

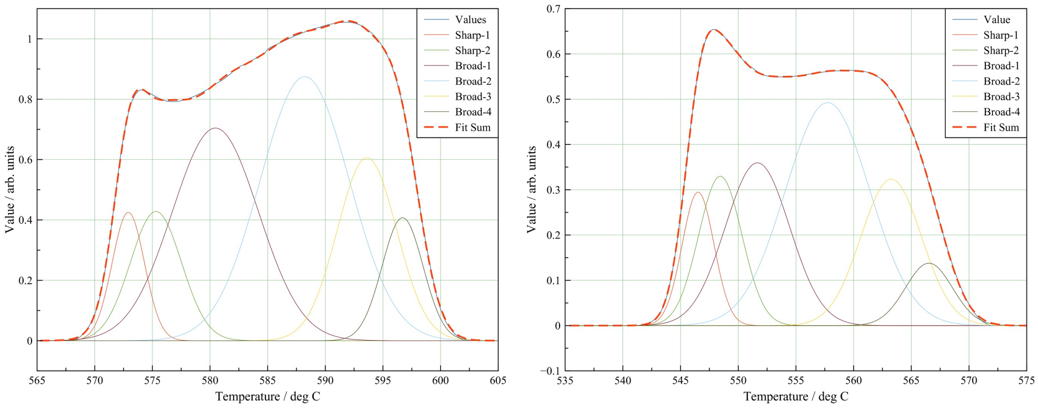

(a) 52 mol % Bi Feature **(b)** 63 mol % Bi Feature

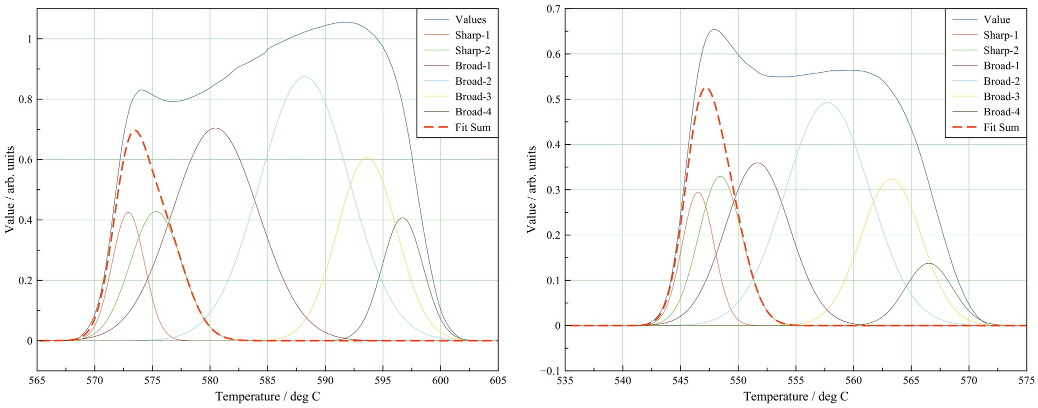

(c) 52 mol % Bi Sharp Peak **(d)** 63 mol % Bi Sharp Peak

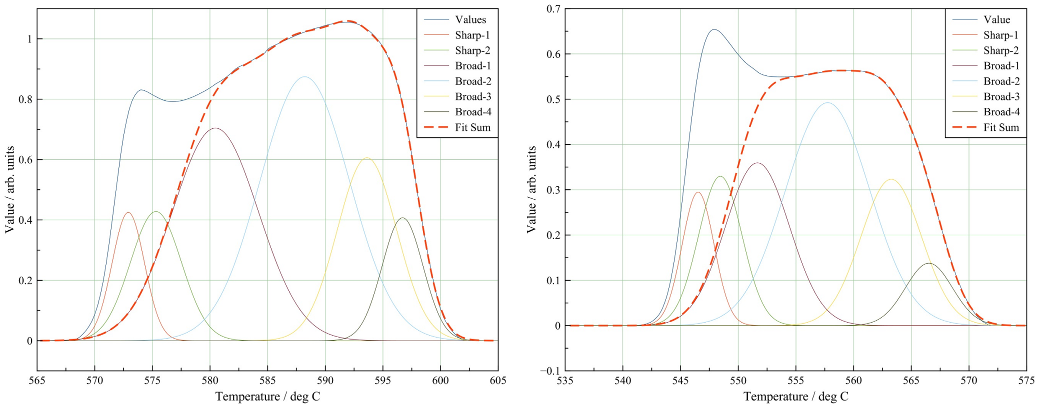

(e) 52 mol % Bi Broad Peak **(f)** 63 mol % Bi Broad Peak

Figure 4.13: Fitting of Gaussian curves to overlapping peaks. In each case the sharp peak can be approximated with two Gaussian curves and the remaining broad peak can be approximated by a further four Gaussian curves

Composition / mol % Bi	Peak	Gaus. Area / Arb. units	Percent area of feature	Enthalpy / J g^{-1}
52	Both	24.70	100.00	−5.86
	Sharp	3.87	15.69	−0.92
	Broad	20.82	84.31	−4.94
63	Both	12.44	100.00	−2.98
	Sharp	2.58	20.71	−0.62
	Broad	9.87	79.29	−2.36

Table 4.4: Deconvolution of overlapping peaks by attributing enthalpy to each feature in proportion to its area

4.1.7 Surface of Samples after DSC

Images of the surfaces of the aliquots after being used for DSC were taken using SEM and are shown in Figure 4.14. The SEM was set to measure back scattered elections because it was difficult to get an image with secondary electrons. Each of the images show a plate like crystalline structure except for the last two which show whiskers on the surface of the higher bismuth content samples.

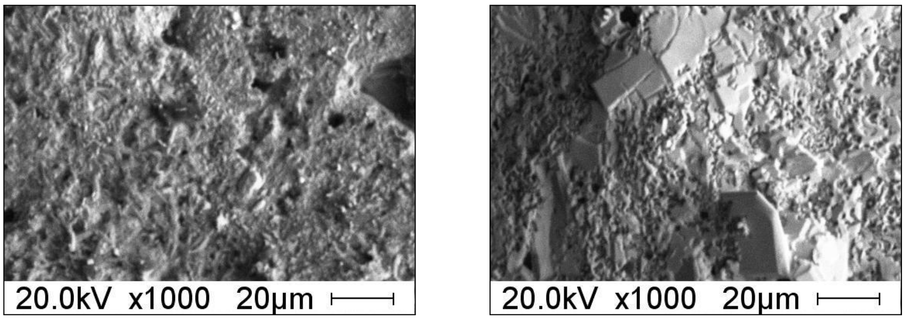

(a) 8 mol % Bi **(b)** 17 mol % Bi

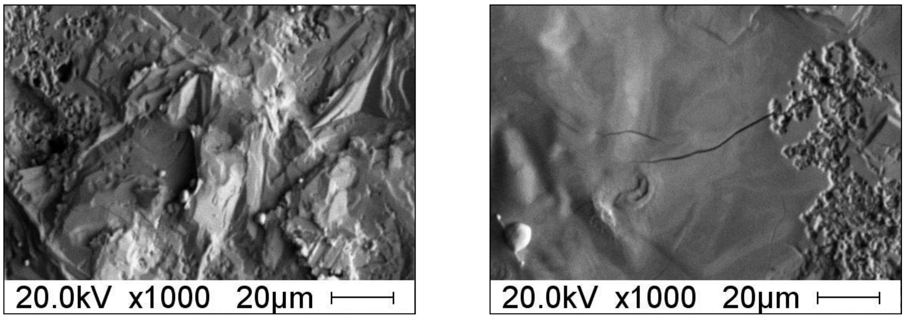

(c) 25 mol % Bi **(d)** 33 mol % Bi

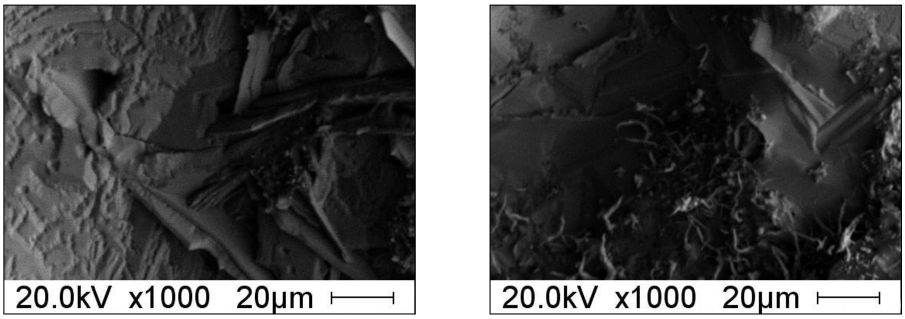

(e) 42 mol % Bi **(f)** 63 mol % Bi

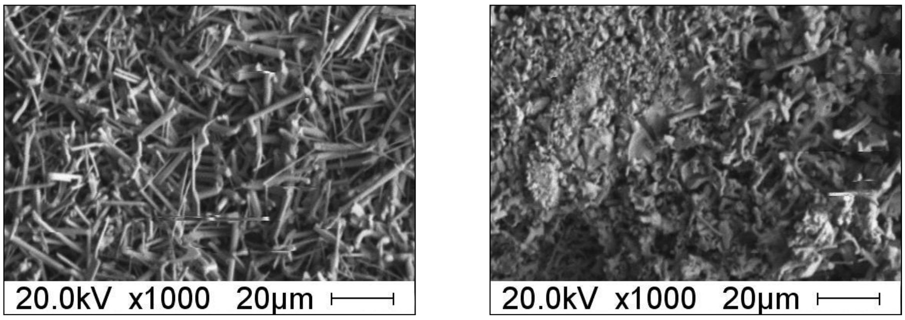

(g) 83 mol % Bi **(h)** 92 mol % Bi

Figure 4.14: Rutherford back scattering detector (RBSD) imaging of the surfaces of the DSC aliquots at ×1000 magnification

4.1.8 Phase Analysis of Samples heated to 510 °C

Six of the bulk samples where pressed back into pellets, resealed in ampoules, and heated to 510 °C and then quenched in liquid nitrogen after 10 days. 510 °C was chosen as this lies between the temperature range of the thermal events in Group C and Group D. If a phase change happened at the events of Group C then different phases should be detected with XRD. A fragment a each pellet was broken off, mounted in resin and polished. SEM images where impossible to obtain because of a large charge build up making it difficult to focus even though silver dag was used on the edge of each sample to ground it. This would suggest the samples themselves where not conducting. Light microscopy was used instead and the images can be seen in Figure 4.15. Despite the lower magnification it can be seen that there are different phases present. The first two samples clearly show two separate phases with possibly a third phase in the first sample. The middle two appear more homogeneous, the blue in the third samples is probably corrosion and the voids in the last two samples would suggest they are more porous than the others.

The remaining pellets were ground to a powder and XRD was performed on them to detect the phases present. The diffractograms of three of the pellets are shown in Figure 4.16. The samples with bismuth content of 25 mol % Bi, 33 mol % Bi and 63 mol % Bi had too many peaks to successfully identify any phases. The first two samples (8 mol % Bi and 17 mol % Bi both had Cu_3BiS_3 and two copper sulphide phases, CuS and Cu_9S_5. As expected in the 42 mol % Bi sample a bismuth phase was detected but a BiCuOS phase was also detected indicating the sample was contaminated at some point during the second anneal.

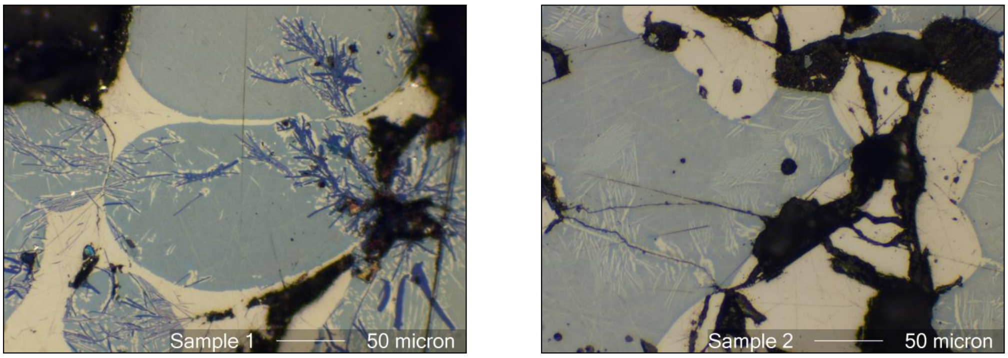

(a) 8 mol % Bi **(b)** 17 mol % Bi

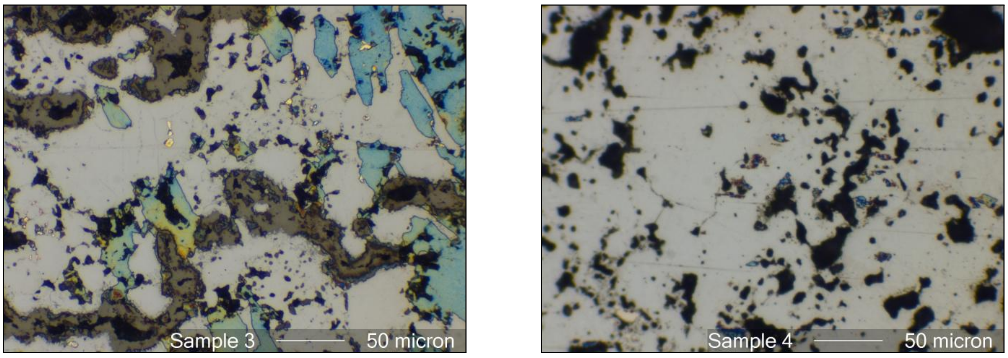

(c) 25 mol % Bi **(d)** 33 mol % Bi

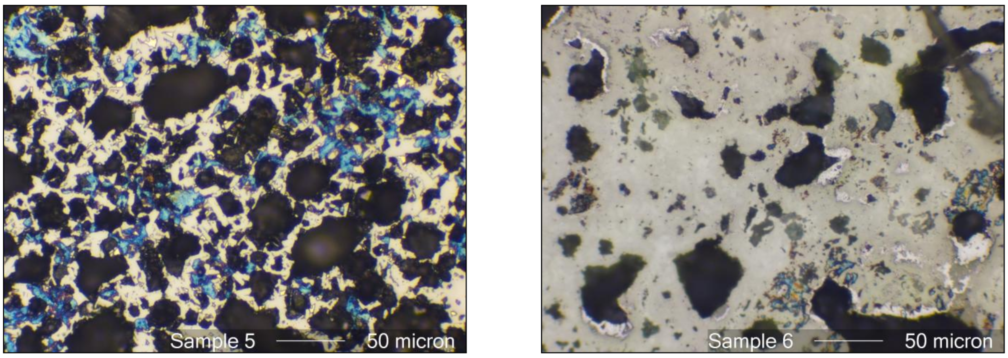

(e) 42 mol % Bi **(f)** 63 mol % Bi

Figure 4.15: Light microscopy showing the phase regions within the bulk samples annealed at 510 °C

This may have happened the other three samples too making them harder to analyse.

There are unlikely to contribute much to the final phase diagram.

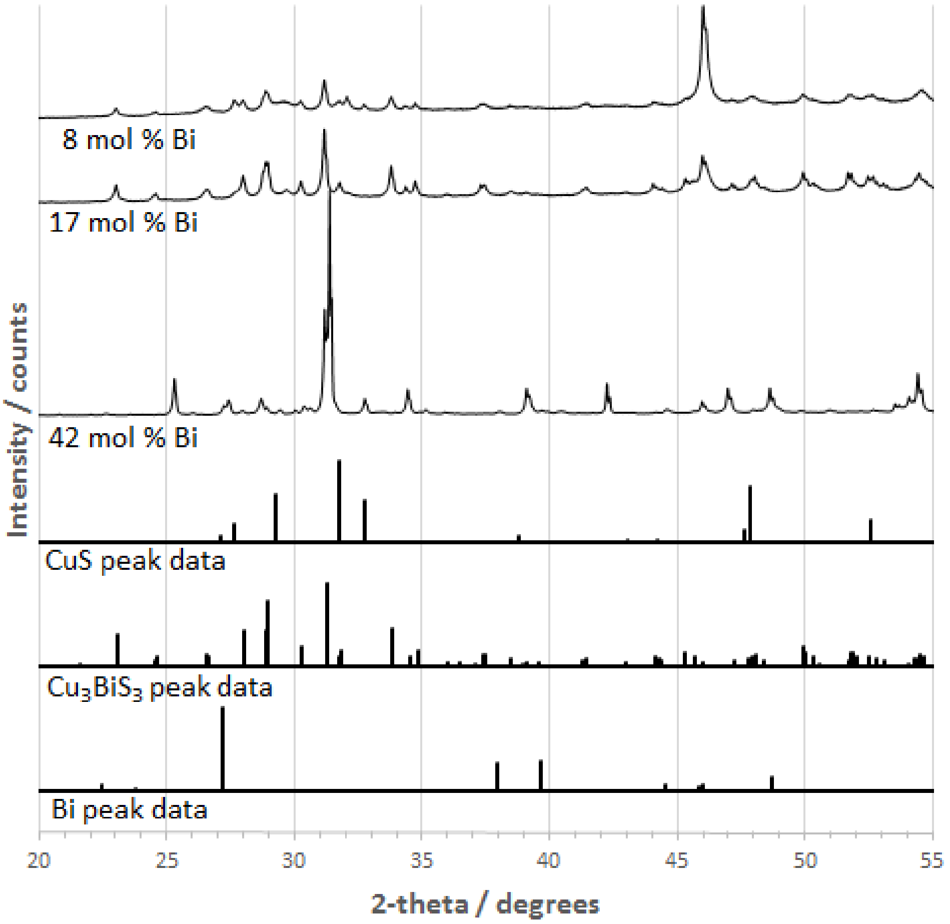

Figure 4.16: XRD showing phases present in three of the bulk samples after annealing at 510 °C

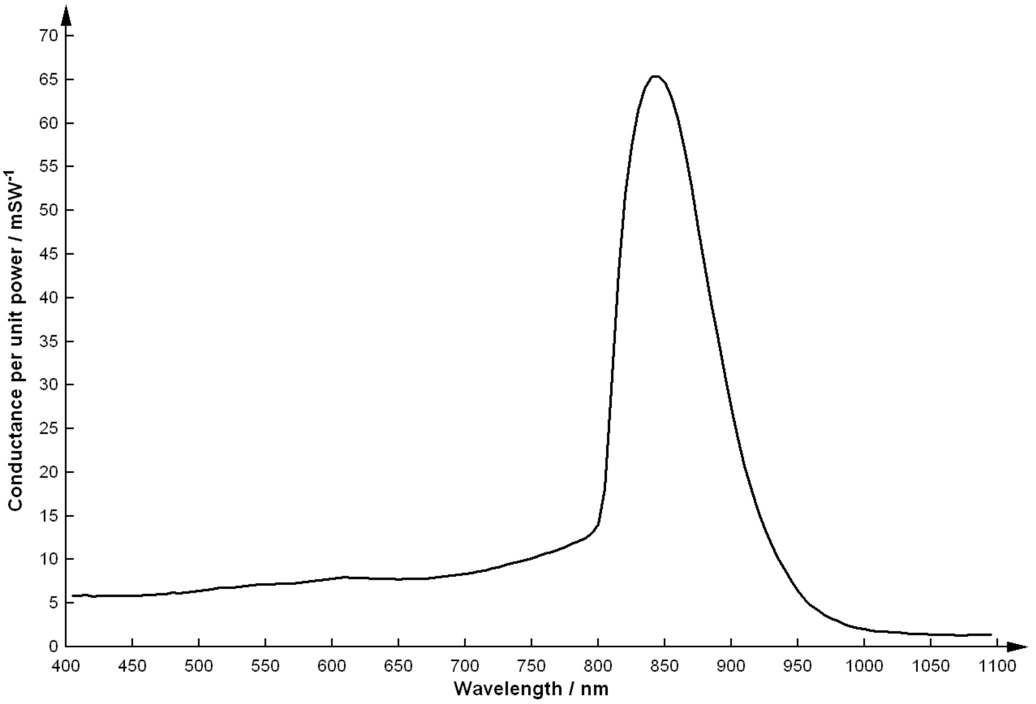

Figure 4.17: Example photoconductivity response of a reference CdTe cell

4.1.9 Photoconductivity Response

A working cadmium telluride cell was used as a reference cell and was run at the start of each day of measurements to ensure the equipment was working correctly. Figure 4.17 shows an example of the response recorded using the CdTe reference cell. The response peaks at 855 nm with a photoconductance of 65 mS W^{-1}. CdTe has a band gap of 1.45 eV [58] which corresponds to light of wavelength 855 nm.

In comparison the photoconductivity curves of the bulk samples heated to 510 °C produced the responses shown in Figure 4.18. No clear response can be seen in any of the graphs and their range is 0 mS W^{-1} to 0.5 mS W^{-1} compared to a minimum of 1 mS W^{-1} to 2 mS W^{-1} and maximum of 65 mS W^{-1} for the reference. In this case it would appear there is no photoconductivity response from any of the samples tested. This could be because there is no response or it may have been masked. It is possible that the lack of response may have been caused by the presence of metallic bismuth seen in previous results. Bismuth conducts electricity independently of illumination so if another material is present that is photoconductive it may have be been electrically shorted by the bismuth and the photoconductivity contribution would not have been recorded. This would be consistent with the results seen and especially in the higher bismuth content samples in Figures 4.18d to 4.18d.

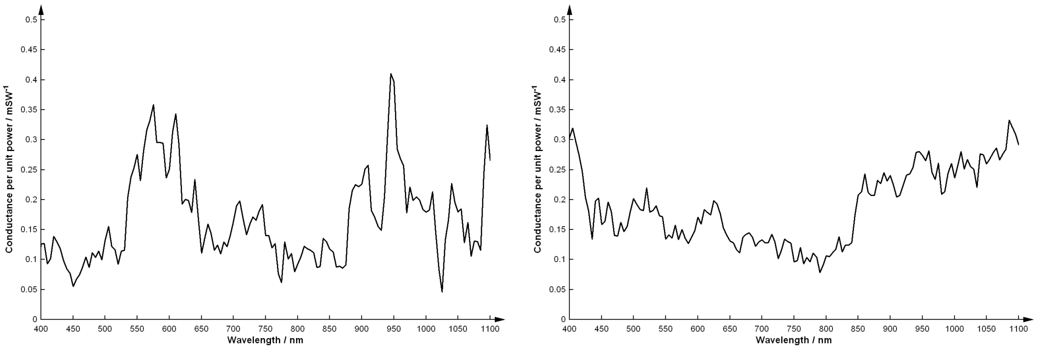

(a) 8 mol % Bi **(b)** 17 mol % Bi

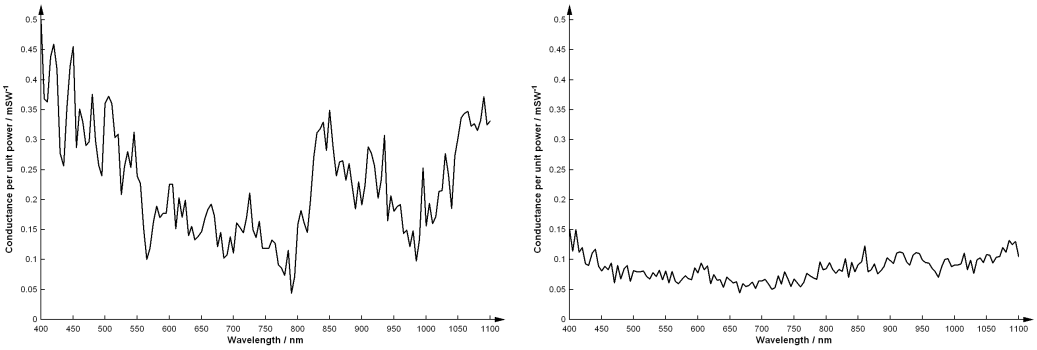

(c) 25 mol % Bi **(d)** 33 mol % Bi

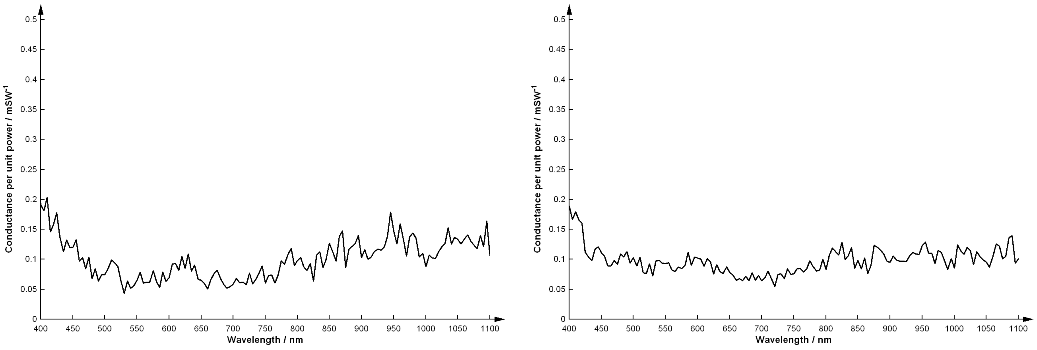

(e) 42 mol % Bi **(f)** 63 mol % Bi

Figure 4.18: Photoconductivity response of bulk samples annealed at 510 °C

4.2 Thin Films by DC Magnetron Sputtering

4.2.1 Position of Sputtering Targets

During co-deposition two targets are directed at the substrate, one from either side and along the long axis. To decide the best position for the targets two geometries were tested. Targets were directed at the centre of the substrate (position 1) and at the edges of the substrate, 37.5 mm from the centre (position 2). In each case the targets where held 10 mm away from the point they were aimed at. Powers were chosen to be 15 W and 80 W for bismuth and copper respectively which should give a Cu/Bi ratio of approximately 3 as derived form the calibration of targets in Section 3.2.2.

Figure 4.19 shows the thickness profiles as measured by a KLA Tencor alphastep profiler from sputtering copper and bismuth individually and together using each position. In general the single material depositions produced thickness gradients that changed in direct proportion to position along the sample with the exception of bismuth in position 1. A predicted thickness for the co-depositions were added to the plots by adding the individual thicknesses. It was predicted position 1 would not give an uniform thickness but position 2 would. The co-deposited layer using position 1 could not be measured due to adhesion problems and position 2 produced a well adhered layer which was thicker in the middle than the ends. Due to adhesion problems associated with position 1, position 2 was used for the remainder of the study.

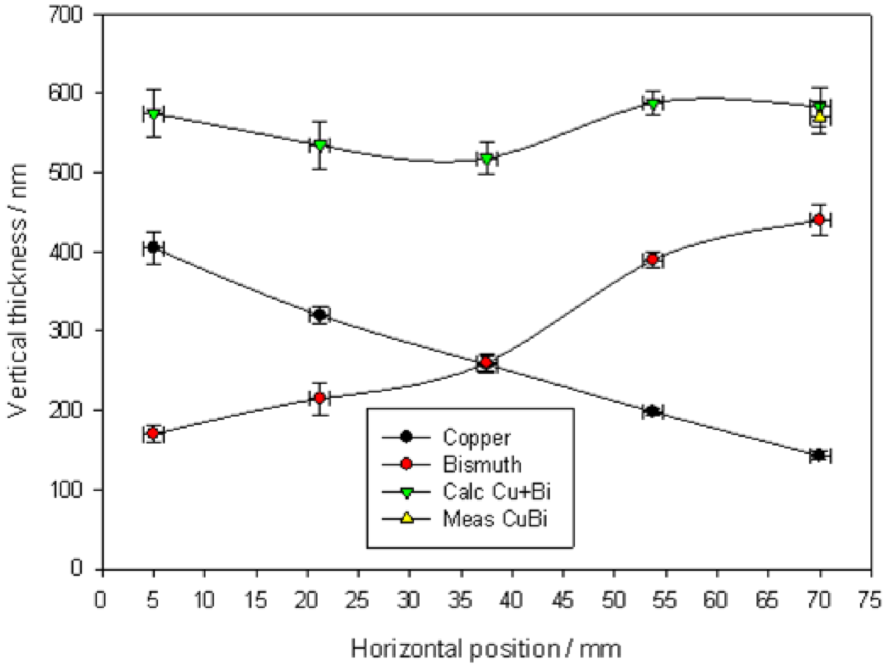

(a) Target sources directed at centre of substrate

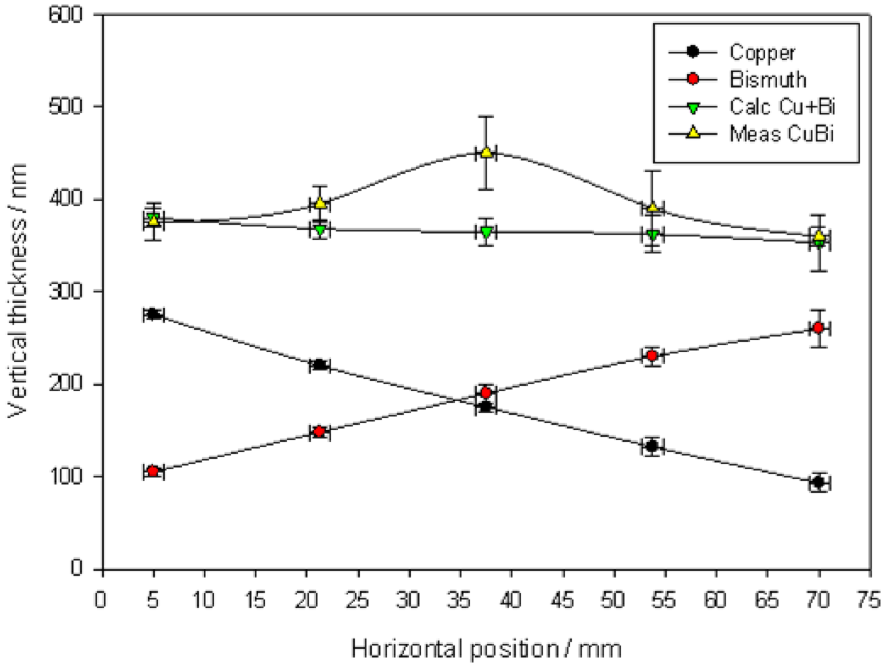

(b) Target sources directed at edge of substrate (37.5 mm from centre)

Figure 4.19: Thickness profile of Cu and Bi libraries as measured by alpha step for two sputtering geometries

4.2.2 Copper Bismuth Sulphide Libraries

Deposition of the Precursors

Three single-slide precursors were prepared by sputtering copper and bismuth onto soda lime glass slides. One slide was created by depositing copper and bismuth simultaneously. Two more slides were deposited by sputtering eight alternate layers of copper and bismuth, one slide for each stacking order. The sputtering configuration was that in Figure 3.4a. The ratio Cu:Bi in Cu_3BiS_3 is three, i.e. 25 % Bi but when deposited using powers derived from single target calibration EDX showed the copper content was higher than expected. To extend the range of composition a further three slides were deposited using target powers calculated to give a Cu:Bi ratio of one. Slide names (which include the calculated Cu:Bi ratios) and sputtering conditions are summarised in Table 4.5.

Sample	Copper Target		Bismuth Target		Order
	Power / W	Time / s	Power / W	Time / s	
CuBi 3:1	183	240	30	240	Simultaneously
Cu-Bi 3:1	183	60	30	58	Cu then Bi, ×4
Bi-Cu 3:1	183	60	30	58	Bi then Cu, ×4
CuBi 1:1	87	240	45	240	Simultaneously
Cu-Bi 1:1	87	60	45	60	Cu then Bi, ×4
Bi-Cu 1:1	87	60	45	60	Bi then Cu, ×4

Table 4.5: Sputtering conditions used to deposit the metallic precursors of the Cu−Bi−S libraries

Visually most of the samples were smooth and reflective, see Figure 4.20. The CuBi co-deposited libraries look like they have a band structure across them. The CuBi 1:1 library has 5 distinct bands across it and SEM images of each band were taken, see Figure 4.21. From the images it can be seen that the first band

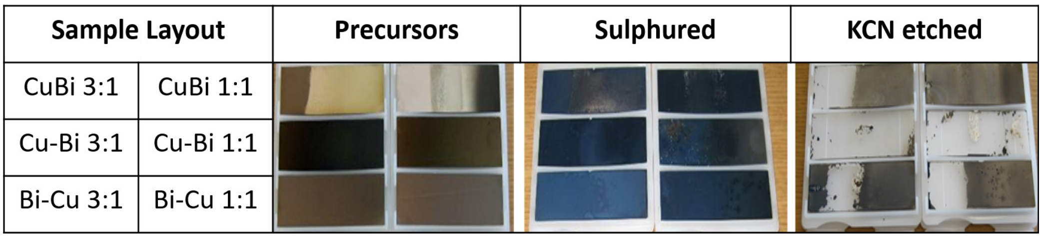

Figure 4.20: Images of the precursor, sulphurised, and etched copper bismuth sulphide libraries

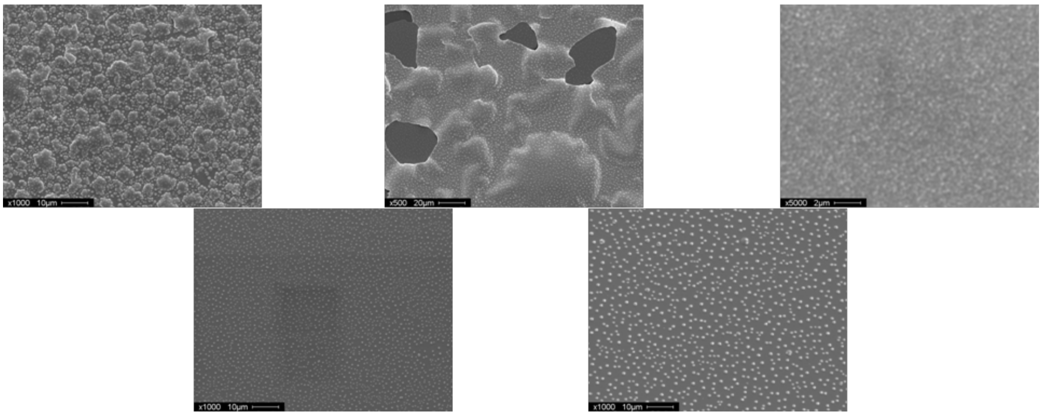

Figure 4.21: SEM images from each band observed on the CuBi 1:1 library, from left to right images taken at points 10 mm, 30 mm, 40 mm, 51 mm and 65 mm from the left edge of the slide and along the middle

in the copper rich region has a structure that looks like the film is buckling, the third image shows much the same but the buckling is much larger and the film has collapsed at various points. The other images look more continuous but have small dots over them. It appears that the band structure observed is more likely due to various levels of adhesion difficulties.

XRD was used to determine what phases were present on the precursors. The Cu−Bi bulk binary alloy phase diagram, see Figure 4.22, can help by suggesting probable phases, although it must be remembered that thin films are neither bulk nor in equilibrium therefore it is useful only as a starting point. The Cu−Bi bulk binary phase diagram shows copper and bismuth are not soluble in each other and

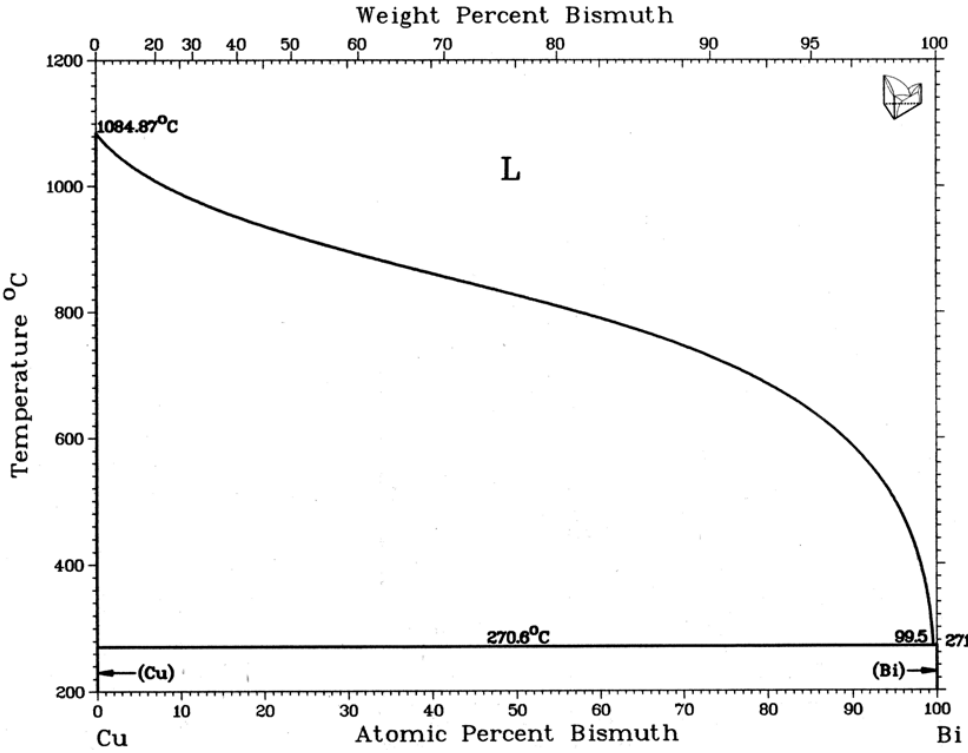

Figure 4.22: Binary alloy phase diagram for the Cu−Bi system [46]

there is a eutectic close to pure Bi (99.5 at % Bi) therefore we would expect no alloying. XRD confirms this by showing only copper and bismuth at all points on the library with no binary phases present.

EDX was carried out on the precursors to map the composition of the deposited film and the results are plotted as contour maps of bismuth concentration in Figure 4.23. It can be seen that there is lateral composition gradient across the libraries, although not as constant across the co-deposited samples. Atomic fraction is plotted, the region of interest would be at 0.25 since this would be the atomic fraction of Bi when the Cu:Bi ratio is 3. Each of the libraries cover this atomic fraction.

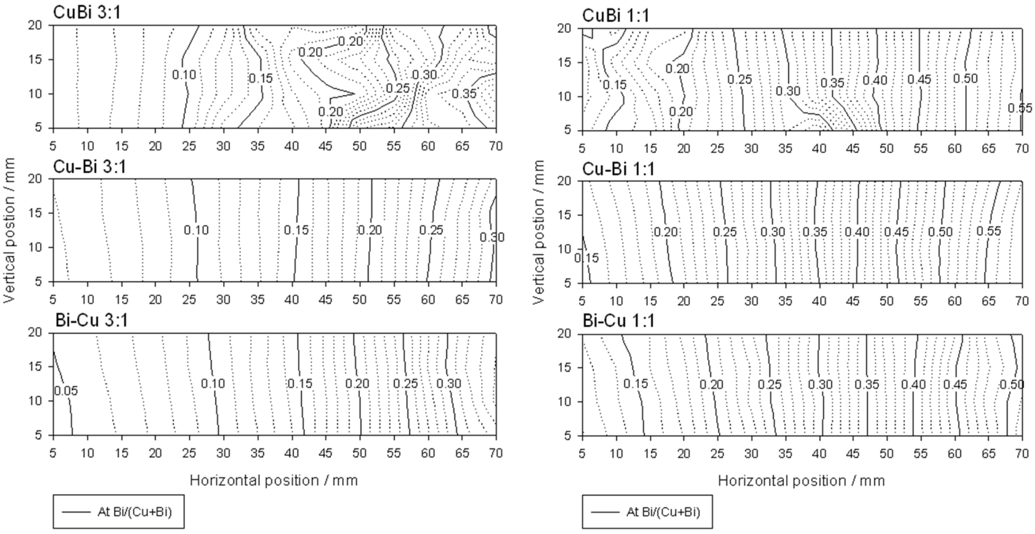

(a) Cu:Bi ratio 3:1 **(b)** Cu:Bi ratio 1:1

Figure 4.23: Composition contour maps showing bismuth content of precursor libraries

Sulphuristion of the Precursors

The precursors each had 1 µm of sulphur deposited on them by thermal evaporation. They were then sealed inside glass ampoules and heated to 260 °C at an average rate of 30 °C min^{-1}. After a dwell time of 30 h they were left to cool naturally to room temperature. The temperature and dwell time were an adaptation from Gerein and Haber [38], where 270 °C is used for 30 h in an H_2S atmosphere. The annealing temperature was reduced to 260 °C to avoid damage to the films since the melting point of bismuth is 271 °C.

As can be seen in Figure 4.20 most of the libraries have taken on a matte dark blue colour with the possible exception of the CuBi 3:1 co-sputtered library, it is a dull grey with dark blue spots and the Bi-Cu 3:1 library which is a slightly lighter shade of blue.

EDX and XRD measurements were taken but for the copper bismuth libraries

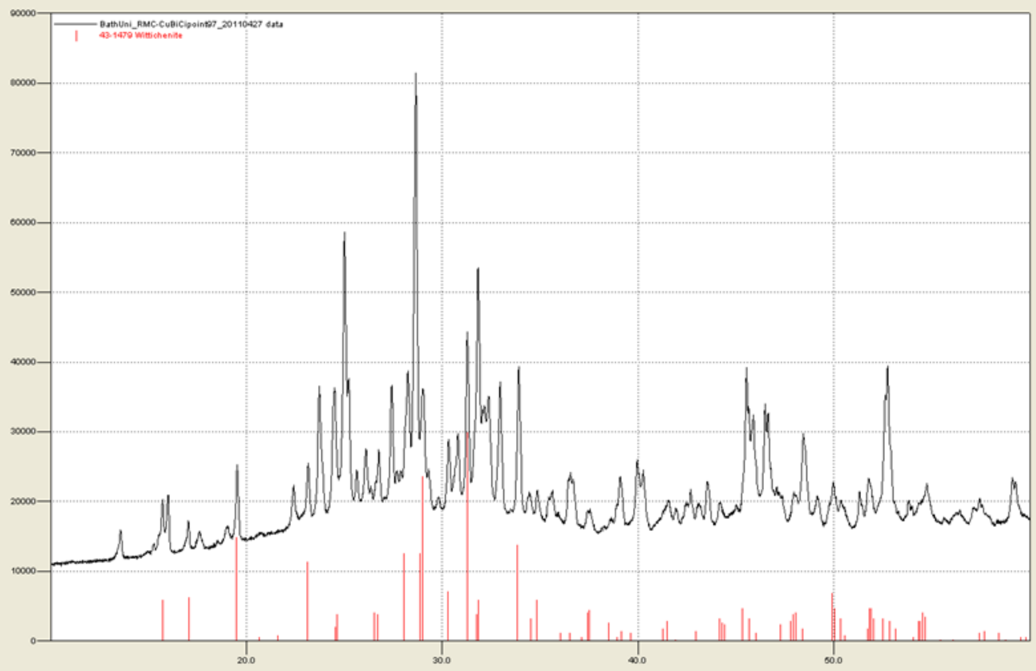

Figure 4.24: Inconclusive diffractogram of a point with coordinates (65,10) on the Cu-Bi 1:1 stacked library with peak data for Cu_3BiS_3 for comparison

the diffractograms were very difficult to interpret and it was not possible to distinguish with certainty between the phases present. On some of the points CuS, Bi_2S_3, and $Cu_4Bi_4S_9$ may have been present. There was no clear indication that Cu_3BiS_3 was present except for a small region on the Cu-Bi 1:1 stacked library. A point central to this region with coordinates in millimetres of (65,10) was chosen to have XRD repeated on it using equipment with a finer 2θ resolution. As can be seen in Figure 4.24 the diffractogram obtained was inconclusive due to the large number of peaks. There are peaks in the locations expected for Cu_3BiS_3 but they are small compared to the others and obscured.

KCN Etching

KCN etching was performed at Bath University. This was to remove the sulphide binary phases which was thought would make identification of any other phases by XRD clearer. The libraries were submerged in 5 % KCN solution for 1 min to etch away any copper sulphide phases. All of the blue colour was removed from the films to reveal smooth reflective grey film on the parts of the libraries where any film was left, see Figure 4.20. Unfortunately, both Cu-Bi stacked libraries were totally destroyed taking with them the region thought most likely to contain Cu_3BiS_3.

4.2.3 Double Anneal

Annealing at 260 °C failed to produce Cu_3BiS_3 on the copper bismuth sulphide libraries. If it did form, it was hidden behind many other phases which made XRD too complicated to analyse. Cu_3BiS_3 may have failed to developed due to the low temperature of annealing which was specifically chosen to avoid the melting of bismuth. Since Bi_2S_3 has a higher melting point of 1036 K [59] (763 °C). It was thought the library might survive annealing at a higher temperature if the bismuth was fully converted to Bi_2S_3 first and thus avoid melting at higher temperatures and compromising the film as suggested in Colombara et al. [44].

To investigate this two precursors of approximately 500 nm thick were prepared by sputtering eight alternate layers of bismuth and copper onto soda lime glass. The sputtering configuration was that in Figure 3.4b and microscope slides cut in half lengthways were used as substrates. Both samples were deposited at the same time. Then 1 µm of sulphur was evaporated onto each sample and both were annealed at 250 °C for 30 min and allowed to cool naturally outside of the furnace. This was to allow all the bismuth convert into Bi_2S_3.

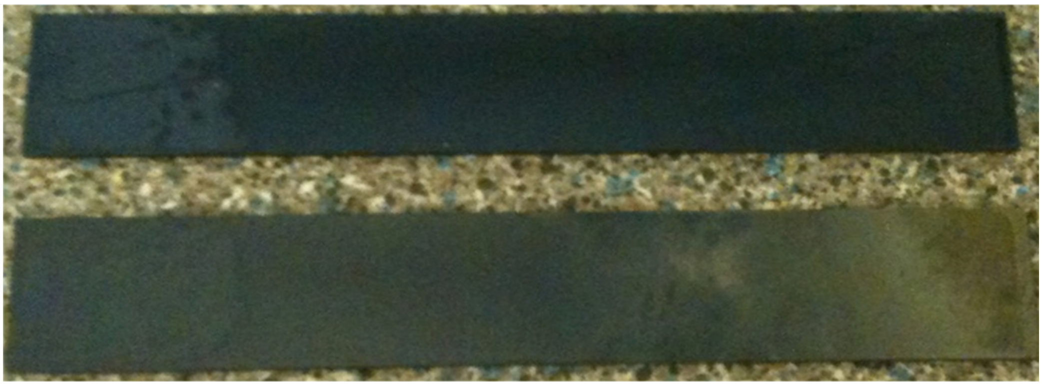

Figure 4.25: Images of the single annealed (top) and double annealed (bottom) samples

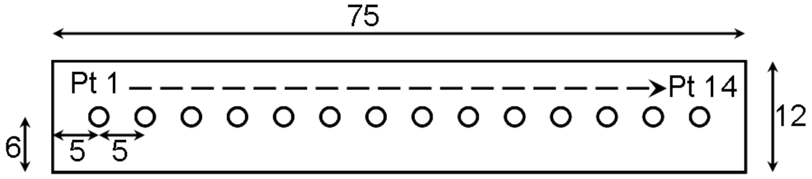

Figure 4.26: Position of sample points 1 to 14 on the half slide size samples

Another 1 µm of sulphur was evaporated onto one of the samples which then underwent a second anneal at 500 °C for 30 min and allowed to cool naturally. An image of the final samples can be seen in Figure 4.25. Although not visible in the image the right most 10 mm of the double annealed sample appears to be slightly translucent. Figure 4.26 shows the location of the sampling points on each sample.

SEM was used to take images of the surface of the double annealed library and are shown in Figure 4.27. They look like a film covered with fragments of another phase, most likely sulphur. There are fewer fragments and more film exposed on the image at the bismuth rich end of the sample.

EDX showed that both precursors had very similar compositional range, see Figure 4.28a. The precursor to be annealed once had a range of Cu/Bi ratios from 25.01 on the left most point (point 1) to 3.76 on the right most point (point 14). The precursor to be annealed twice had a range of Cu/Bi ratios from 26.84 on point

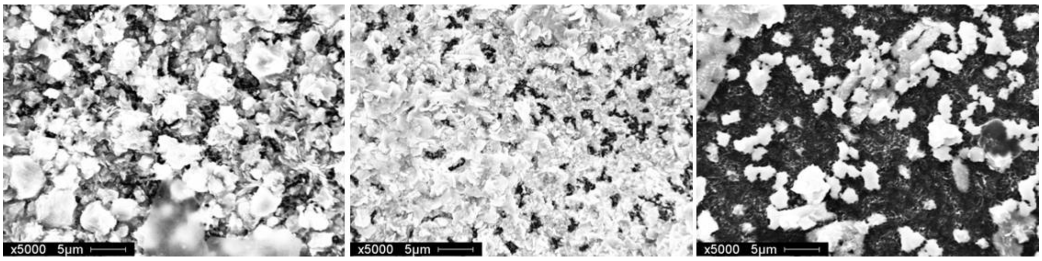

Figure 4.27: SEM images of double annealed library, Point 1, the middle and point 14

1 to 4.00 on point 14. The precursors were more rich in copper than desired for Cu_3BiS_3, the ideal Cu/Bi atomic ratio for this phase based on the chemical formula would be 3. The precursors appeared to adhere well and were very reflective. Once the annealing had taken place the Cu/Bi ratio was plotted again in Figure 4.28b and the S/metal ratio was plotted in Figure 4.28c. The Cu/Bi ratio for the single annealed sample increased slightly at each point with a much larger increase at point 1. The double annealed sample doesn't show such an increase, the Cu/Bi ratio is less stable and some points decreased suggesting either no depletion of bismuth in the first anneal and/or a depletion of copper that compensates.

XRD was preformed on both samples and the phases identified are summarised in Table 4.6. Example spectra and peak data for the phases identified are displayed in Figure 4.29. CuS was found throughout the single annealed sample with strongest peaks at point 1, the copper rich end, and decreasing at points closer to the bismuth rich end of the sample. Bi_2S_3 was identified at point 3 and its XRD peaks grew stronger with increasing bismuth content. This shows that annealing at 250 °C for 30 min is adequate to convert all copper and bismuth into their sulphides. On the double annealed sample CuS was also observed decreasing from point 1 to point 9. Another ternary phase was observed at points 6 to 10 which may have been either $Cu_{1.77}Bi_{4.57}S_8$ or $CuBi_5S_8$ but their peak data are almost identical so

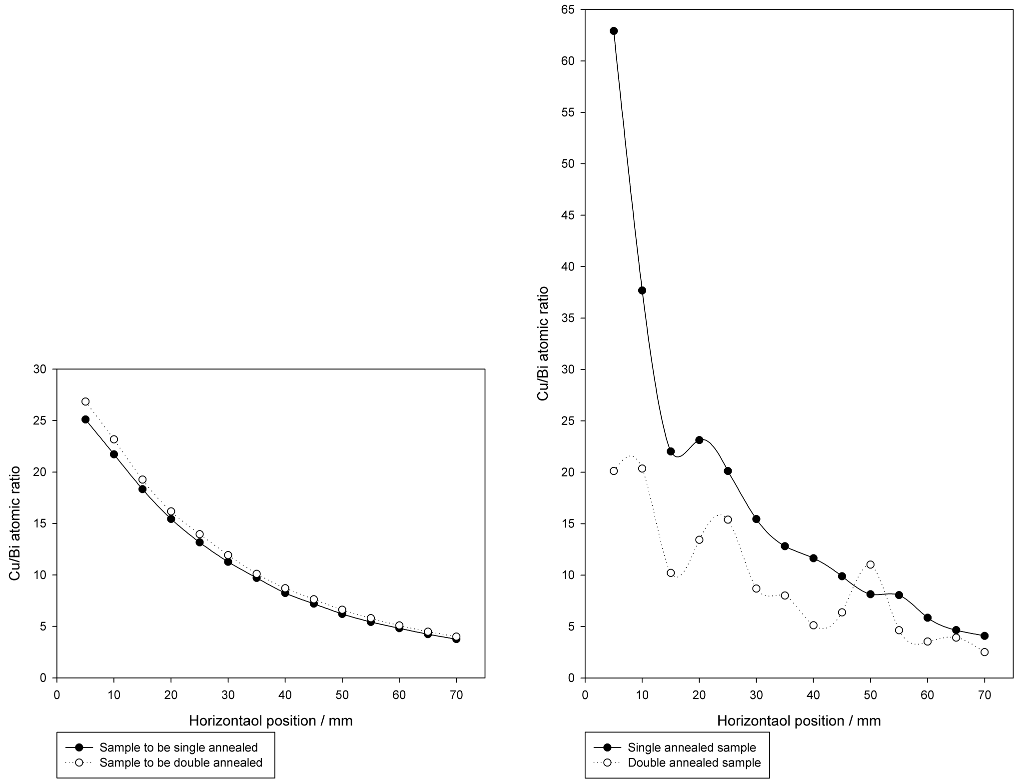

(a) Cu/Bi atomic ratio across precursors to be single and double annealed

(b) Cu/Bi atomic ratio across single and double annealed samples

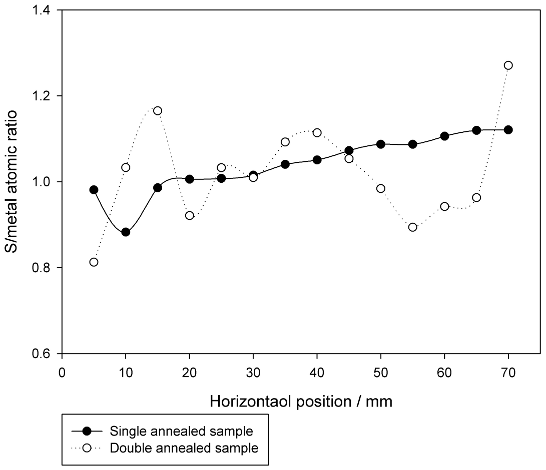

(c) S/metal atomic ratio across single and double annealed samples

Figure 4.28: Composition across single and double annealed samples

Point	Single annealed sample		Double annealed sample		
1	CuS		CuS		
2	CuS		CuS		
3	CuS	Bi_2S_3	CuS		
4	CuS	Bi_2S_3	CuS		
5	CuS	Bi_2S_3	CuS		
6	CuS	Bi_2S_3	CuS	$CuBi_5S_8$	
7	CuS	Bi_2S_3	CuS	$CuBi_5S_8$	
8	CuS	Bi_2S_3	CuS	$CuBi_5S_8$	
9	CuS	Bi_2S_3	CuS	$CuBi_5S_8$	
10	CuS	Bi_2S_3		$CuBi_5S_8$	Cu_3BiS_3
11	CuS	Bi_2S_3		$CuBi_5S_8$	Cu_3BiS_3
12	CuS	Bi_2S_3			Cu_3BiS_3
13	CuS	Bi_2S_3			Cu_3BiS_3
14	CuS	Bi_2S_3			Cu_3BiS_3

Table 4.6: Phases identified by XRD at each sample point on the single and double annealed libraries

it was not possible to distinguish between them. Lastly, Cu_3BiS_3 was observed increasing from point 10 to point 14. This is the region that appeared to be slightly translucent. It can be seen that Cu_3BiS_3 only forms at the bismuth rich end of the sample but the sample was copper rich. The film was translucent and not suitable for testing with photoconductivity as a solid continuous film is required. A thicker film would be ideal, with some adjustments to precursor composition or annealing conditions this could be a way to grow films of Cu_3BiS_3.

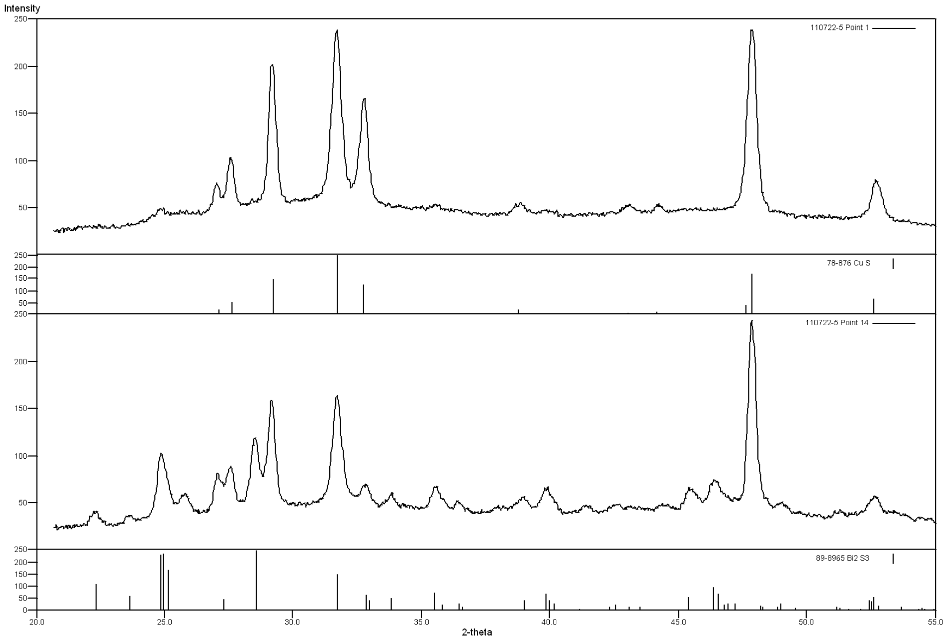

(a) XRD spectra of point 1 and 14 of the single annealed sample

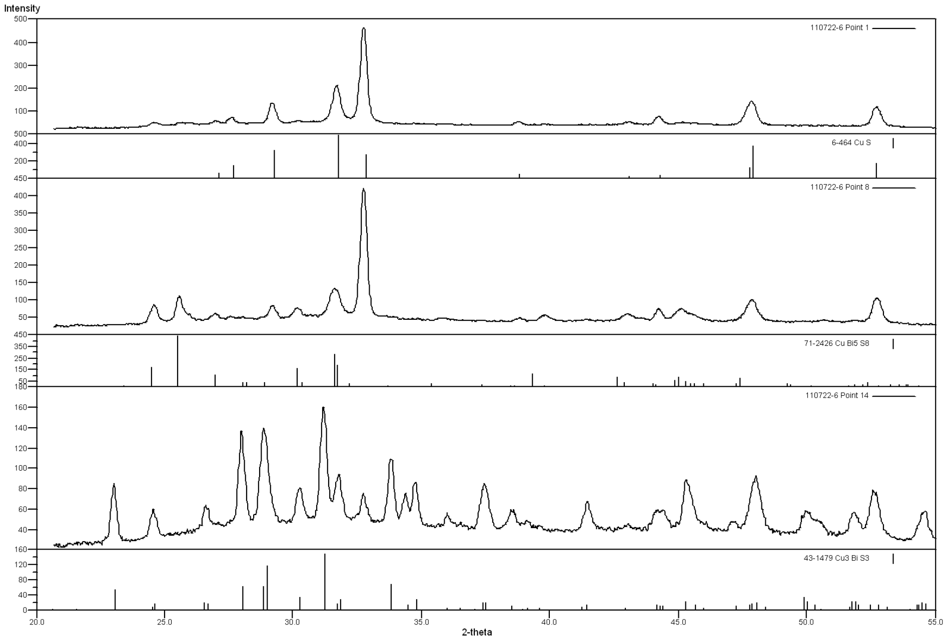

(b) XRD spectra of point 1, 8 and 14 of the double annealed sample

Figure 4.29: XRD spectra of various points on the single and double annealed samples with peak data for the phases identified

Sample	First stage of anneal	Second stage of anneal
1	250 °C for 30 min	N/A - sample removed after first stage
2	250 °C for 30 min	500 °C for 5 min
3	250 °C for 30 min	500 °C for 30 min

Table 4.7: Summary of annealing conditions for two stage anneal with sulphur pellet

4.2.4 Two Stage Anneal with Sulphur Pellet

Another sulphurisation technique was attempted. Rather than evaporate a layer of sulphur directly onto the film a 0.01 g fragment of a sulphur pellet was placed in the ampoule alongside the metallic precursor. During annealing the pellet melted and provided a sulphur atmosphere. The anneal was allowed to continue to 500 °C after a dwell time of 30 min at 250 °C. It was thought this two stage anneal could successfully mimic the double anneal in the previous section that produced a film with Cu_3BiS_3. Three single composition samples were prepared by a co-sputter of bismuth at 17 W and copper at 75 W. The substrate was rotated during sputtering to ensure an even distribution of copper and bismuth targeted at Cu/Bi=3. The middle slide had been previously cut into 6 to provide 6 small precursors. Three of the precursors were annealed with the conditions listed in Table 4.7

Photographs of the annealed samples can be seen in Figure 4.30. Sample 1 came out a solid very dark blue and Sample 2 was a solid slightly translucent lighter grey. Sample 3 was very unusual, it produced a swirly pattern of opaque grey film. Unlike the first two samples sample 3 was not continuous, there were gaps between the swirls where the glass substrate could be seen from underneath.

SEM images were taken of the surfaces of the samples and are shown in Figure 4.31. EDX point analysis was performed to find the composition of each of the features seen in the SEM images. Sample 1 appeared to have a rough surface

(a) Sample 1 - a single anneal of 30 min at 250 °C produced a solid dark blue film

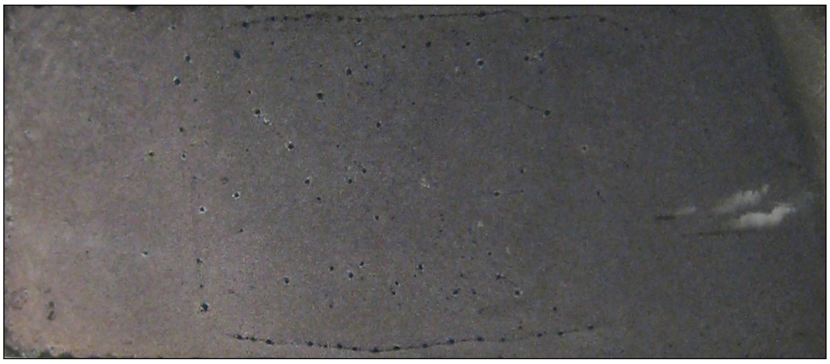

(b) Sample 2 - a double anneal of 30 min at 250 °C then 5 min at 500 °C produced a solid slightly translucent lighter grey film

(c) Sample 3 - a double anneal of 30 min at 250 °C then 30 min at 500 °C produced a swirly pattern of opaque grey film with many gaps between the swirls

Figure 4.30: Photographs of double annealed samples showing the results of various secondary annealing conditions

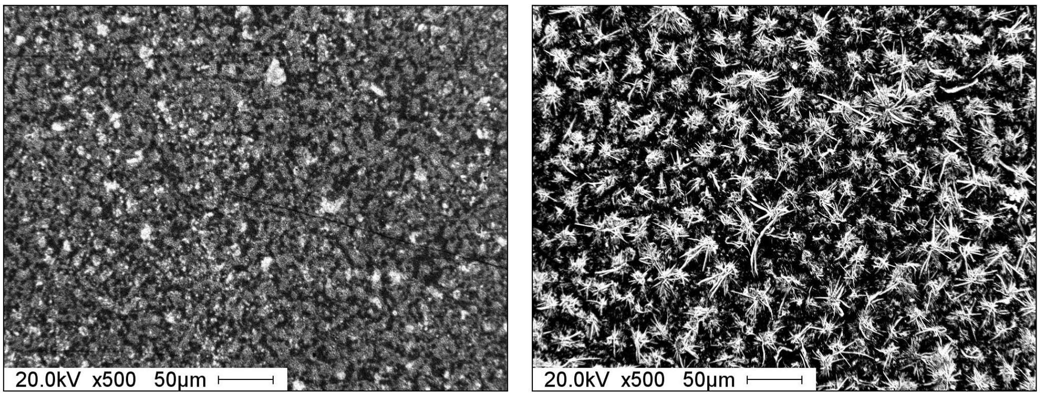

(a) Sample 1 - 30 min at 250 °C

(b) Sample 2 - 30 min at 250 °C and 5 min at 500 °C

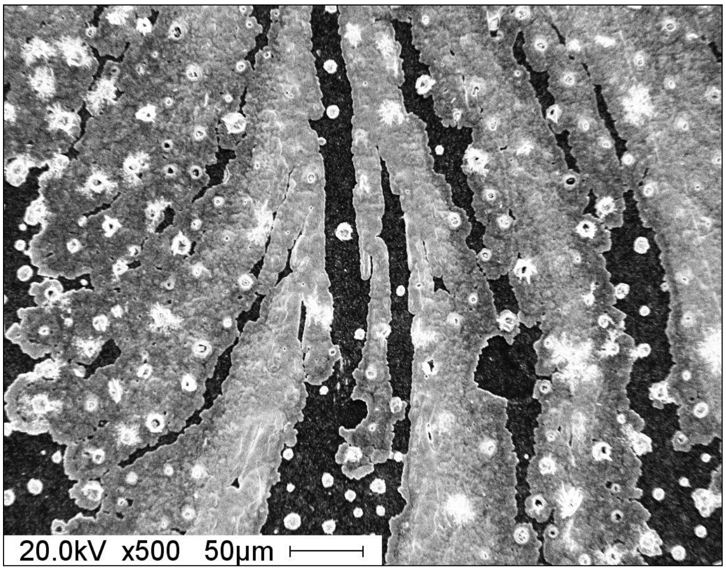

(c) Sample 3 - 30 min at 250 °C and 30 min at 500 °C

Figure 4.31: SEM images of double annealed samples 500 magnification

and had a very variable Cu/Bi ratio across it, the average S/metal ratio was 0.88. The XRD diffraction pattern shown in Figure 4.32 shows the presence of CuS and Bi_2S_3 but no metallic copper or bismuth. This shows that annealing at 250 °C for 30 min using this method also converts all of the precursor materials into their sulphides. Sample 2 was annealed in the same way as sample one and then heated to 500 °C and held there for 5 min. The SEM image is a dark layer with light coloured spiky dots. EDX of the light areas areas have an average Cu/Bi of 5.97 and S/metal of 0.97, the dark areas had values of 1.22 and 0.84 respectively. Three phases were identified using XRD, $Cu_3Bi_3S_7$, $Cu_4Bi_4S_9$ and CuS. See Figure 4.33. Sample 3 was held at 500 °C for 5 min in the second stage of the anneal. The swirling pattern can be clearly seen as a feathered pattern in the SEM image. In addition to the pattern there is a dark back ground and light coloured spots covering the whole image. Spot EDX analysis was performed on each area. The black background gave a Cu, Bi or S content of <1 % indicating that there is no film there and it is the glass slide underneath being imaged. The white spots had a Cu/S ratio of 1.07 indicating that they could be CuS. The grey area had an average Cu/Bi ratio of 2.35 and S/metal ratio of 0.67. These ratios are very close to those in Cu_3BiS_3, they would give a slightly bismuth rich version of $Cu_{2.35}BiS_{2.24}$. XRD confirmed the presence of Cu_3BiS_3 on the third sample. See Figure 4.34.

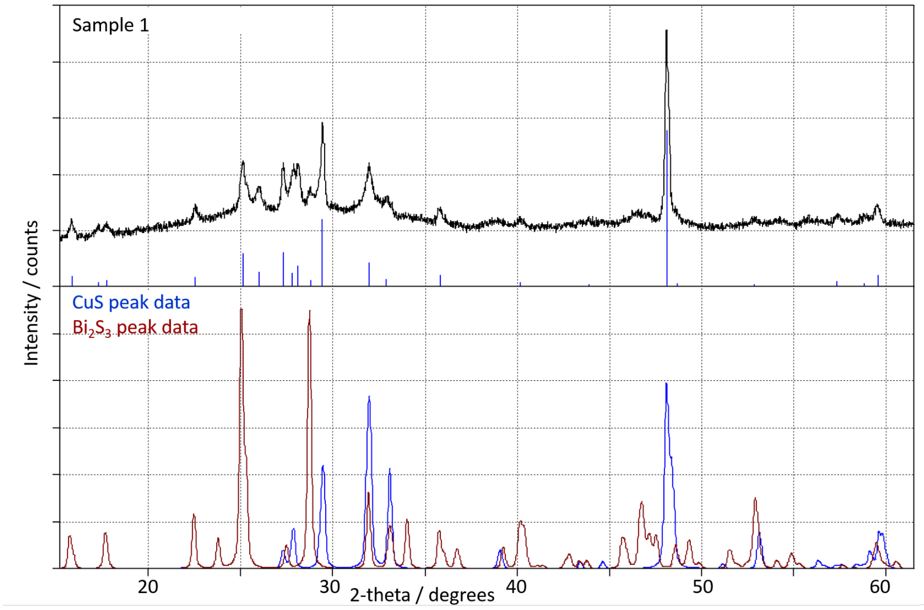

Figure 4.32: XRD of Sample 1 in two stage anneal - 30 min at 250 °C, only CuS and Bi_2S_3 identified

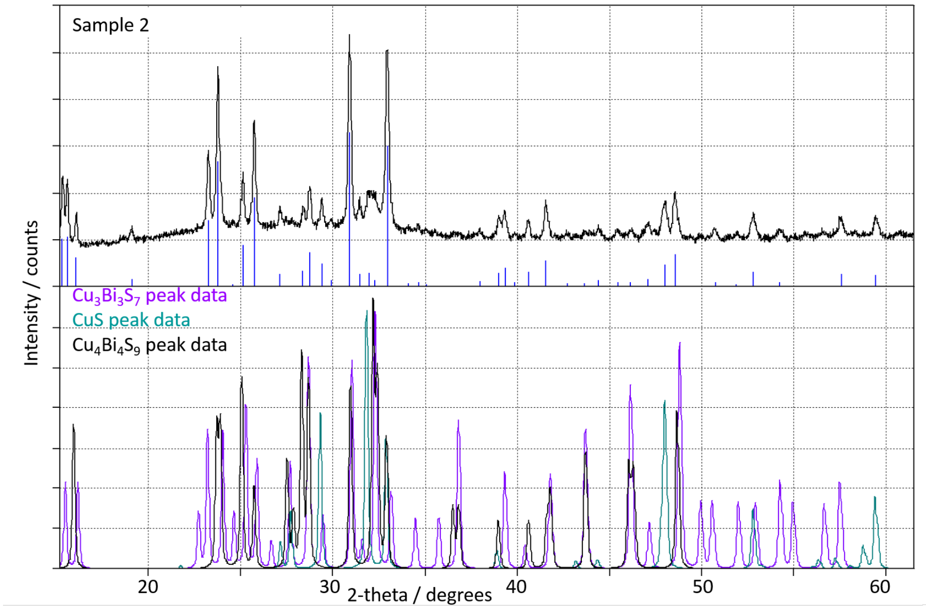

Figure 4.33: XRD of Sample 2 in two stage anneal - 30 min at 250 °C then 5 min at 500 °C, $Cu_3Bi_3S_7$, $Cu_4Bi_4S_9$ and CuS identified

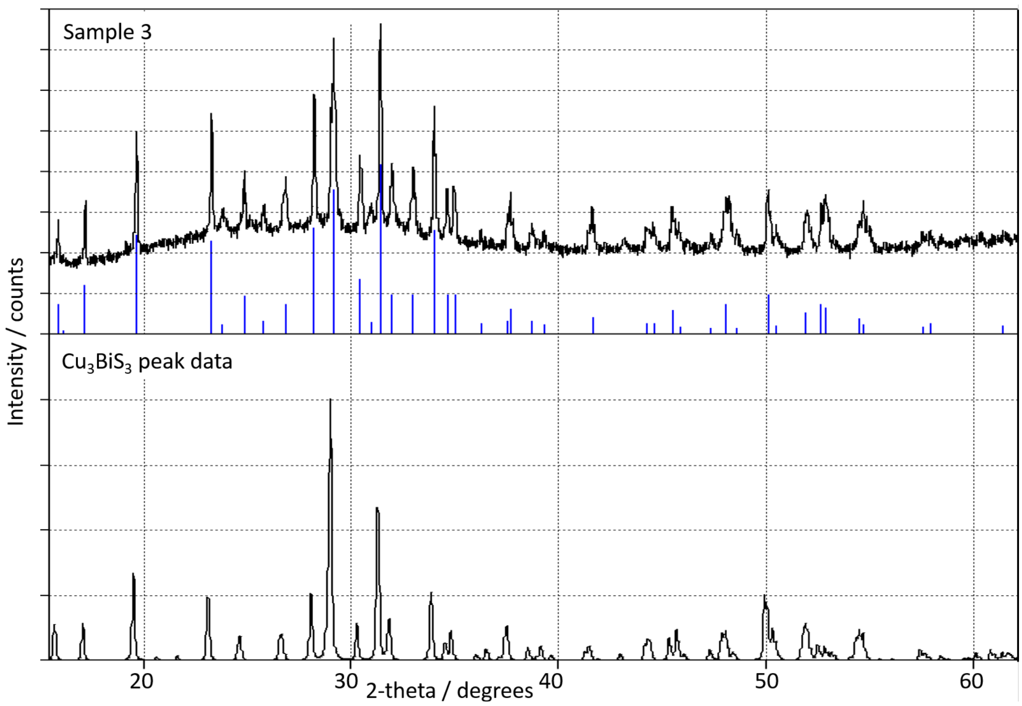

Figure 4.34: XRD of Sample 3 in two stage anneal - 30 min at 250 °C then 30 min at 500 °C, Cu_3BiS_3 confirmed

4.3 Thin Films by Thermal Evaporation

This section contains the results of evaporating copper sulphide and bismuth. CuS and Bi were evaporated individually and then evaporated together in an attempt to produce films of Cu_3BiS_3.

4.3.1 Evaporation of Starting Materials

Before attempting an evaporation of copper sulphide and bismuth together trial runs evaporating the individual materials were carried out to see how each behaved in isolation. The aim was to find an approximate starting point for the currents required to achieve the desired proportions of copper, sulphur and bismuth.

From the phase diagram there is a narrow single phase region of Cu_3BiS_3 at 25 mol % Bi. Therefore, a molecular ratio of 3:1 of CuS and Bi is desirable for the formation of Cu_3BiS_3. The quartz crystal monitor in the evaporation chamber measures rate of deposition and thickness. For a given area the thickness of a film is directly proportional to the volume and so the molar volume can be used as a conversion factor between molecular number and thickness. The calculated molar volume (molar mass divided by mass density) of copper sulphide is 20.09 $\mathrm{cm^3\,mol^{-1}}$. The molar volume of bismuth was found to be 21.31 $\mathrm{cm^3\,mol^{-1}}$ [51]. The molecular ratio of 3 to 1 can now be expressed as a thickness ratio of 60.27 to 21.31 which is 2.83:1. A CuS deposition rate 3 times greater than that for Bi was decided to be a sensible starting point.

Copper Sulphide

Copper sulphide was evaporated onto a glass slide and a baffle was used to achieve a thickness gradient across the sample. The rate at which it was deposited was measured using a quartz crystal monitor located to the side of the mid point of the sample and EDX was used to measure the deposited composition across each sample. This is important because a ratio of copper and sulphur at unity is required to maintain stoichiometry with Cu_3BiS_3. Figure 4.35 shows the ratio of copper and sulphur deposited across six samples.

Samples CuS0 to CuS2 were deposited with the shutter open from the start of each evaporation. A quartz crucible was used for CuS0 and an alumina crucible was used for CuS1 and CuS2. The crucible was changed due to a very slow deposition rate even at the maximum current possible. Figure 4.35a shows that using a quartz crucible resulted in a film that was sulphur rich. The other two samples returned films that were copper rich. Samples CuS3 to CuS5 were deposited with the shutter closed until the desired current was reached and then the shutter was opened. An alumina crucible was used and was topped up with CuS between each evaporation. The crucible had to be replaced for CuS5 since it cracked in the previous evaporation. Figure 4.35b shows that the copper and sulphur ratio for these samples are much closer to unity than the previous samples. They are still slightly copper rich for the majority of the length of the samples but less so than when the shutter was open from the start of the evaporation.

Using the shutter means that that sample is protected from any deposit that comes from the de-gassing as the material is being heated. This de-gassing can be seen clearly during the deposition of CuS1, shown in Figure 4.36. In this case it

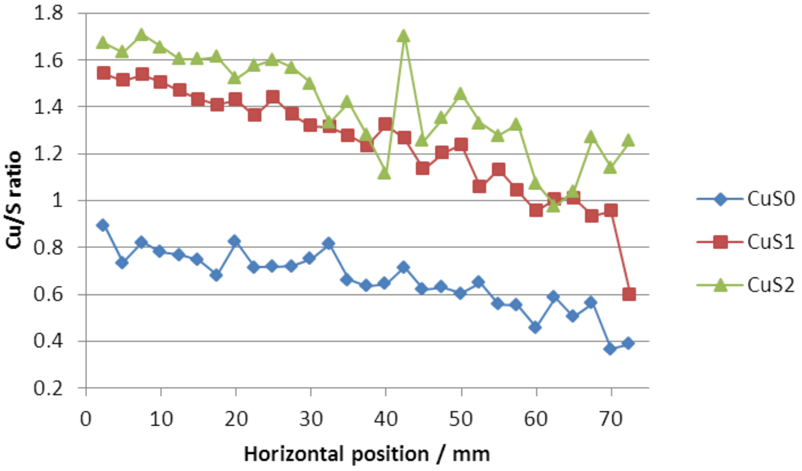

(a) Samples without using the shutter

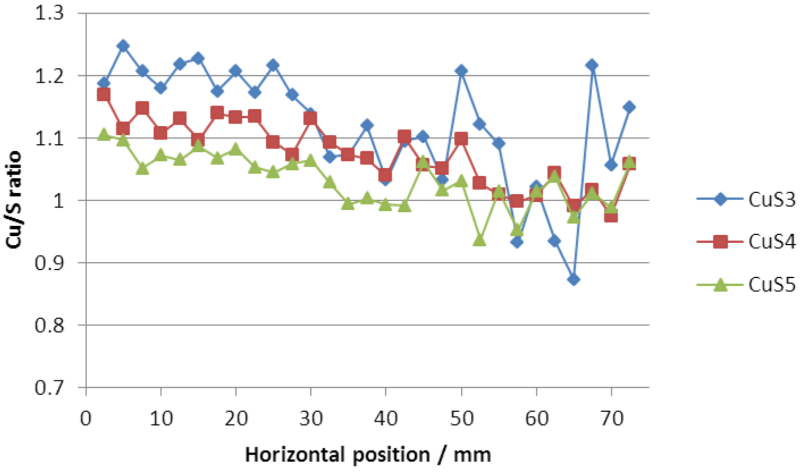

(b) Samples using the shutter

Figure 4.35: Copper and sulphur ratios of evaporated CuS

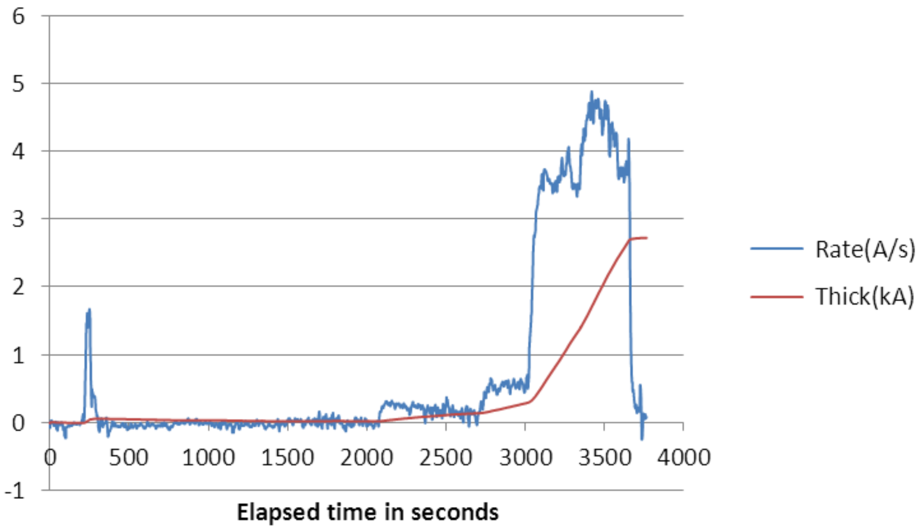

Figure 4.36: Estimated thickness and rate of deposition at centre of sample CuS1

occurs at about 250 s and can be seen by the peak in rate of deposition measured by the quartz crystal monitor. The degassing occurs when a current of 40 A is applied to the heating coil. The CuS doesn't appear to evaporate until much later when the current is nearly at maximum for the equipment.

The rates of deposition and thickness are estimates and are measured close to the midpoint of each sample. With the baffle present there ought to be a thickness gradient across each sample. Figure 4.37 shows an image of the samples and observation would suggest there is indeed a thickness gradient. The samples appear opaque at the end closest to the CuS source and slightly translucent at the opposite end.

From Figure 4.36 it can also be seen that the maximum rate of deposition at the centre for CuS is in the order of $4\,\text{Å}\,\text{s}^{-1}$. Tungsten boats were also tested to see if they would deposit faster, although this time without the baffle. Figure 4.38 shows the deposition of CuS from a tungsten boat. The current was increased slowly to

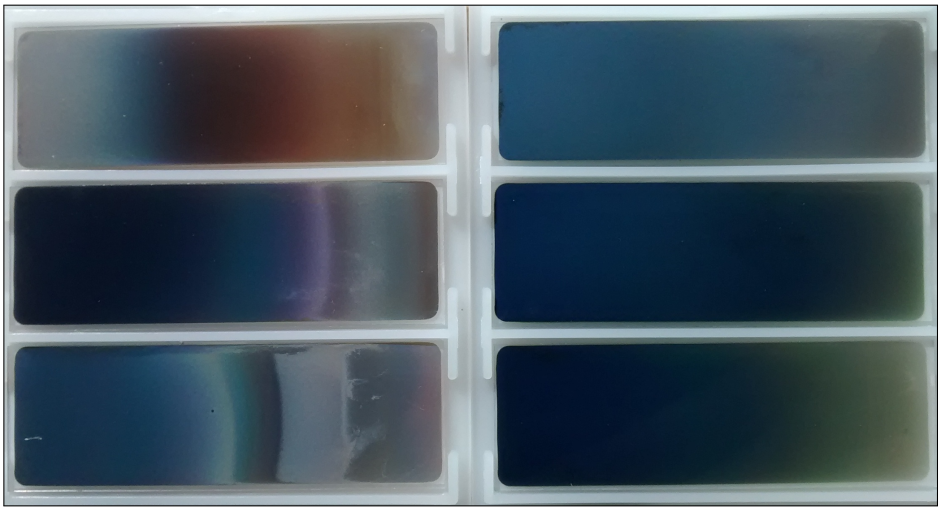

Figure 4.37: Image of samples CuS0–CuS2 on the left and CuS3–CuS5 on the right

prevent de-gassing from knocking CuS out of the boat which is more shallow than a crucible. At 200 s there is de-gassing as before and at the maximum current of 113 A the rate of deposition is between 6 Å s^{-1} and 7 Å s^{-1}. After 800 s there is a sharp decrease in the rate of deposition despite the current not being reduced. This is the point at which the CuS source is exhausted.

This sections shows that copper sulphide can be deposited using evaporation and maintain a ratio of copper and sulphur fairly close to one. It also shows that from tungsten boats copper sulphide can be deposited at between 6 Å s^{-1} and 7 Å s^{-1} when a current of 113 A is applied.

Bismuth

Bismuth was evaporated from an alumina crucible without using a baffle and the rate of deposition was observed using a quartz crystal monitor. The rates of deposition over time can seen in Figure 4.39. The deposition rate appears to roughly double with every 2 A applied after deposition starts at 38 A. Since this

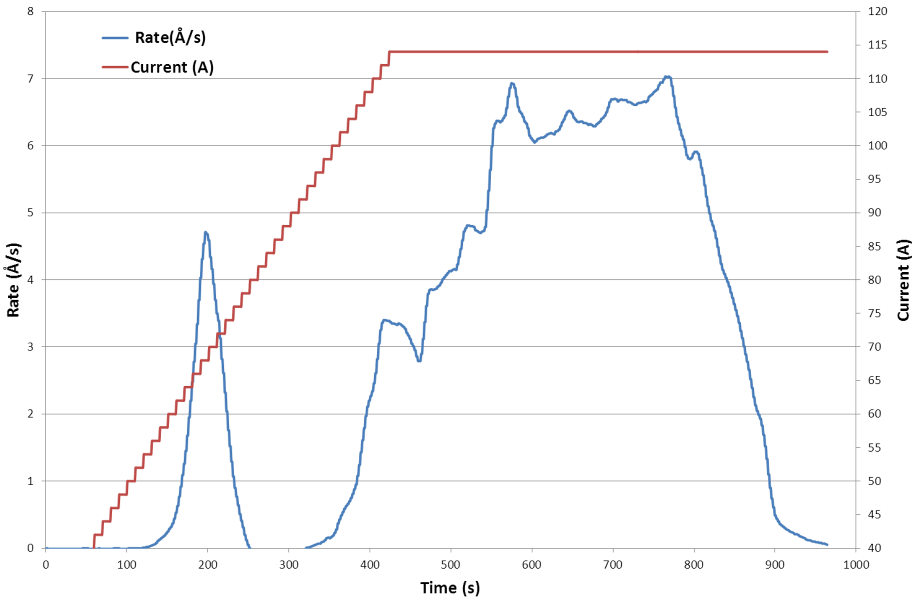

Figure 4.38: Depostion rate of CuS from a tungsten boat

is going to be matched to a copper sulphide rate of 6 Å s^{-1} to 7 Å s^{-1}, a rate of deposition of bismuth of about 2 Å s^{-1} would be desired. Although it is difficult to reach a steady deposition rate 43.5 A was chosen as it appeared to give a rate of around 2 Å s^{-1} when using an alumina crucible.

4.3.2 Co-evaporation of Copper Sulphide and Bismuth

From the findings in the previous sections the following recipe was used to evaporate copper sulphide and bismuth together.

Copper sulphide was evaporated from a tungsten boat which was filled to capacity with 0.3 g of CuS. The current through the boat was raised to 20 A in the first minute then raised by 2 A every 10 s to 113 A which took about 8 min. The current was held at 113 A for 1 min and then the shutter was opened. This was found to give a deposition rate of approximately 6 Å s^{-1}. At the same time

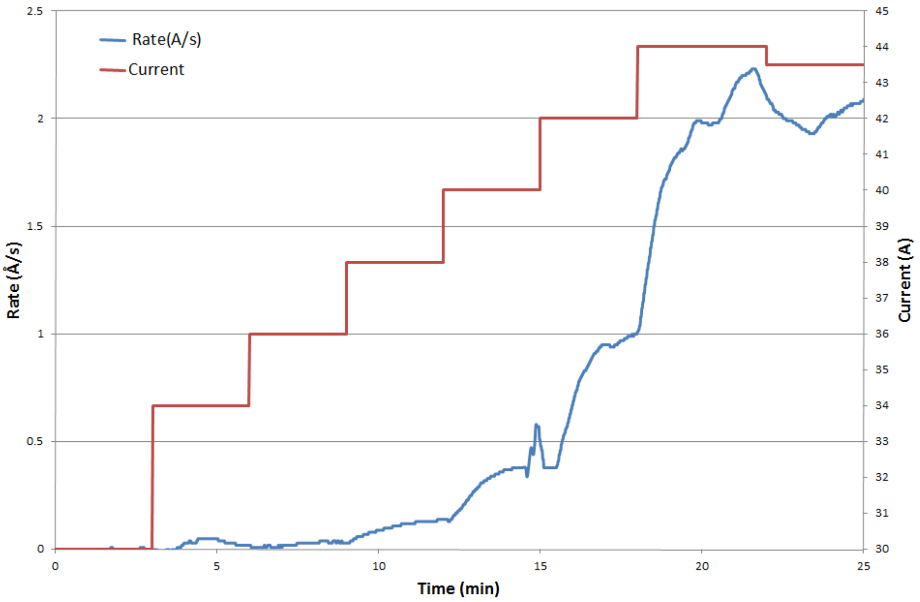

Figure 4.39: Deposition rate of bismuth from an alumina crucible

Bismuth was evaporated from an alumina crucible which was topped up to 2 g of bismuth (4.24 g including the crucible) between each evaporation. A current was applied and slowly raised to 43.5 A. The aim was to reach this target current about a minute before opening the shutter. This was previously found to give a deposition rate of approximately 2 Å s^{-1}. The shutter was kept open until the CuS source was exhausted which was identified by a drop in the deposition rate.

In order to use the quartz crystal monitor to estimate rate of deposition and thickness of the film, density and z-factor of the starting materials had to be estimated. Values for bismuth and copper sulphide are tabulated in the equipment's documentation so by assuming a linear dependence and a ratio of CuS to Bi of 3:1 a weighted mean was taken for each value. The thickness measurement is an estimate for comparison only.

Samples without the Baffle

Three samples, sample 1, 2 and 3, were made to see if co-evaporation would work. The substrate was heated to 200 °C to help encourage a reaction between the constituent materials. The thickness of the samples as measured by the quartz crystal monitor were 611 nm, 525 nm and 427 nm for samples 1, 2 and 3 respectively.

EDX was used to measure the elemental composition of the films deposited and the ratios of Cu/Bi, S/metal, and Cu/S are shown in Figure 4.40. For Cu_3BiS_3 the ideal values for these ratios would be 3, 0.75 and 1 respectively. The samples were fairly consistent, Cu/Bi ratio was low and usually between 1 and 2, the S/metal ratio was low at approximately 0.25 and Cu/S ratio was high at approximately 2 or slightly above.

SEM was used to take an image from the centre of each sample and is shown in Figure 4.41. Each of the samples appear to have a rough surface at ×10 000 magnification. This would help explain why the films appear matte as can be seen in Figure 4.42a. They are all very dark but sample 1 has a blue hue to it and samples 2 and 3 have a slightly more brown hue to them.

XRD was performed across the samples to identify any phases present. Fourteen points 5 mm apart were taken across the middle of the samples and the findings summarised in Table 4.8. In all three samples a bismuth phase could be clearly seen throughout each sample. On sample 2 there are other peaks present but it was difficult to determine which copper sulphide phase they belonged to. Cu_2S seemed most likely but it was inconclusive.

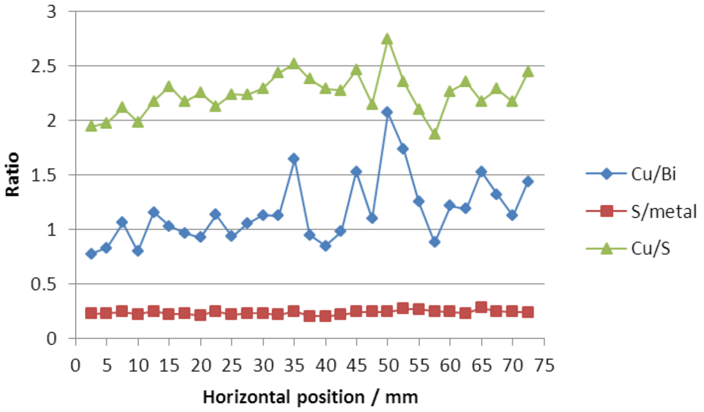

(a) Sample 1

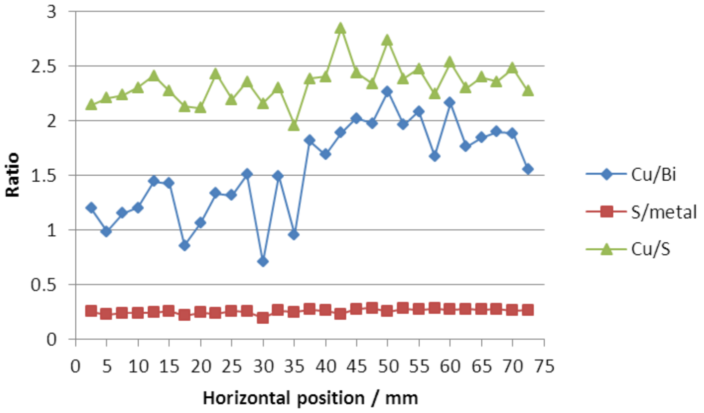

(b) Sample 2

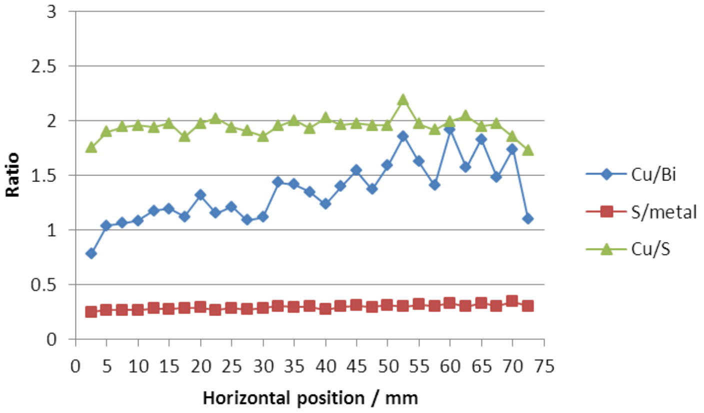

(c) Sample 3

Figure 4.40: SEM Ratios of constituent elements of samples evaporated without a baffle

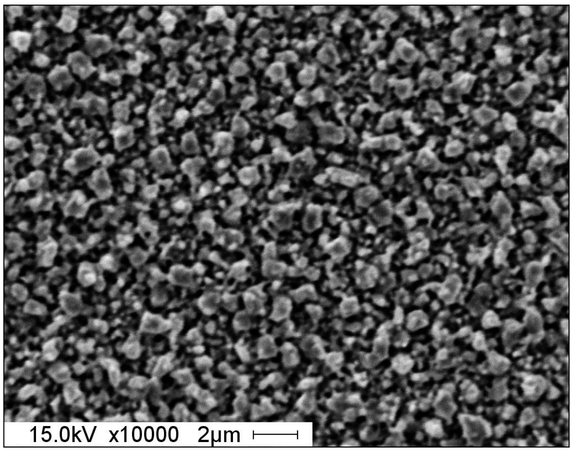

(a) Sample 1

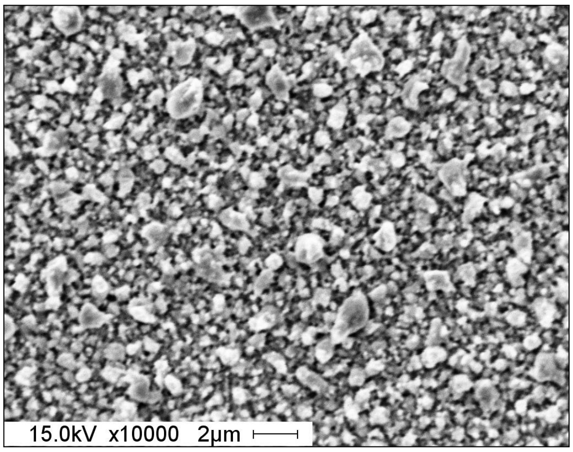

(b) Sample 2

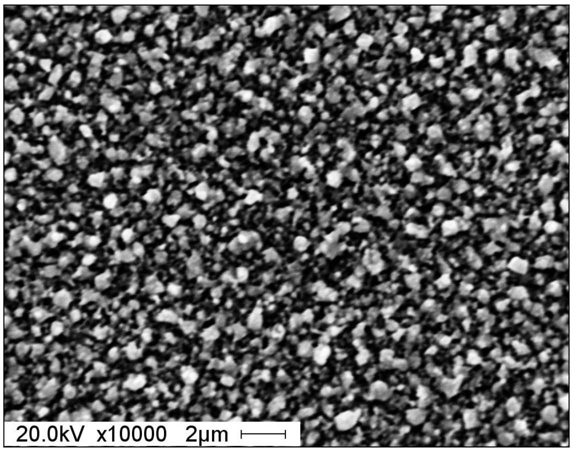

(c) Sample 3

Figure 4.41: SEM images of middle of samples evaporated without a baffle

Sample	Points	Bi	Cu_2S	Notes
1	all	Yes		Peaks decrease towards CuS end
2	1 to 7	Yes		
	8	Yes	Possibly	
	9	Yes	Possibly	Low signal, high background
	10	Yes	Possibly	Mid signal, high background
	11 to 14	Yes		
3	all	Yes		

Table 4.8: Summary of XRD on co-evaporated samples without a baffle

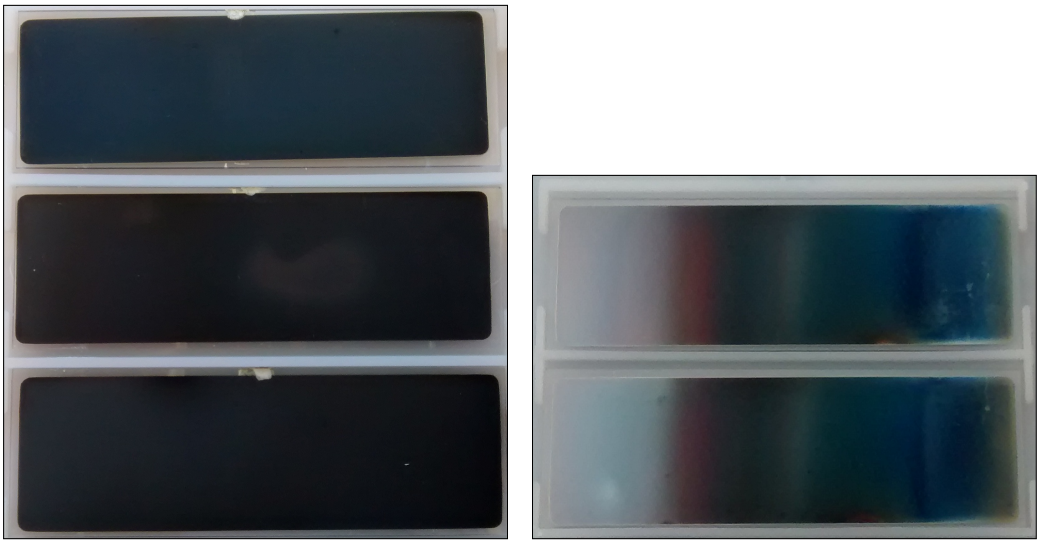

(a) Samples without the baffle. Sample 1 top, sample 2 middle, sample 3 bottom

(b) Samples with the baffle. Sample A top, sample B bottom, CuS rich end to the left and Bi rich end to the right

Figure 4.42: Images of co-evaporated samples

Samples with the Baffle

Two more samples, samples A and B, were made by repeating the conditions in the previous section and introducing a baffle to create a compositional gradient as discussed in Section 3.2.3. The thickness of the samples as measured by the quartz crystal monitor were 239 nm and 247 nm for samples A and B respectively.

Figure 4.42b shows the samples have a clear band structure from left to right. At the CuS rich end they are a light reflective grey turning in a brown-red colour then a dark green band followed by a dark blue band at the bismuth rich end.

XRF was used to measure the change in elemental composition across the samples and is reported in Figure 4.43. The start of the sample is the edge closest to the CuS source to mirror the proposed phase diagram already discussed. If Cu_3BiS_3 is desired we should look for a point with ratios of Cu/Bi and S/metal at 3 and 0.75 respectively. The first 5 points on each sample have Cu/Bi near or greater than 3 then drops off as an exponential decay towards the more bismuth rich end of the slide. In both samples there appears to be less sulphur than expected as the S/metal ratio never exceeds 0.5. Due to the low sulphur content Cu/S is also plotted and shows it as high as 2 before dropping to unity at 55 mm and then below in both samples.

XRD was also preformed across the samples to identify the phases present. The XRD spectra are shown for both ends of the samples and a 3D representation is included to show how the phase changes from one end of the sample to the other in Figure 4.44 The results for both samples are very similar. In both samples there are strong bismuth metal peaks at bismuth end of the sample. These peaks decrease the closer to the CuS you are to be replaced with a series of much smaller peaks. No probable phase matched more than one of these peak at any one time and the phases were left undetermined. Unfortunately Cu_3BiS_3 was not found on either sample.

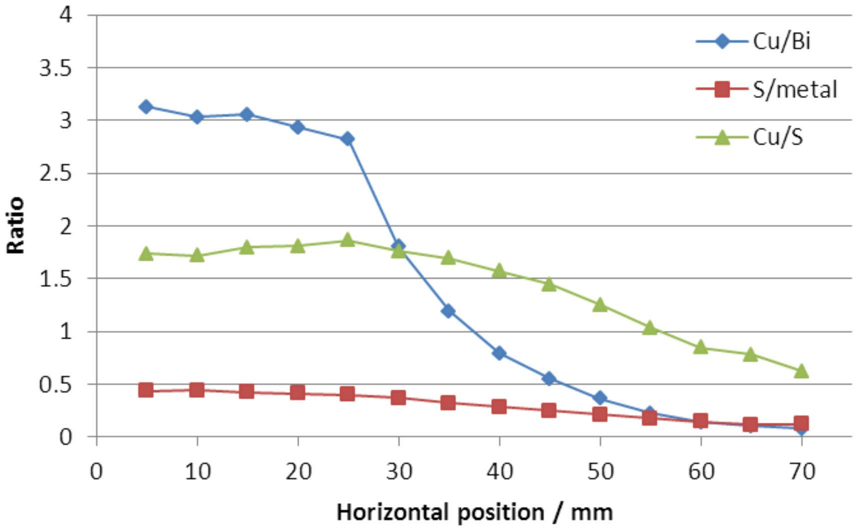

(a) Sample A

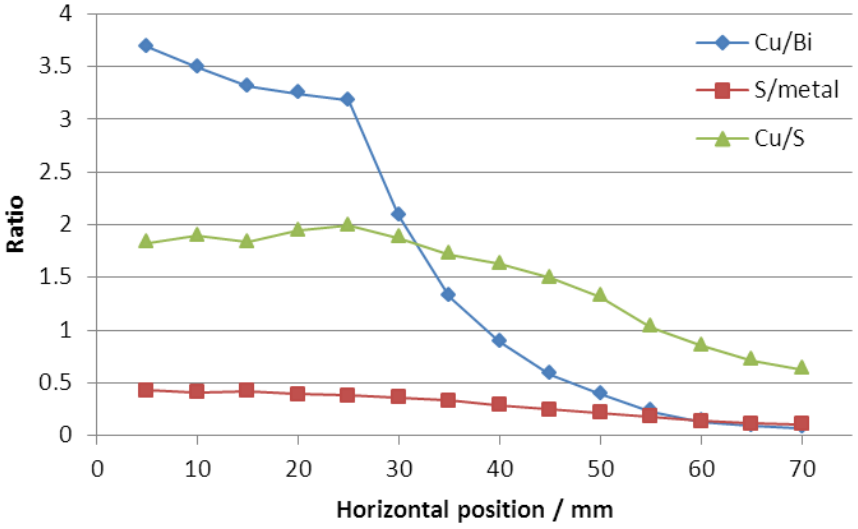

(b) Sample B

Figure 4.43: Compositional gradient of co-evaporated samples with a baffle

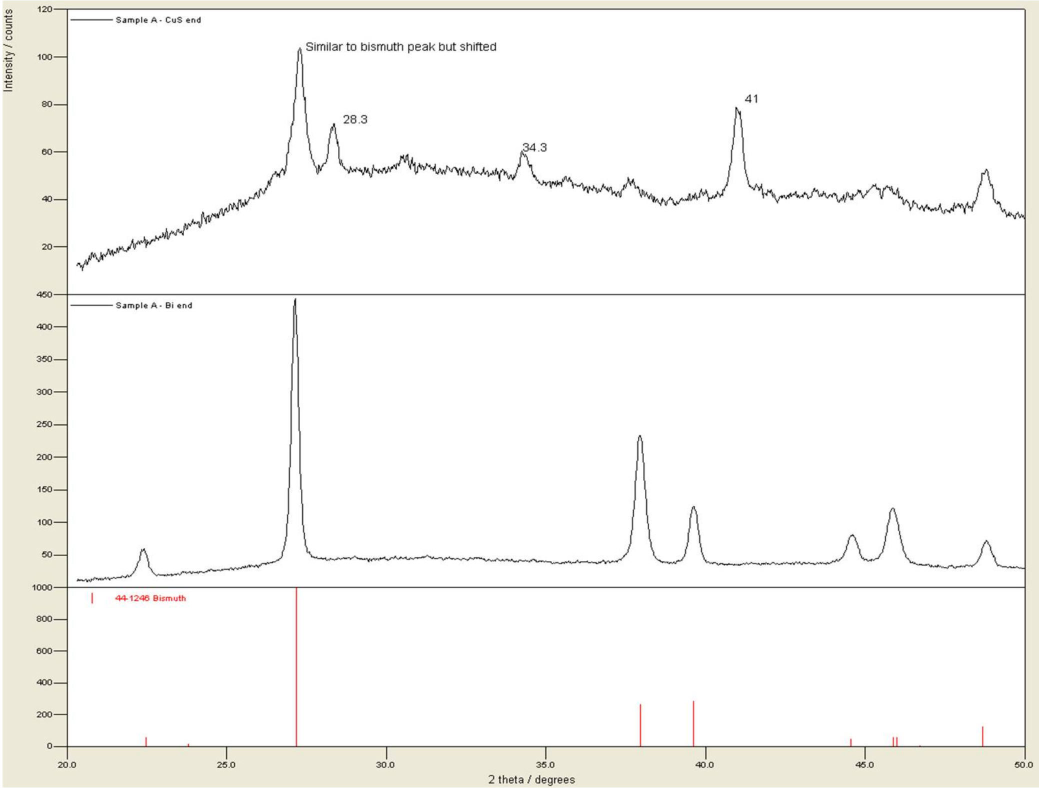

(a) XRD at points at either end of Sample A

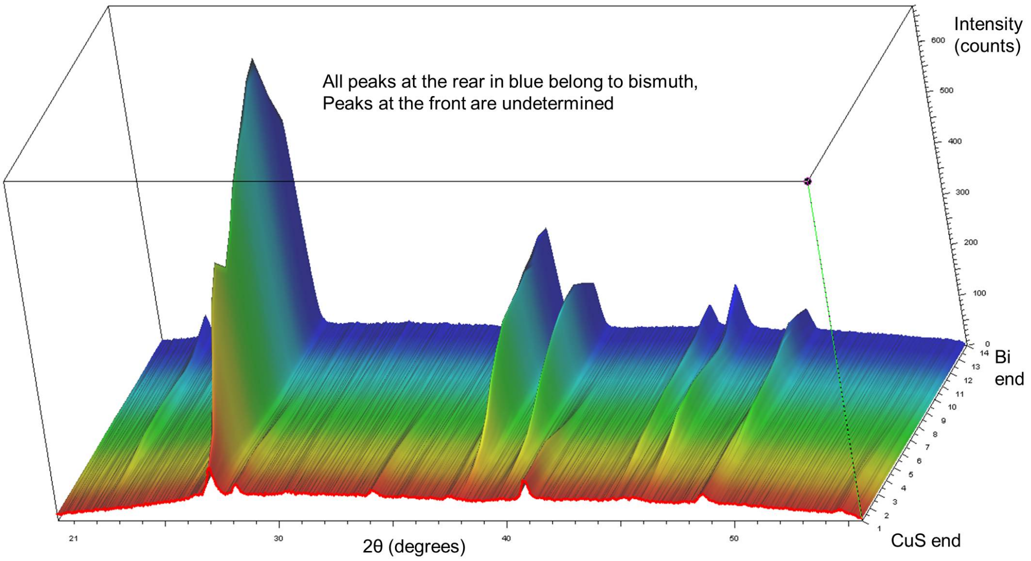

(b) 3D representation of phase changes across sample A

Figure 4.44: XRD of co-evaporated Sample A with a baffle

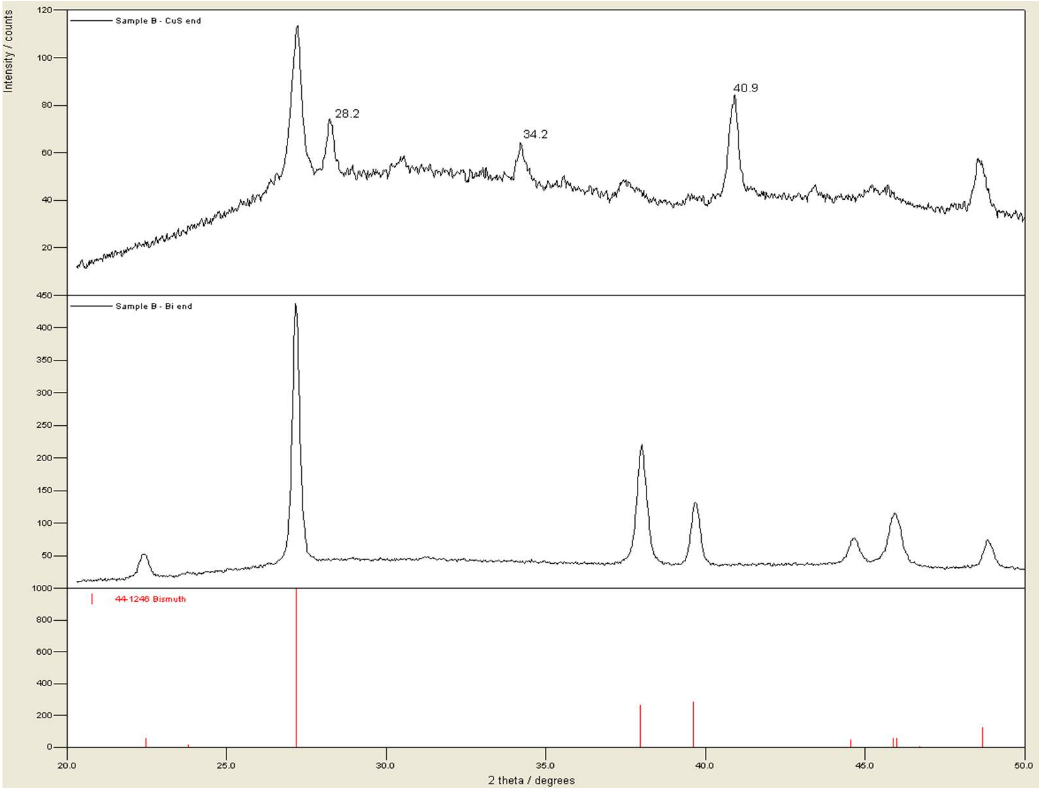

(a) XRD at points at either end of Sample B

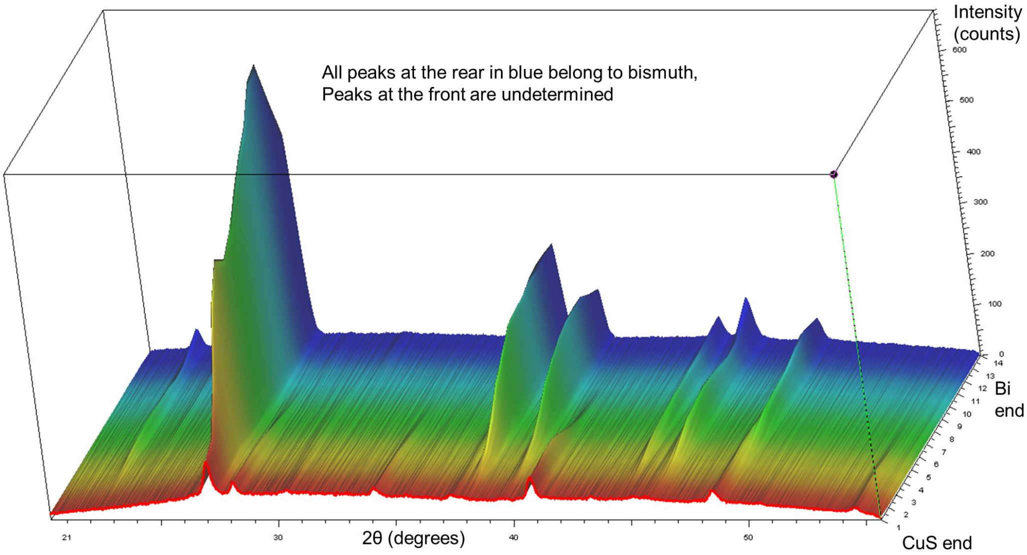
All peaks at the rear in blue belong to bismuth,
Peaks at the front are undetermined

(b) 3D representation of phase changes across sample B

Figure 4.45: XRD of co-evaporated Sample B with a baffle

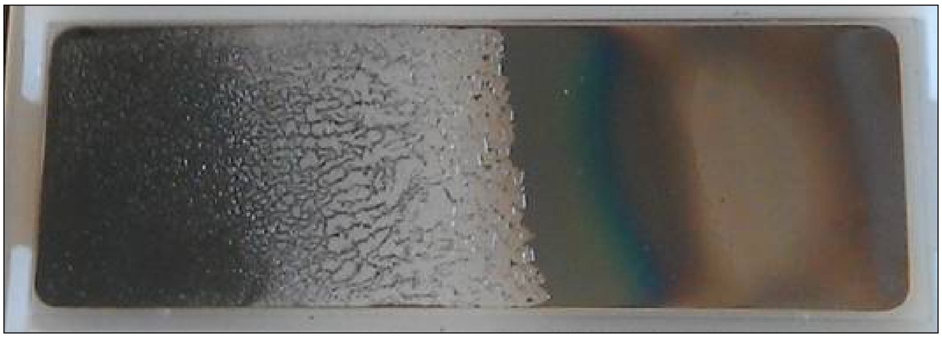

Figure 4.46: Image of an evaporated sample found to contain Cu_3BiS_3

Film of Cu_3BiS_3

Throughout the above study there were many test samples created, one of which is presented below. Copper sulphide and bismuth were both evaporated from alumina crucibles for 26 min and the quartz crystal monitor measured 379 nm as the thickness near the midpoint. Maximum current was applied to the CuS source and 55 A was applied to the bismuth source. For this sample the glass slide was not heated. A large region did not adhere well and the 40 mm of the sample nearest the CuS source partially peeled off. Figure 4.46 shows the sample and the peeling. Otherwise the sample was shiny, smooth, dark with a blue-green tint near the peeled region. The CuS end was slightly translucent when held up the light and the bismuth end was opaque.

Composition was measured by EDX and is shown in Figure 4.47. The first half of the sample is very erratic due to the broken nature of the surface of the sample it is unlikely these measurements are accurate. The second half of the sample where there is continuous film the measurement appears more stable showing a Cu/Bi ratio of about 3 or 4 and decreasing to less that 1 at the Bi rich end. The S/metal ratio varied between 0.5 and 0.8 over this section of the sample. Cu_3BiS_3 has a

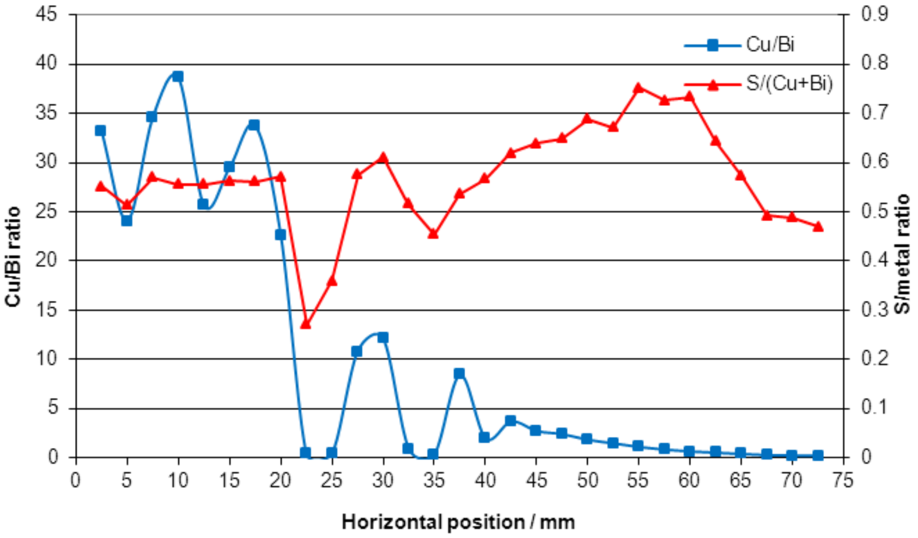

Figure 4.47: Composition of evaporated sample found to contain Cu_3BiS_3

S/metal ratio of 0.75 so this is in the right ball park.

XRD was performed across the whole sample and is shown in Figure 4.48. At point 1 (the CuS rich end) the peaks for Cu_9S_5 were detected, after point 1 the peaks were very low due to the fragmented nature of the film and no peaks could be identified. At point 7 which is 35 mm into the sample Cu_3BiS_3 (PDF card number 43-4179) was observed. The film is still broken at this point and the signal to background ratio is high but the main peaks of Cu_3BiS_3 can be clearly seen in Figure 4.48a. Towards the bismuth rich end where the film is better adhered the diffraction peaks are more pronounced, bismuth and Bi_2S_3 were observed. Figure 4.48b shows a 3D representation of XRD across the sample from here it can be seen how weak the Cu_3BiS_3 signal was in comparison to phases at either end of the sample.

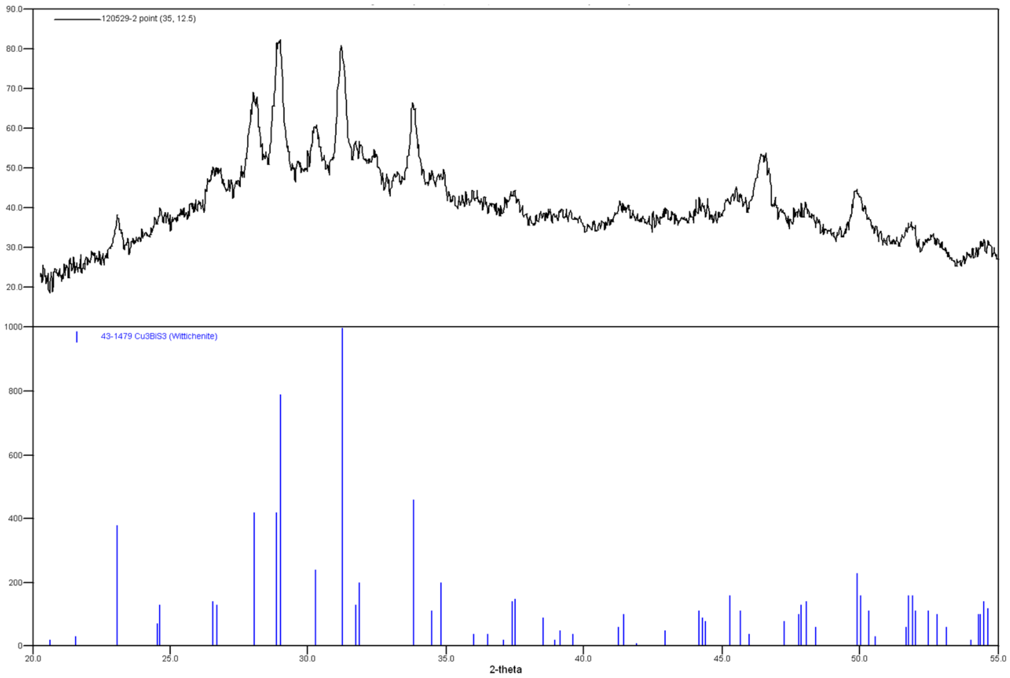

(a) XRD of point 7 (35 mm into sample)

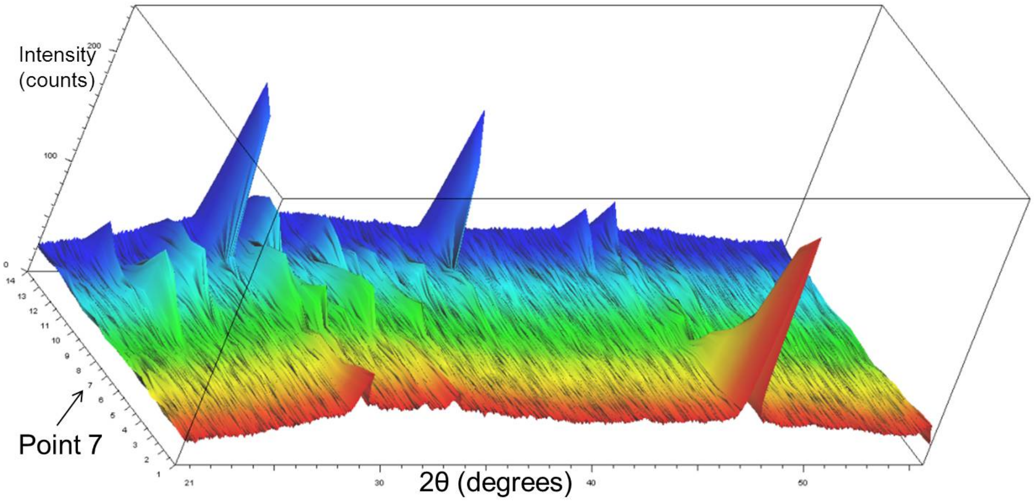

(b) 3D representation of phase change across sample

Figure 4.48: XRD of of evaporated sample showing presence of Cu_3BiS_3

4.4 Summary of Results

In this chapter the results from analysing several samples of various compositions of copper sulphide and bismuth were presented. XRD provided phase information of the samples quenched from 380 °C and from 510 °C. In both cases SEM was carried out to support the results from XRD. The phase information will help determine what phases are present on the 380 °C and from 510 °C isotherms on the CuS−Bi pseudo-binary phase diagram constructed in the discussion chapter. The pseudo-binary phase diagram will be constructed using the DSC results obtained in this chapter. Groups of thermal events from different compositions were related and analysed for inclusion into the phase diagram.

The second stage of the investigation showed that Cu_3BiS_3 films could be grown using two different deposition techniques. The first used DC magnetron sputtering to deposit metallic precursor films which where than sulphurised. Initial work using compositional libraries and sulphuring by thermal evaporation of a sulphur layer did not produce layers that adhered well and they contained mostly binary phases which hindered phase analysis. When the binary layers were etched away it appeared Cu_3BiS_3 was not present on the films. Two novel annealing techniques were attempted both with the aim to use higher temperatures to help conversion but controlled in way to improve film adhesion. One involved annealing twice, once at 250 °C and again at 500 °C with extra sulphur evaporated onto the film in between anneals. The second used a small sulphur pellet in a two stage controlled anneal. Samples were held at 250 °C for 30 min and then the temperature was raised to 500 °C. It was shown both annealing techniques produced films of Cu_3BiS_3.

The second deposition technique used thermal evaporation to deposit CuS and Bi directly onto the substrate. Evaporated copper sulphide was shown to produce films with a Cu/S ratio close to unity and then was evaporated with bismuth. Although the evaporated samples appeared to be well adhered they did not produce Cu_3BiS_3 reliably with the conditions tested. However, the XRD on one sample did show a region of single phase Cu_3BiS_3 showing that this technique can work and may need to be optimised.

The following chapters will discuss how this work fits into the wider field of knowledge and what should be done to continue this work.

Chapter 5

Discussion

5.1 Phase diagram

A series of samples were made from bismuth and copper sulphide powders and annealed at 380 °C for 2.5 months. After the annealing the samples were measured using ED-XRF and it was decided to use the calculated composition from the weighed starting materials instead. The possibly of sending the samples for commercial analysis using other techniques was explored but many companies stated they could not measure across the expected composition range. Sulphur and bismuth are difficult to differentiate using ED-XRF because the most prominent emission lines of sulphur, the Kα lines, overlap with the M lines of bismuth. In an attempt to mitigate against this in our measurements the sulphur content was inferred from the copper content and the bismuth content was measured from its Lβ line which does not overlap with any other lines. This was done because CuS was used as a starting material so the mole fraction of sulphur should equal the mole fraction of copper in each pellet. However, the measurements in Table 4.1

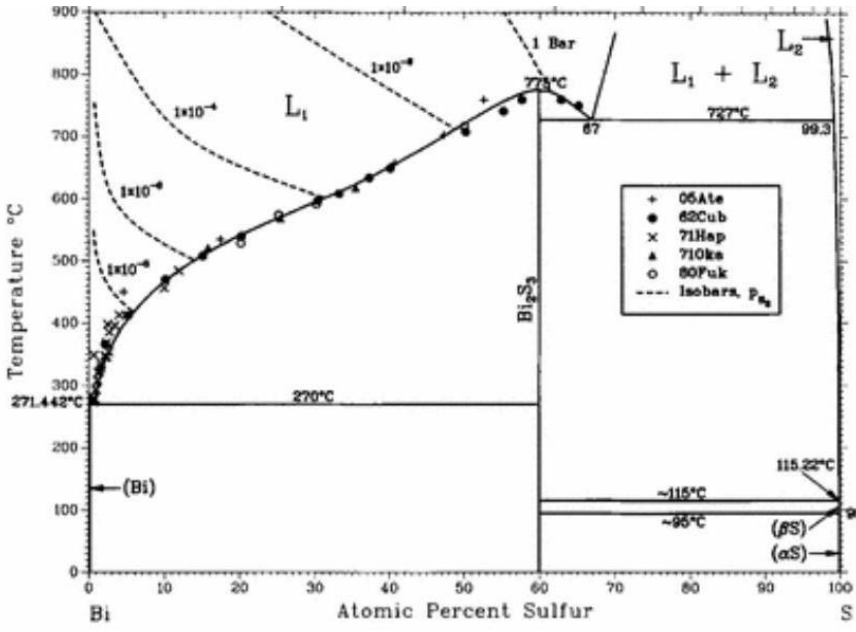

Figure 5.1: The Bi−S binary phase diagram [60]

suggest a loss of bismuth which was not observed as it would have left a film or a precipitate on the inside of the ampoule during annealing. Other work such as Sugaki and Shima [49] appear to rely on the weighed starting materials for composition and it was decided it would be appropriate to do the same in this study. The samples covered the full range from 0 mol % Bi to 100 mol % Bi of the CuS−Bi join across the Cu−Bi−S material system.

The regular binary phase diagrams that bound the ternary phase diagram are Cu−Bi, Bi−S, and Cu−S phase diagrams and are shown in Figures 2.3, 5.1 and 5.2 respectively. These have been redrawn and scaled to show an extended phase diagram which wraps around the perimeter of the Cu−Bi−S ternary phase diagram starting from the sulphur apex and moving to the copper apex, the bismuth apex and then back the to sulphur apex. This extended S−Cu−Bi−S diagram is shown in Figure 5.3.

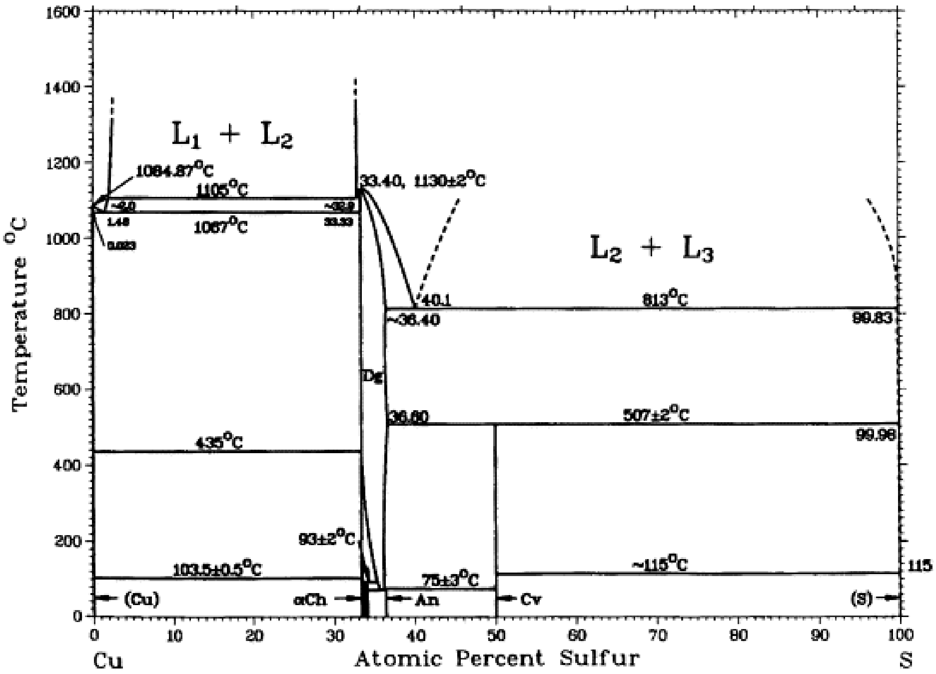

Figure 5.2: The Cu−S binary phase diagram [55]

What can be seen from these diagrams are the start and end points of the CuS−Bi phase diagram and possible hints at the interior. At the bismuth apex where two phase diagrams meet it can be seen that there is a phase change at 270 °C to 271 °C which is the melting point of bismuth. This is observed in the results across the whole sample range and would be represented on the CuS−Bi phase diagram as a horizontal line much like in the Cu−Bi phase diagram or half of the Bi−S phase diagram. It can also be seen that there is a eutectic extremely close to pure bismuth and a liquidus leading upward steeply as the proportion of copper or sulphur increases. Given that the CuS−Bi phase diagram bisects these phase diagrams at the bismuth apex it would be reasonable to assume this feature will also be present. Indeed at 92 mol % Bi a small thermal event can be seen in Table 4.3 at 540 °C which could be this liquidus. The location of the eutectic is

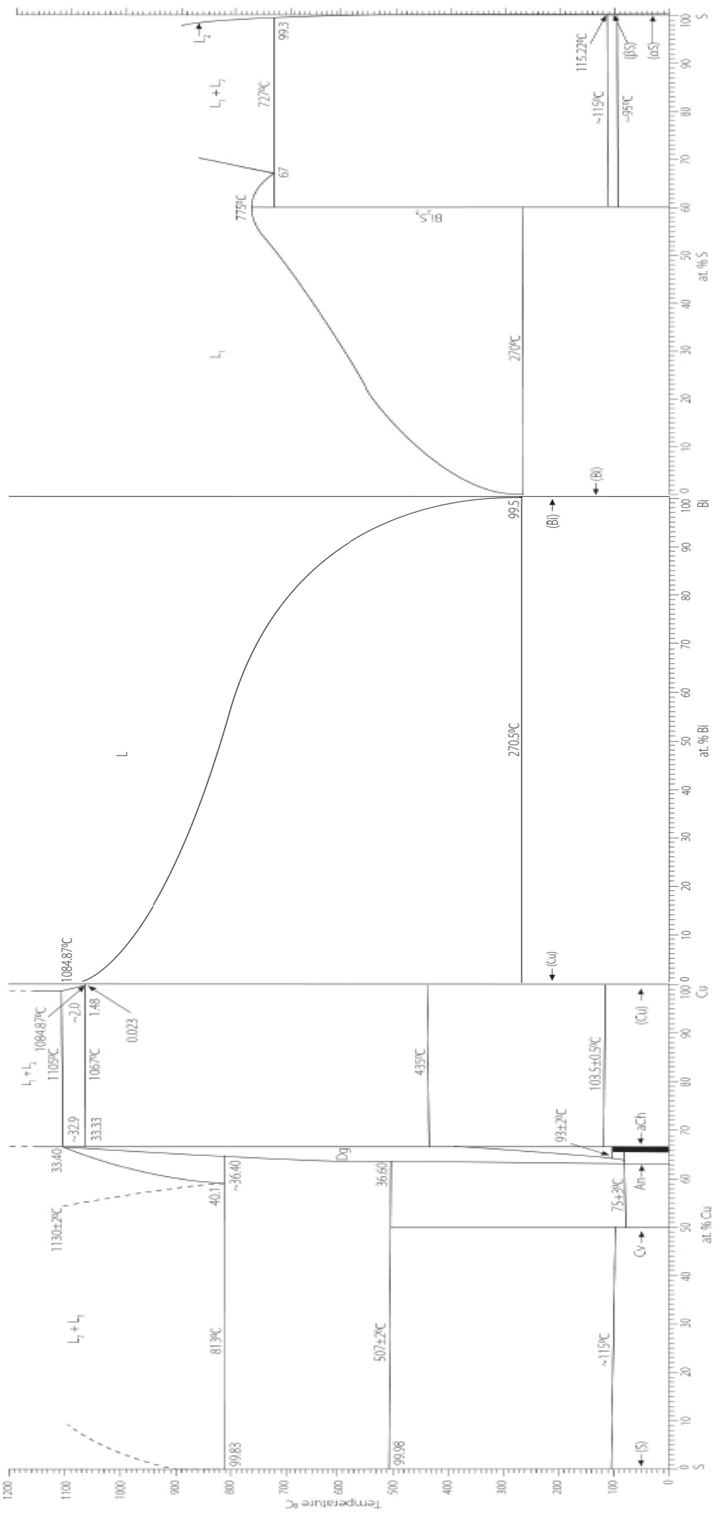

Figure 5.3: Boundaries of the Cu−Bi−S System

likely to be in the order of <1 mol % Bi from the edge just like in the two phase diagrams and has been drawn on the final CuS−Bi phase diagram.

In the S−Cu section or the Cu−S phase diagram in Figure 5.2 which is as it appears in Blachnik and Müller [55] the thermal events of CuS can be read. The starting material CuS is at 50 at % S and marked as ‘Cv’ for covellite. At 507 °C it decomposes peritectically into a liquid and $Cu_{2\text{-}x}S$ and this mixture doesn’t change again until 813 °C. To either side of covellite are phase changes at 75 °C and 115 °C so there is a possibility that if there were any impurities due to the starting material not having a Cu/S ratio exactly 1 then some peaks at these temperatures might be seen. Figures 4.4 and 4.5 do show some small peaks measured near 75 °C and 115 °C but it is very difficult to conclude whether they are due to these impurities or not.

There were many smaller peaks in Figure 4.5 that did not obviously belong in any of the groups of events marked in Figure 4.6 It may be possible to get an idea whether these are errors or should be included in the system by looking at other phase diagrams that intersect with CuS−Bi. Overall there is very little information on the Cu−Bi−S material system in the literature but a total of five phase diagrams crossing the interior of the Cu−Bi−S system were found. In addition to the $Cu_2S-Bi_2S_3$ phase diagram in Figure 2.6, Figures 5.4 to 5.7 show four more known pseudo-binary phase diagrams in the Cu−Bi−S material system from various studies [61–63].

Each of these phase diagrams cross the Cu−Bi line at various locations and at those points they share the same composition and therefore the same properties, including phase regions and transitions. Figure 2.7b shows on a plan view where these phase diagrams are located within the Cu−Bi−S system and Table 5.1 gives

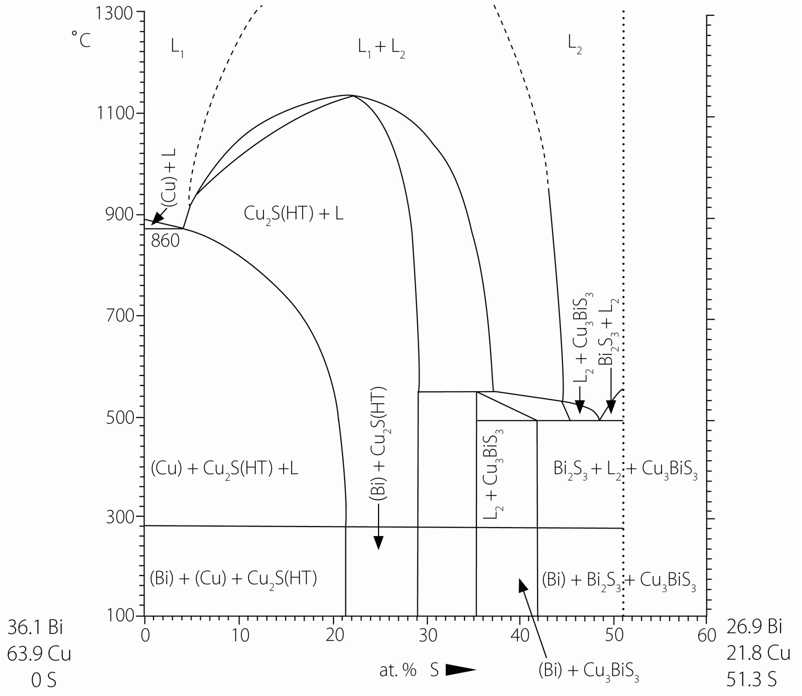

Figure 5.4: Phase diagram for approx. $Cu_2Bi-CuBiS_2$ [63]

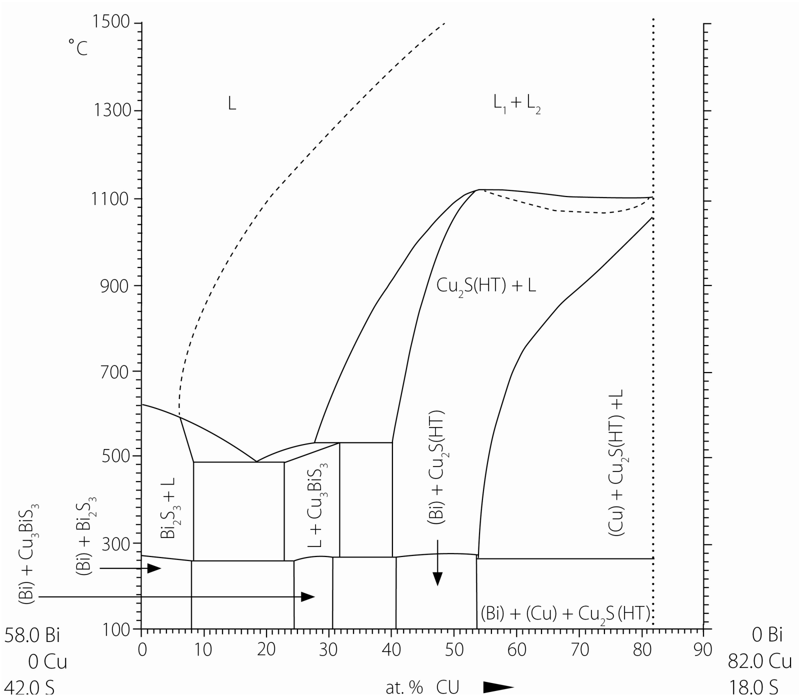

Figure 5.5: Phase diagram for approx. $Bi_3S_2-Cu_4S$ [63]

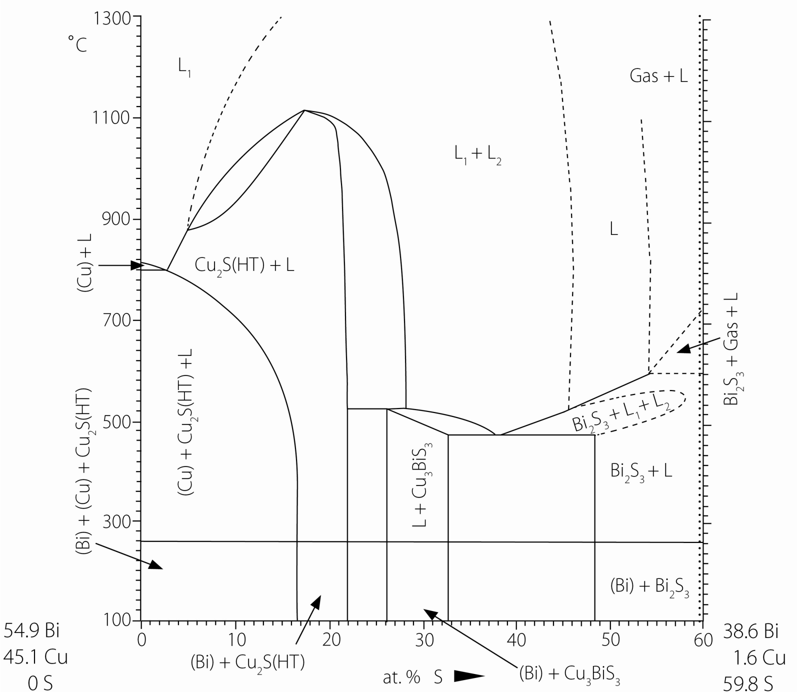

Figure 5.6: Phase diagram for approx. $CuBi-Bi_2S_3$ [63]

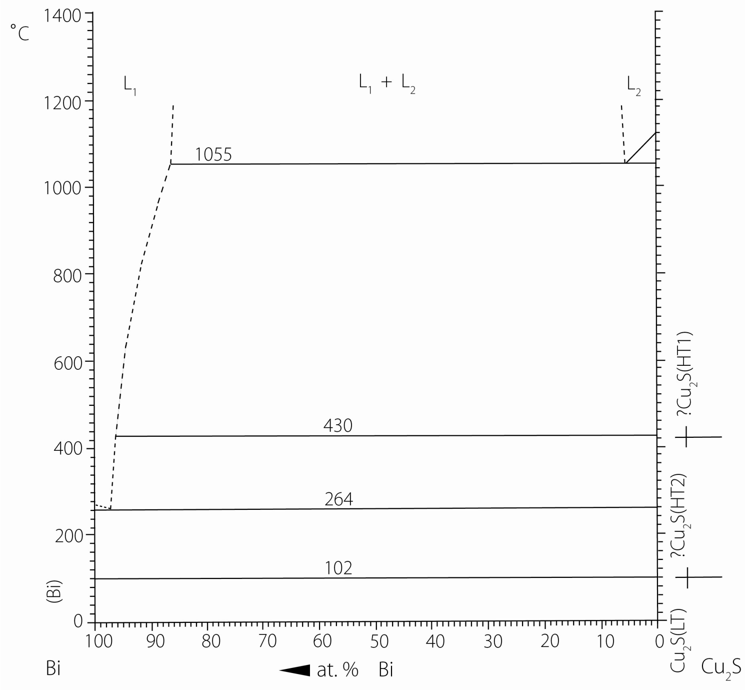

Figure 5.7: Phase diagram for $Bi-Cu_2S$ [62]

the details of the the crossing points along with the thermal events we would expect to see in our phase diagram from the phase diagrams in the literature. The crossing points were calculated by scaling the composition at one end of each phase diagram to the composition at the other end and finding the point at which the atomic fraction of copper equals the atomic fraction of sulphur which is a condition unique to all points on the CuS−Bi phase diagram. The atomic composition at these points were then converted into a molar percent of copper sulphide and bismuth to find the corresponding point on the CuS−Bi phase diagram.

Figure	Intersects CuS−Bi	Composition (mol % Bi)	Thermal events (°C)		
2.6	75 mol % Cu_2S	25	400	527	610
5.4	35 at % S	46	275	540	840
5.5	33 at % Cu	52	270	530	720
5.6	26 at % S	65	260	530	960
5.7	100 at % Bi	100	102	264	

Table 5.1: Intersections of phase diagrams with CuS−Bi phase diagram

The temperatures in this table in the region of 260 °C to 275 °C agree with the melting point of bismuth which was observed on all the samples during DSC. The temperatures of the phase changes in the $Cu_2S-Bi_2S_3$ phase diagram (Figure 2.6) match approximately with the temperatures measured for the 25 mol % Bi sample. The thermal event at 400 °C was read from a very steep line in Figure 2.6 so there could be a large error on that, it could well correspond to the point in Group C measured at 485 °C and at 25 mol % Bi. If this is the case it might offer an explanation for what the events in Group C mean. In Figure 2.6 it can be seen the single phase region of Cu_3Bi_3S bends to the right and the events could be the transition where the region bends away. This could be where Cu_3BiS_3

starts to break down into other ternary, Cu_9BiS_6. Although this is speculative. The temperatures in the table in the region of 530 °C to 540 °C appear to be a continuation of Group D, the deconvolved overlapping peaks are close to these but are of a slightly higher temperature. It is very difficult to reconcile these and so will be left out of the partial phase diagram for now. They occupy a high temperature region, and although interesting this is not a region that helps with the fabrication of Cu_3BiS_3.

5.1.1 Proposed Partial Phase Diagram for CuS–Bi

The temperatures of events A and B change very little over the compositional range at which they take place. The temperature of event A is 269(5) °C and the temperature of event B is 632(5) °C. The temperature of events C and D depend on composition. The Tammann diagram for Group C would suggest event C intersects event A at 5 mol % Bi and ends at 52 mol % Bi at a temperature of 375(5) °C. The Tammann diagram for Group D would suggest event D starts at 7 mol % Bi and ends at 54 mol % Bi. The closest measured temperatures to these points are 573 °C at 8 mol % Bi and 569 °C at 52 mol % Bi. Taking the information above Figure 5.8 was drawn as a proposed partial pseudo-binary phase diagram for the CuS−Bi system. This diagram is incomplete as there are some thermal events above 500 °C in the higher bismuth content region that could not be reconciled with known data. If more samples were made to provide a higher resolution across the phase diagram it might have been possible to relate the two but as it stands it is not possible. Further investigation into this region of the phase diagram would possible as further work to complete the phase diagram.

5.2 Thin Film Sputtering

Libraries that spanned a large composition range were made by sputtering metallic precursors, however the precursors did not appear to adhere well to the glass slides used in this investigation. After evaporating sulphur onto the precursor and annealing at a low temperature for a long time most of the films appeared to be binary sulphide phases. The only region suspected of containing Cu_3BiS_3 was destroyed during a KCN etch to remove the copper sulphides. Whereas an anneal

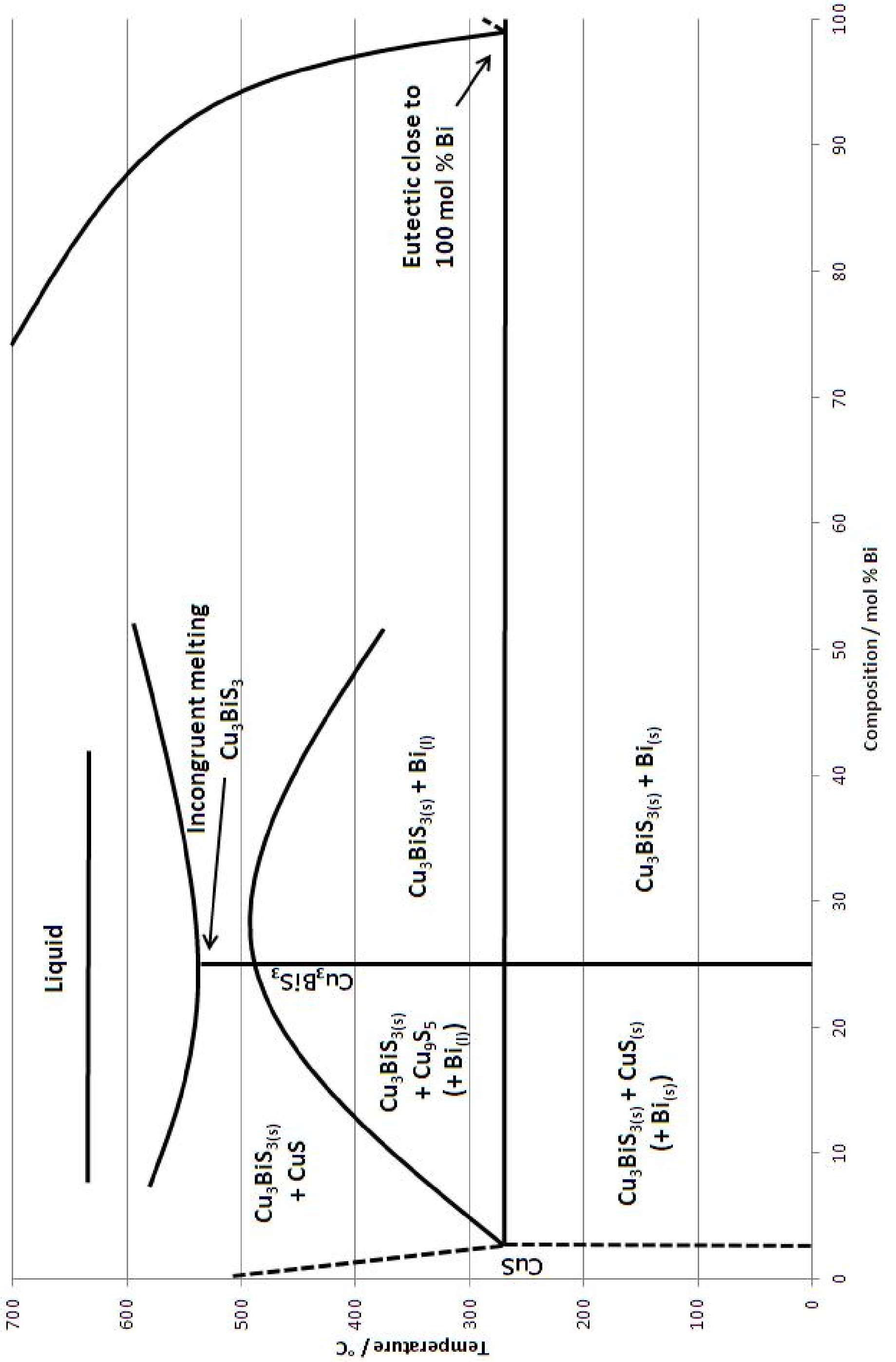

Figure 5.8: CuS−Bi Phase Diagram

at 270 °C worked for Gerein and Haber [38] it did not work here with elemental sulphur.

A double anneal and two stage anneal were shown to be successful in making films of Cu_3BiS_3. Both techniques were designed to avoid melting bismuth by waiting at an appropriate temperature for bismuth to fully react with sulphur before raising the temperature higher to promote a reaction into ternary phases. In all cases annealing at 250 °C for 30 min is long enough to convert all bismuth into Bi_2S_3, bismuth metal is not detected by XRD on any of the slides which underwent this treatment. When the sulphide films were heated to 500 °C for 30 min Cu_3BiS_3 was found. The Cu_3BiS_3 portion of the films were either translucent or discontinuous with large gaps. The presence of Cu_3BiS_3 in the films using these techniques is encouraging. Refinement of either process should lead to the deposition of solid continuous films which would be suitable for testing for suitability in solar applications.

Since this work was undertaken others have attempted grow films of Cu_3BiS_3 using sputtering of metals then annealing in a sulphur atmosphere. For example Yakushev et al. [64] grew and measured the optical properties of Cu_3BiS_3 films. In their study they sputtered copper and bismuth onto molybdenum coated soda-lime glass. An excess of sulphur was evaporated onto the film and then annealed at 250 °C for 30 min. The annealing took place in an argon atmosphere at 100 Pa. These conditions are similar to those used for the libraries presented at the start of the sputtering section with two main differences. The first being the substrate, plain soda-lime glass was used in this study and they used molybdenum coated soda-lime glass. The molybdenum, purposefully avoided in this study so as not to complicate XRD measurements, may have helped with the adhesion of the films by laying a surface more suitable for the deposition of copper and bismuth than bare glass. Also the sulphurisation technique used in this study used evacuated ampoules in the annealing step which may have encouraged the sulphur into the vapour phase resisting reaction with the film.

5.3 Thin Film Evaporation

Thermal evaporation was attempted as an alternative to sputtering. It allows the direct deposition of sulphur in the form of CuS which removes the need for further processing which was found to be detrimental to films in the previous section. In general evaporation gives smooth well adhered films which was found to be difficult to obtain using sputtering. Both these reasons help simplify the process and should help improve the resulting film. Also, because CuS can be deposited with bismuth it provides a direct comparison with the bulk CuS$-$Bi phase diagram. This phase diagram has fewer phases present than the $Cu_2S-Bi_2S_3$ phase diagram in Figure 2.6. Having fewer phases means there may be less potential for contamination from unwanted phases and could mean the process is easier than evaporating Cu_2S and Bi_2S_3.

Copper sulphide and bismuth were evaporated together and a baffle was used to create some shadowing to get a thickness gradient of each across the samples. Initially a series of copper sulphide films were evaporated on their own and the ratio of copper to sulphur across each sample was investigated to make sure the ratio remained close to unity. At the early stages of evaporation it was seen that the CuS powder de-gases. This de-gassing could be either impurities, moisture, or sulphur from the breakdown of CuS leaving the source. From the Cu$-$S phase diagram in Figure 5.2 and as discussed in the phase diagram work CuS breaks down into $Cu_{2\text{-}x}S$ and a sulphur rich liquid at 507 °C. The boat or coil glowed brightly during evaporation so it would be safe to assume the CuS was heated to above that temperature and this could be the explanation of the de-gassing. When samples were exposed to the de-gassing they had higher Cu/S ratios than expected (when using an alumina crucible) but when a shutter was used to shield the substrate as the source was heated the ratio of the final samples approached unity. One possibility of why this is is that the degassing may coat the glass slide with a film that preferentially adheres to copper more than sulphur. Bismuth was relatively easy to evaporate, it has a low melting point of 271 °C and is a single element so there is no danger of decomposition before evaporation like with CuS. Both the CuS and bismuth films were very smooth and adhered well to the slide which was one of the reasons for trying evaporation and was a good sign for the next step of co-evaporation.

In the series of samples which didn't use a baffle the Cu/Bi ratio was between 1 and 2 meaning that there was more bismuth deposited than desired which would support the above possibility. Bismuth evaporates at a much lower temperature than CuS so it may be affected by the heat given off by the much hotter CuS source during co-evaporation. Copper sulphide required such a large current to produce enough heat for evaporation it is very possible that it added radiant heat to the bismuth source and increased its rate of evaporation. Although, when the same deposition conditions were attempted but with a baffle to get a gradient the Cu/Bi ratio for a large portion of the sample rose to 3 or just above which was the desired ratio. It appears there was thermal leakage between the sources in the first set of samples but it was partially mitigated by the placement of the baffle in the second set. It may have been covering more of the bismuth source than the CuS source. The positioning, height and size of the baffle was more of less trial and error and could be optimised further. Another reason for a high bismuth content could be the way the deposition was ended. Deposition ended whenever CuS was exhausted and a drop in the deposition rate was observed by the quartz crystal monitor. In the time taken to observe the drop and close the shutter a film of only bismuth could have deposited on top of the samples. This might add to the high bismuth content of samples 1 to 3 but would also help explain the prevalence of strong bismuth peaks in the XRD spectra for all the samples, with or without the baffle being used. To mitigate against either of these occurrences it would have been prudent to have used some sort of thermal shielding between the sources and also time the deposition rather than wait until one source was depleted.

Another unusual feature found in the co-evaporation samples is the Cu/S ratio. When CuS was evaporated on its own it remained close to one, but during co-evaporation without a baffle it increased to 2 or slightly more. This unfortunately means that is the samples cannot be directly compared to the phase diagram already discussed. The increase in sulphur would take the composition of the slide off the range between 100 % CuS and 100 % bismuth.

The use of a baffle in the second set of samples was shown to successfully produce a gradient across sample A and B as can be seen in Figure 4.43. Both the Cu/Bi and S/metal ratios decrease when moving toward the bismuth rich end. The rate of change is not constant, it changes very slowly to begin with then much more rapidly after 25 mm into the sample. This might have something to do with the positioning of the baffle and would be something that could be looked at further but it shows the principle works. Samples A and B are smooth and are well adhered to the slide, a band structure can be seen across the slide although the XRD results do not appear to match the change in appearance to phases present. Bismuth can see seen across much of the sample A and B with a much more minor unidentified phase emerging near the CuS end of the samples. These did not show Cu_3BiS_3 anywhere and like the other samples where sulphur poor.

The final film presented was a little different to the others as it didn't follow the path of the main investigation but may offer a hint at where efforts could be directed to reproduce Cu_3BiS_3 in the future. In this case the film was evaporated onto an unheated substrate. One thing to note that this film has a S/metal ratio higher than any of the other evaporated samples. When the glass slide was heated to 200 °C to encourage a reaction on the surface it may have made it more difficult for sulphur to adhere. Sulphur melts at a very low temperature of 115 °C so it may have partially evaporated off again before reacting with bismuth. If using a lower temperature substrate improves the chemical composition it appears it also hinders adhesion. The CuS rich side of the sample mostly peeled off. XRD was used to identify Cu_3BiS_3 in the region where the film was peeling off. The background was large so much of the signal was from the amorphous glass which was exposed between flakes of film. It would be interesting to test a range of substrate temperatures to see if this has an impact on both the formation of Cu_3BiS_3 and the adhesion of the film. Perhaps there is a compromise where both can be achieved.

5.4 Summary of Discussion

Result from this investigation that are new and novel include the partial CuS−Bi phase diagram. The diagram presented was made up from the measurements obtained from DSC with the exception of the points at either side of the phase diagram, pure Bi and pure CuS. They were taken from the literature. Literature was broadly in agreement with the events found on the 25 mol % Bi sample which is encouraging. The continuation of this study to include more points on the phase diagram and especially the higher bismuth regions would be beneficial as there is very limited information to date.

Finally it was shown that Cu_3BiS_3 can be grown using techniques commonplace in the thin film industry and used for other materials. Sputtering and evaporation. Both techniques were used to make films of Cu_3BiS_3 and show promise. Further work to optimise the processes would probably lead to higher quality films.

Chapter 6

Conclusions

6.1 Conclusions

A series of samples were made from bismuth and copper sulphide powders and analysed by DSC, XRD and SEM. The samples covered the whole compositional range from 100 % copper sulphide to 100 % bismuth and were analysed over a temperature range of at least 50 °C to 650 °C. The DSC heating curves showed a series of characteristic thermal events. The series were identified as the melting point of bismuth metal, the liquidus of the Cu−Bi−S system and the incongruant melting of Cu_3BiS_3. There was a fourth series of undetermined origin but is thought to be related to Cu_3BiS_3 due to the trends in the enthalpies in Tammann diagram. Constructing the phase diagram was a challenge due to possible contaminants and residual phases from thermal cycling. However, some regions were very clear, and especially around the Cu_3BiS_3 area at 25 mol % Bi. This is the most important region to this investigation since it contains Cu_3BiS_3. The CuS−Bi pseudo-phase diagram was constructed from the data and it shows that Cu_3BiS_3 is present for a wide range of compositions and only melts at temperatures in excess of 534 °C. This is helpful when attempting to make thin films of Cu_3BiS_3, it tells us that annealing above 534 °C may not work but that we can expect to see some Cu_3BiS_3 over a broad range on compositions otherwise.

Cu_3BiS_3 was identified on films grown by sputtering of metallic precursors which are then sulphurised by annealing. Sulphur was introduced by either evaporating it directly onto the film or by annealing the precursor with a sulphur pellet. The formation of Cu_3BiS_3 appeared to depend more on the annealing conditions. Given the long anneal of the first libraries it appears the reaction to Cu_3BiS_3 is sluggish at low temperature but higher temperatures risk compromising the film by melting any bismuth metal still present. Care must be taken to control the anneal to make sure all bismuth is sulphurised before raising the temperature to promote the reaction to Cu_3BiS_3 from CuS and Bi_2S_3. Cu_3BiS_3 was found and produced a very interestingly pattered film but the process needs development to to obtain continuous films that would be suitable for PV. Some conditions that would be useful to alter would be annealing time, temperature and pressure within the ampoule. Also, other substrates might help adhesion.

Cu_3BiS_3 was also identified during the evaporation work. Films were made evaporating CuS and Bi together. The adhesion in this particular sample was poor but in general the adhesion of the films from evaporation appear to be better than those from sputter deposition. This might have been due to the substrate temperature. It would be worth while developing this method to improve the adhesion, the most obvious conditions to alter being the substrate itself or its temperature.

6.2 Suggestions for Future Work

In order to refine the Cu_3BiS_3 phase diagram future work would include the following. More composition samples so that phase ranges could be more confidently drawn especially towards the bismuth rich side of the phase diagram and a higher temperature resolution could be obtained by using a lower heating rate. Both these would help to get more exact locations and would provide more points for extrapolation from Tammann diagrams. It would also help in determining which peaks observed are phase changes in the system or contamination from other phases.

In the thin film work it would be beneficial to develop both methods. Both methods were shown to produce Cu_3BiS_3 and with optimisation might well be able to produce high quality films of it. Currently Cu_3BiS_3 is present but not in a form that can be measured for suitability in photovoltaics due to its adhesion problems. For the sputtered films development of the second anneal would be worth while. Substrates other than glass could be trialled and the pressure within the ampoule changed. An investigation using different length of times for annealing and different temperatures might reveal a set of conditions that will produce continuous films. The thickness of the precursor could also be investigated, perhaps more material would stop the formation of Cu_3BiS_3 from opening up gaps in the film.

For evaporated films Cu_3BiS_3 was also found to have adhesion problems. The next step would be test various substrate heating temperatures as it was suggested it might have an impact on Cu_3BiS_3 formation and the adhesion of the film.

Once continuous films of Cu_3BiS can be grown future work would include testing them for suitability for photovoltaics. Photoconductivity measurements would be made and if positive future would could include making a device from

Cu_3BiS_3 and testing its efficiency.

Bibliography

[1] A. W. Crosby. *Children of the sun: A history of humanity's unappeasable appetite for energy*. W.W. Norton, 2006.

[2] Godfrey Boyle, editor. *Renewable Energy: Power for a Sustainable Future*. Oxford University Press, second edition, 2004.

[3] BP plc. BP statistical review of world energy 2013. Online, January 2014. URL `www.bp.com/statisticalreview`.

[4] Jenny Nelson. *The Physics of Solar Cells*. Imperial College Press, 2003.

[5] Solarbuzz. Strong growth forecast for solar PV industry in 2014 with demand reaching 49 GW, according to NPD Solarbuzz. Online, December 2013. URL `www.solarbuzz.com/news/recent-findings/strong-growth-forecast-solar-pv-industry-2014-demand-reaching-49-gw`.

[6] John Singleton. *Band Theory and Electronic Properties of Solids*. Oxford University Press, 2001.

[7] Greg Parker. *Introductory Semiconductor Device Physics*. Prentice Hall, 1994.

[8] S. M. Sze. *Semiconductor Devices: Physics and Technology*. Wiley, second edition, 2002.

[9] William Shockley and Hans J. Queisser. Detailed balance limit of efficiency of p-n junction solar cells. *Journal of Applied Physics*, 32(3):510–519, 1961. doi:10.1063/1.1736034.

[10] National Renewable Energy Laboratory. Reference solar spectral irradiance: Air Mass 1.5. Online, February 2014. URL `http://rredc.nrel.gov/solar/spectra/am1.5/`.

[11] Fraunhofer Institute for Solar Energy Systems, ISE. Photovoltaics Report. Online, November 2015. URL `www.ise.fraunhofer.de/en/downloads-englisch/pdf-files-englisch/photovoltaics-report-slides.pdf`.

[12] Hans Joachim Möller. *Semiconductors for Solar Cells*. Artech House, 1993.

[13] Armin G. Aberle. Thin-film solar cells. *Thin Solid Films*, 517(17):4706–4710, 2009. doi:10.1016/j.tsf.2009.03.056.

[14] First Solar. Main page. Online, April 2015. URL `www.firstsolar.com`.

[15] Jiawei Gong, Jing Liang, and K. Sumathy. Review on dye-sensitized solar cells (DSSCs): Fundamental concepts and novel materials. *Renewable and Sustainable Energy Reviews*, 16(8):5848–5860, 2012. doi:10.1016/j.rser.2012.04.044.

[16] Pablo P. Boix, Kazuteru Nonomura, Nripan Mathews, and Subodh G. Mhaisalkar. Current progress and future perspectives for organic/inorganic perovskite solar cells. *Materials Today*, 17(1):16–23, 2014. doi:10.1016/j.mattod.2013.12.002.

[17] Xiaohan Yang and Ashraf Uddin. Effect of thermal annealing on P3HT:PCBM bulk-heterojunction organic solar cells: A critical review. *Renewable and Sustainable Energy Reviews*, 30:324–336, 2014. doi:10.1016/j.rser.2013.10.025.

[18] National Renewable Energy Laboratory. Main page. Online, May 2015. URL `www.nrel.gov`.

[19] Sharp Corporation. Sharp develops concentrator solar cell with world's highest conversion efficiency of 44.4 %. Online, June 2013. URL `www.sharp-world.com/corporate/news/130614.html`.

[20] Fraunhofer ISE. New world record for solar cell efficiency at 46 %. Online, April 2015. URL `www.ise.fraunhofer.de/en/press-and-media/press-releases/press-releases-2014/new-world-record-for-solar-cell-efficiency-at-46-percent`.

[21] Webmineral. Wittichenite mineral data. Online, September 2013. URL `http://webmineral.com/data/Wittichenite.shtml`.

[22] Stuart J C Irvine, editor. *Materials Challenges: Inorganic Photovoltaic Solar Energy*. RSC Energy and Environment Series. The Royal Society of Chemistry, 2015. ISBN 978-1-84973-187-4. doi:10.1039/9781849733465. 190-202 for 6.4 Sulfosalts section 196-198 for 6.4.2 Cu-Bi-S section.

[23] US Geological Survey. Main page. Online, April 2014. URL `www.usgs.gov`.

[24] D. L. Staebler and C. R. Wronski. Reversible conductivity changes in discharge-produced amorphous Si. *Applied Physics Letters*, 31(4):292–294, 1977. doi:10.1063/1.89674.

[25] N. Romeo, A. Bosio, V. Canevari, and A. Podestà. Recent progress on CdTe/CdS thin film solar cells. *Solar Energy*, 77(6):795–801, 2004. doi:10.1016/j.solener.2004.07.011.

[26] Selya Price and Robert Margolis. 2008 Solar technologies market report. Online, January 2010. URL `www.nrel.gov/tech_deployment/pdfs/2008_solar_market_report.pdf`.

[27] Philip Jackson, Dimitrios Hariskos, Roland Wuerz, Oliver Kiowski, Andreas Bauer, Theresa Magorian Friedlmeier, and Michael Powalla. Properties of Cu(In$_G$a)Se$_2$ solar cells with new record efficiencies up to 21 7%. *physica status solidi (RRL) – Rapid Research Letters*, 9(1):28–31, 2015. doi:10.1002/pssr.201409520.

[28] Kentaro Ito and Tatsuo Nakazawa. Electrical and optical properties of stannite-type quaternary semiconductor thin films. *Japanese Journal of Applied Physics*, 27(11R):2094, 1988. doi:10.1143/JJAP.27.2094.

[29] Kyle Hutchings. *High throughput combinatorial screening of Cu−Zn−Sn−S thin film libraries for the application of* Cu_2ZnSnS_4 *photovoltaic cells*. PhD thesis, Cranfield University, 2012.

[30] Wei Wang, Mark T. Winkler, Oki Gunawan, Tayfun Gokmen, Teodor K. Todorov, Yu Zhu, and David B. Mitzi. Device characteristics of CZTSSe thin-film solar cells with 12 6% efficiency. *Advanced Energy Materials*, 4(7), 2014. doi:10.1002/aenm.201301465.

[31] A. Rabhi, M. Kanzari, and B. Rezig. Growth and vacuum post-annealing effect on the properties of the new absorber $CuSbS_2$ thin films. *Materials Letters*, 62(20):3576–3578, 2008. doi:10.1016/j.matlet.2008.04.003.

[32] C. Garza, S. Shaji, A. Arato, E. Perez Tijerina, G. Alan Castillo, T. K. Das Roy, and B. Krishnan. p-Type $CuSbS_2$ thin films by thermal diffusion of copper into Sb_2S_3. *Solar Energy Materials and Solar Cells*, 95(8):2001–2005, 2011. doi:10.1016/j.solmat.2010.06.011.

[33] Y. Rodríguez-Lazcano, M. T. S. Nair, and P. K. Nair. $CuSbS_2$ thin film formed through annealing chemically deposited Sb_2S_3–CuS thin films. *Journal of*

Crystal Growth, 223(3):399–406, 2001. doi:10.1016/S0022-0248(01)00672-8.

[34] Nathan J. Gerein and Joel A. Haber. One-step synthesis and optical and electrical properties of thin film Cu_3BiS_3 for use as a solar absorber in photovoltaic devices. *Chemistry of Materials*, 18(26):6297–6302, 2006. doi:10.1021/cm061453r.

[35] Padmanabhan K. Nair, Santhamma M. Nair, Hailin Hu, Ling Huang, R. A. Zingaro, and E. A. Meyers. New p-type absorber films formed by interfacial diffusion in chemically deposited metal chalcogenide multilayer films. In *Optical Materials Technology for Energy Efficiency and Solar Energy Conversion XIV*, volume 2531, pages 208–219, 1995. doi:10.1117/12.217335.

[36] P. K. Nair, L. Huang, M. T. S. Nair, Hailin Hu, E. A. Meyers, and R. A. Zingaro. Formation of p-type Cu_3BiS_3 absorber thin films by annealing chemically deposited Bi_2S_3–CuS thin films. *Journal of Materials Research*, 12(3):651–656, 1997. doi:10.1557/JMR.1997.0099.

[37] Verónica Estrella, M. T. S. Nair, and P. K. Nair. Semiconducting Cu_3BiS_3 thin films formed by the solid-state reaction of CuS and bismuth thin films. *Semiconductor Science and Technology*, 18(2):190–194, 2003. doi:10.1088/0268-1242/18/2/322.

[38] Nathan J. Gerein and Joel A. Haber. Cu_3BiS_3, Cu_3BiS_4, Ga_3BiS_3 and $Cu_5Ga_2BiS_8$ as potential solar absorbers for thin film photovoltaics. In *Photovoltaic Specialists Conference, 2005. Conference Record of the Thirty-first IEEE*, pages 159–162, January 2005. doi:10.1109/PVSC.2005.1488095.

[39] Nathan J. Gerein and Joel A. Haber. Synthesis of Cu_3BiS_3 thin films by heating metal and metal sulfide precursor films under hydrogen sulfide. *Chemistry of Materials*, 18(26):6289–6296, 2006. doi:10.1021/cm061452z.

[40] Nathan J. Gerein and Joel A. Haber. Synthesis and optical and electrical properties of thin films Cu_3BiS_3—a potential solar absorber for photovoltaic devices. In *Photovoltaic Energy Conversion, Conference Record of the 2006 IEEE 4th World Conference on Photovoltaic Energy Conversion*, volume 1, pages 564–566, May 2006. doi:10.1109/WCPEC.2006.279518.

[41] F. Mesa and G. Gordillo. Effect of preparation conditions on the properties of Cu_3BiS_3 thin films grown by a two-step process. *Journal of Physics: Conference Series*, 167(1):012019, 2009. doi:10.1088/1742-6596/167/1/012019.

[42] F. Mesa, A. Dussan, and G. Gordillo. Study of the growth process and optoelectrical properties of nanocrystalline Cu_3BiS_3 thin films. *physica status solidi (c)*, 7(3-4):917–920, 2010. doi:10.1002/pssc.200982860.

[43] P. J. Dale, Laurence M. Peter, Andreas Løken, and Jonathan Scragg. Towards sustainable photovoltaic solar energy conversion: Studies of new absorber materials. *ECS Transactions*, 19(3):179–187, 2009. doi:10.1149/1.3120699.

[44] Diego Colombara, Laurence M. Peter, Keith D. Rogers, and Kyle Hutchings. Thermochemical and kinetic aspects of the sulfurization of Cu−Sb and Cu−Bi thin films. *Journal of Solid State Chemistry*, 186:36–46, 2012. doi:10.1016/j.jssc.2011.11.025.

[45] Craig R. Barrett. *The Principles of Engineering Materials*. Prentice Hall, 1973.

[46] T. B. Massalski, editor. *Binary Alloy Phase Diagrams*, volume 1. ASM International, 1986.

[47] D.R.F. West. *Ternary Equilibrium Diagrams*. Chapman and Hall, 1982. ISBN 9780412228209. URL `http://books.google.co.uk/books?id=U7t2QgAACAAJ`.

[48] Prof. Stephen A. Nelson. Ternary phase diagrams. Online, October 2014. URL `www.tulane.edu/~sanelson/eens212/ternaryphdiag.htm`.

[49] Asahiko Sugaki and Hiromi Shima. Phase relations of the Cu_2S–Bi_2S_3 system. *Technology Reports of the Yamaguchi University*, 1:45–70, 1972. URL `http://repository.oai.yamaguchi-u.ac.jp/yunoca/AA0086073X/KJ00004350902.pdf`.

[50] K. D. Leaver and B. N. Chapman. *Thin Films*. Wykeham Publications, 1971.

[51] Charles N. Singman. Atomic volume and allotropy of the elements. *Journal of Chemical Education*, 61(2):137–142, 1984. doi:10.1021/ed061p137.

[52] Leszek Rycerz. Practical remarks concerning phase diagrams determination on the basis of differential scanning calorimetry measurements. *Journal of Thermal Analysis and Calorimetry*, 113(1):231–238, 2013. doi:10.1007/s10973-013-3097-0.

[53] Milton Ohring. *Materials Science of Thin Films*. Academic Press, second edition, 2002.

[54] Mindat.org. Main page. Online, October 2015. URL `www.mindat.org`.

[55] R. Blachnik and A. Müller. The formation of Cu_2S from the elements: I. copper used in form of powders. *Thermochimica Acta*, 361(1-2):31–52, 2000. doi:10.1016/S0040-6031(00)00545-1.

[56] Masakuni Matsuoka and Rika Ozawa. Determination of solid-liquid phase equilibria of binary organic systems by differential scanning calorimetry. *Journal of Crystal Growth*, 96(3):596–604, 1989. doi:10.1016/0022-0248(89)90057-2. URL `http://www.sciencedirect.com/science/article/pii/0022024889900572`.

[57] Magicplot Systems. Main page. Online, November 2014. URL `www.magicplot.com`.

[58] M. Hädrich, N. Lorenz, H. Metzner, U. Reislöhner, S. Mack, M. Gossla, and W. Witthuhn. CdTe−CdS solar cells — production in a new baseline and investigation of material properties. In *EMRS 2006 Conference Sympodium O on Thin Film Chalcogenide Photovoltaic Materials*, volume 515, pages 5804 – 5807, 2007. doi:10.1016/j.tsf.2006.12.036.

[59] M. Schulz, O. Madalung, and U. Rössler. Bismuth sulfide (Bi_2S_3) heat capacity, density, melting point. SpringerMaterials — The Landolt-Börnstein Database. `http://www.springermaterials.com`.

[60] J.-C. Lin, R.C. Sharma, and Y.A. Chang. The Bi-S (Bismuth-Sulfur) system. *Journal of Phase Equilibria*, 17(2):132–139, 1996. doi:10.1007/BF02665790.

[61] Pierre Villars, Alan Prince, and Hiroaki Okamoto, editors. *Handbook of ternary alloy phase diagrams*, volume 5. ASM International, 1995.

[62] B. Gather and R. Blachnik. Temperature-composition diagrams in the Cu_2(VIb)-(Vb) sections of the ternary Cu-(Vb)-(VIb) systems (Vb = As, Sb, Bi; VIb = S, Se, Te). *Journal of the Less Common Metals*, 48(2):205–212, 1976. doi:10.1016/0022-5088(76)90003-5.

[63] Von Rudolf Vogel, Ingrid Riethmüller, and Christa Hochhaus. Über das System Wismutsulfid-Kupfersulfid und über das Dreitoffsystem $Bi-Bi_2S_3-Cu_2S-Cu$. *Zeitschrift für Metallkunde*, 47(10):694–699, 1956.

[64] M.V. Yakushev, P. Maiello, T. Raadik, M.J. Shaw, P.R. Edwards, J. Krustok, A.V. Mudryi, I. Forbes, and R.W. Martin. Electronic and structural characterisation of Cu_3BiS_3 thin films for the absorber layer of sustainable photovoltaics. *Thin Solid Films*, 562:195 – 199, 2014. doi:10.1016/j.tsf.2014.04.057.

Appendix A

LabVIEW program

A program was written in LabVIEW to control the monochromator and read the multimeter and lock-in amplifier. A visual representation of the program can be seen in Figure A.1. It takes the start, end and interval wavelengths in nanometres, wait time and time constant in seconds as inputs. It moves the monochromator from the start wavelength to the end wavelength in steps using the specified interval. At each step a while loop is run which records the current through the diode from the multimeter and the current through the sample from the lock-in amplifier. It does this twice and takes an average for each quantity. The first readings are taken after the wait time which is set to 3 to 5 times the time constant selected on the lock in amplifier. The second readings are taken after a further wait equal to the time constant. These averages are I_d and I_s respectively, as mentioned in Section 3.3.5. The responsiveness of the diode is interpolated from the tabulated values supplied with the equipment and the power is calculated using Equation (3.6). To get the conductance per unit power I_s is divided by both the power and the voltage of the battery as in Equation (A.1).

$$G_s/P = \frac{I_s}{V_s}/P = \frac{I_s}{V_s P} \tag{A.1}$$

The program outputs four sets of data: Lock-in current versus wavelength; incident power versus wavelength; conductance per unit power versus wavelength; and conductance per unit power versus photon energy. These are automatically plotted as the program is run but can be manually exported to a spreadsheet.

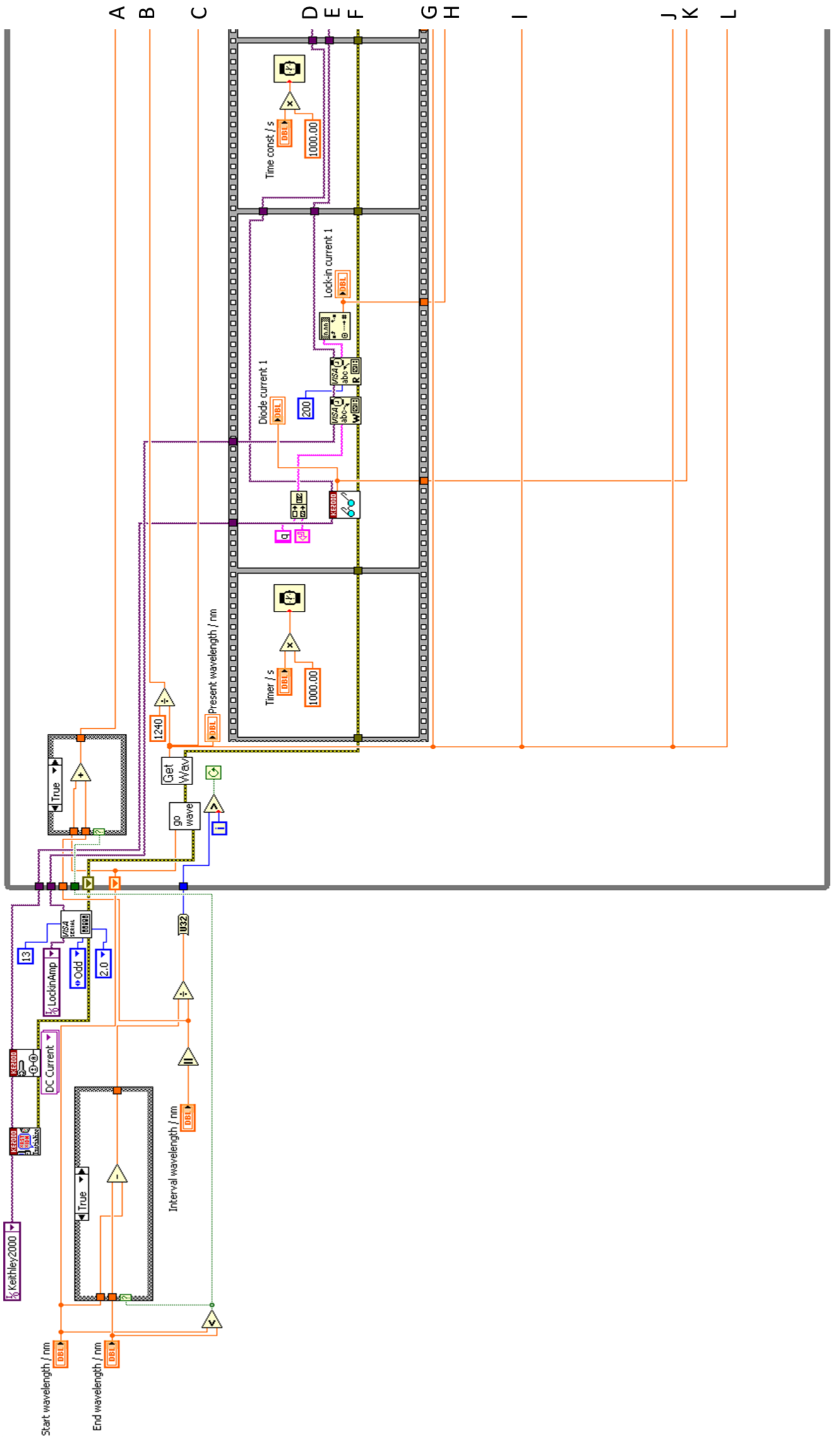

Figure A.1: LabView photoconductivity program block diagram

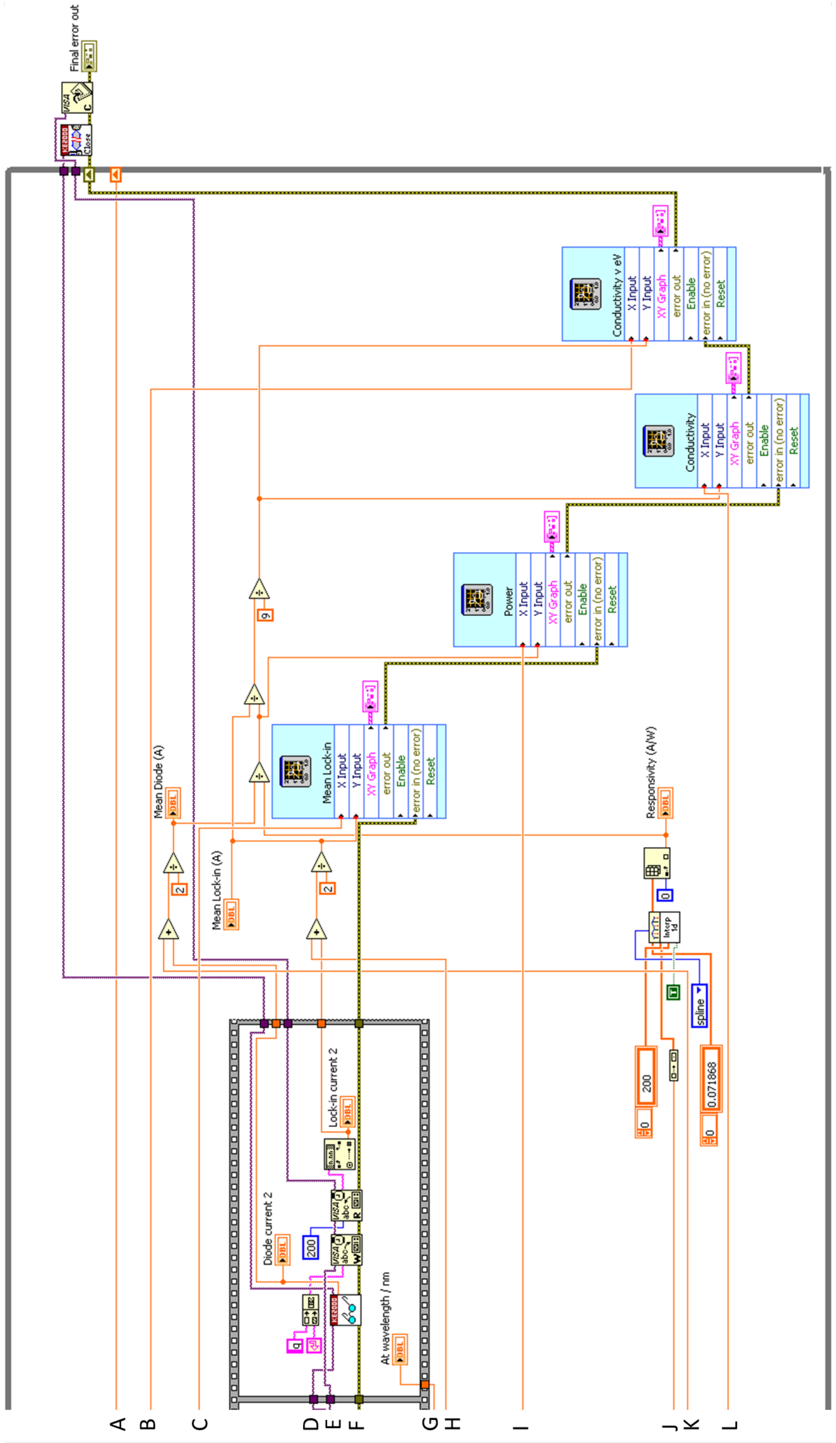

Figure A.1: LabView photoconductivity program block diagram (cont.)